Design of patch filters for millimeter-wave applications in BiCMOS 55-nm technology

Mohammed Wehbi

THÈSE

Pour obtenir le grade de

DOCTEUR DE L'UNIVERSITÉ GRENOBLE ALPES

École doctorale : EEATS - Electronique, Electrotechnique, Automatique, Traitement du Signal (EEATS)
Spécialité : Nano électronique et Nano technologies
Unité de recherche : Techniques de l'Informatique et de la Microélectronique pour l'Architecture des systèmes intégrés

Conception de filtres patch pour applications en bande millimétrique en technologie BiCMOS 55 nm

Design of patch filters for millimeter-wave applications in BiCMOS 55-nm technology

Présentée par :

Mohammed WEHBI

Direction de thèse :

Philippe FERRARI Professeur des universités, Université Grenoble Alpes	Directeur de thèse

Rapporteurs :

Cédric QUENDO
PROFESSEUR DES UNIVERSITES, UNIVERSITE DE BREST-BRETAGNE OCCIDENTALE
Serge VERDEYME
PROFESSEUR DES UNIVERSITES, UNIVERSITE DE LIMOGES

Thèse soutenue publiquement le **6 mars 2023**, devant le jury composé de :

Philippe FERRARI PROFESSEUR DES UNIVERSITES, UNIVERSITE GRENOBLE ALPES	Directeur de thèse
Cédric QUENDO PROFESSEUR DES UNIVERSITES, UNIVERSITE DE BREST-BRETAGNE OCCIDENTALE	Rapporteur
Serge VERDEYME PROFESSEUR DES UNIVERSITES, UNIVERSITE DE LIMOGES	Rapporteur
Anne-Laure FRANC MAITRE DE CONFERENCES, TOULOUSE INP	Examinatrice
Florence PODEVIN PROFESSEUR DES UNIVERSITES, GRENOBLE INP	Présidente
Cédric DURAND DOCTEUR EN SCIENCES, ST MICROELECTRONICS	Examinateur

Invités :

Ariana Lacorte Caniato SERRANO
PROFESSEUR DES UNIVERSITES, Universidade de São Paulo USP

ACKNOWLEDGMENT

This work has successfully arisen within the blessings, prosperity and love of our holly GOD, especially with COVID moments where “HOPE-” was “-LESS”. During these days tightness with the family was from abroad, thanks to them for standing by me.

A special and dedicated thanks to my director Philippe FERRARI who wasn’t only a professor but indeed a godfather. Working under his supervision with TIMA Laboratory family was great and an added value. So, thanks to all the staff and students who were keen to provide the support and thoughts to build up this achievement.

I would like to thank my village in Lebanon, Alkharayeb, who supported me in the very beginning of the thesis. While, after the unfortunate economic crisis that happened in Lebanon, FRANCE through different local funding contracts, within the University Of Grenoble Alpes labs, was the rescue. So, big thanks to the country that we Lebanese consider as our affectionate “Mother”.

RESUME

Cette thèse démontre la réalisation des premiers filtres de type patch en bande millimétrique au-delà de 50 GHz, en technologie intégrée BiCMOS 55 nm fournie par la société STMicroelectronics. Deux versions de Back-End-Of-Line ont été utilisées, offrant respectivement huit niveaux de métaux (8ML) et neuf niveaux de métaux (9ML). Les objectifs étaient de réaliser des filtres alliant performances et forte compacité afin de répondre aux besoins futurs de la 6ème génération de systèmes de télécommunication (6G). Plus précisément, un des objectifs était de réaliser des filtres et diplexer présentant des bandes passantes inférieures à 10% au-delà de 120 GHz. Grâce à l'excellente collaboration entre le laboratoire TIMA et la société STMicroelectronics, ainsi que l'aide précieuse de l'IEMN à Lille pour les phases de caractérisation RF, les objectifs ont été atteints, avec de nombreux filtres et diplexer réalisés entre 50 GHz et près de 300 GHz.

Les technologies utilisées ont dans un premier temps été évaluées en termes de performances en extrayant le facteur de qualité non chargé, Q_u, de patchs élémentaires, ceci pour de nombreuses combinaisons de métaux offerts par le Back-End-Of-Line. Cela a permis d'effectuer un choix éclairé des métaux à utiliser pour les filtres.

Afin de réduire la surface des patchs, de nombreuses techniques issues des filtres RF réalisas en technologie PCB ont été étudiées en technologie BiCMOS, afin de réduire la surface des patchs. Ces techniques concernent l'utilisation de vias, de fentes, et de charges capacitives afin de pouvoir généraliser une approche de conception basée sur des résonateurs multi-modes. Ces techniques nous ont conduit à développer de nouvelles méthodes de synthèses asynchrones afin de concevoir les filtres multi-modes souhaités. Des filtres multi-résonateurs couplés ont également été réalisés, afin d'améliorer la sélectivité, en utilisant une méthode de synthèse traditionnelle.

L'implémentation et le layout des filtres est une phase clé très importante lorsque qu'il s'agit de gérer des circuits passifs en technologies avancées. En se basant sur les règles de dessin fournies par le fondeur (DRM pour « Design Rule Manuel »), les caractéristiques des métaux (layers et vias) ainsi que des diélectriques ont été extraites en amont de la synthèse. Une fois la synthèse réalisée, il s'est agit de considérer les règles de densité et de gérer l'ajout de dummies de manière judicieuse afin de ne pas impacter de manière trop

forte les performances des filtres, cette étape nécessitant le recours intensif à la simulation électromagnétique 3D.

Au final, les filtres réalisés et mesurés montrent pour certains des performances à l'état de l'art. En particulier, nous avons démontré qu'il était possible de réaliser des diplexer avec des filtres bande étroite (< 10%) présentant des pertes inférieures à 3 dB dans la bande.

ABSTRACT

This dissertation introduces the first patch filter design at mm-waves band above 50 GHz, using the BiCMOS 55-nm integrated circuit technology that is provided by STmicroelectronics. The two versions of BiCMOS55 (8 Metal Layers (8ML) and 9ML EVO), are exploited in order to gain space in comparison between different filter designs performance. The aim is to design the first narrow-band dual-mode bandpass patch filter targeting frequencies above 120 GHz with 10% of fractional bandwidth. Thanks to the framework collaboration between TIMA Laboratory and STMicroelectronics, that allowed the availability of participating in different realization tapeout runs in order to design and implement several original 2nd order and dual-band patch-like filters targeting frequencies at 50 GHz, 60 GHz, 90 GHz, 200 GHz and 270 GHz.

Since, the potentiality of the technology is not yet known for patch resonators, the unloaded quality factor Q_u is extracted and compared for all different metal/oxide layer substrates from the BACK-END-OF-LINE (BEOL). Then, based on the extracted information, the suitable layers are chosen. Moreover, it is very important to have compact patch filter, a deep analysis of using grounded *vias* with patch resonators has encountered to understand its influence on size reduction and fundamental resonance modes. Grounded *vias* are used with antennas for modes suppression, but it is barely used with filters. This has led us to newly developing its synthesis methodology in order to design the asynchronous narrowband dual-mode bandpass filter. Moreover, filters with cascaded coupling scheme are conducted while using the traditional synthesis approach.

Implementation or layout scheme of the designed filters is pivotal in this work flow. Based on the design rule manual (DRM) provided by the manufacturer, the characteristics of the oxide layers along with the conductivity of the metal layers and other elements, such as *vias*, are extracted. Due to the strict and picky design rules, especially for the Min/Max metal dimensions and surface metal densities, post-layout simulation is required to compensate their influence on the intended filter.

Last but not least, the presented developed filters showed a great performance in comparison to the state-of-the-art. Also, as a demonstration, we have shown that it is possible to realize integrated mm-wave diplexers at 90 GHz with narrow band filters (< 10%) presenting losses around 3 dB within the passband.

CONTENTS

LIST OF FIGURES

LIST OF TABLES

LIST OF ABBREVIATIONS

6G - sixth generation mobile radio

AI - Artificial Intelligence

AR/VR - Augmented /Virtual Reality

5G - fifth generation mobile radio

IoT - internet of things

eMBB - enhanced mobile broadband

FWA - fixed wireless access

ITU-R - International Telecommunication Union Radio Sector

OSI - Open Systems Interconnection

MIMO - Multiple Input, Multiple Output

mm-wave – Millimeter-Wave

MMIC - Microwave Monolithic Integrated Circuits

CMOS – Complementary metal–oxide–semiconductor

BiCMOS – Bipolar Complementary metal–oxide–semiconductor

PAE - Power Added Efficiency

SiGe - Silicon–Germanium

BGA - Ball Grid Array

PCB - Printed Circuit Board

LTCC - Low Temperature Co-fired Ceramics

SIW - Substrate Integrated Waveguide

GaAs - Gallium Arsenide

InP - Indium Phosphide

INTRODUCTION

Motivation

In 2020, the beginning of my thesis work, our mindset has been tuned to welcome a new era of telecommunication, which obeys capabilities to transfer us into the "Meta-verse". It is the upcoming promising virtual universe integration that unifies our current experiences across the physical, digital and human world as the diagram in Figure 0.1 shows [1]. Hopefully, it offers more efficient, productive and energy less life. It is not a science fiction, it is what researchers and scientists are promising us after a decade when launching the sixth generation mobile radio (6G).

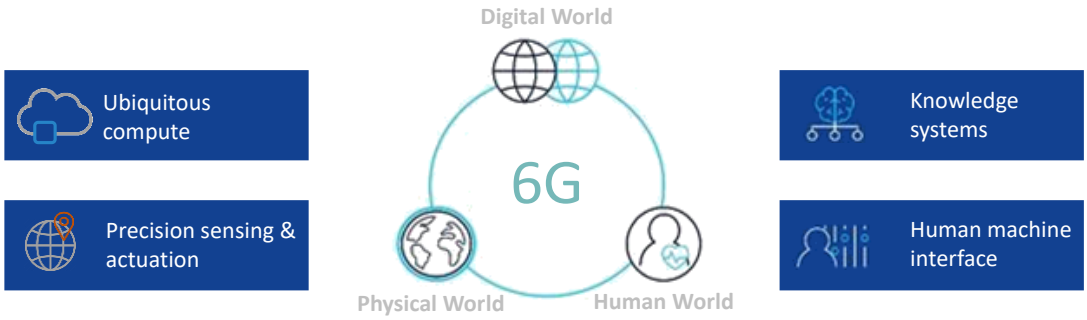

Figure 0.1: 6G will unify the experience across physical, digital and human worlds [1].

It will require development of advanced mobile communication technologies such as cognitive and highly secure data networks with massive sensors. The expected applications will be more relied on Artificial Intelligence (AI) and machine learning such as Augmented /Virtual Reality (AR/VR) with holographic videos, sensory interfaces that feel like real life…etc. Its technological standards are not clear yet, but it will rely on the current fifth generation mobile radio (5G) architecture with new expected frequency allocations at: low bands 460-694 MHz, mid-bands 7-20 GHz for urban outdoor cells enabling higher capacity and sub-THz band for short ranges with peak data rate promising to be up to 1 Terra Byte per second (TB/s).

In the meantime, the deployment of 5G radio network or what marketers like to alias, the internet of things (IoT), has just launched. Ericson in its mobility report released in June 2022, mentioned that till now there are 1 billion 5G subscribers and expected to reach

4.4 billion in 2027 [2]. This has intensively pushed industry consortium to take the investment today to provide the most common services of 5G: enhanced mobile broadband (eMBB), fixed wireless access (FWA), gaming and AR/VR services, and the most important smart cities.

Based on the International Telecommunication Union - Radio communication sector (ITU-R) standards, 5G involves a new network structure implicating the use of different techniques and technologies in Open Systems Interconnection (OSI) model media layers (physical, data link, and network layers), such as massive Multiple Input, Multiple Output (MIMO), different frequency bands and small cells. In Europe, the frequency allocations are as follows: 700 MHz for wide range coverage, 3.6 GHz and 26 GHz for urban capacity, and 60 GHz (57-66) for security and medical monitoring services that require very high data rates and bandwidths [3].

Based on the presented motivation and in order to meet the expectations of the demanders to have 5G, and future 6G applications with high data rates and low power consumption, a revolution in the millimeter wave (mm-wave) circuit design is on the move. For that purpose, advancements in Microwave Monolithic Integrated Circuits (MMIC) technologies like CMOS/BiCMOS have gained the attention of researchers in the last two decades for mm-wave circuit design. Nowadays, its high-performance transistor features (f_T/f_{max} around 500/600 GHz) makes it very suitable for 5G and 6G applications in the sub-THz band like automotive radars, imaging systems for medicine or security defense [4]. To take advantage of these technologies, sophisticated transceivers must be developed. However, today it comes up against several obstacles, mainly, (i) the connection of the antenna system to the (Bi)CMOS chips often with the need for a beam orientation capability, (ii) the energy efficiency of the chips, which is very limited with efficiencies Power Added Efficiency (PAE) of the order of 10% for power amplifiers in Silicon–Germanium (SiGe) technology in D-band, and last but not least (iii) the non-availability of diplexers.

For that purpose, diplexers are essential if the optimization of bandwidth is required, which is the case. But their realization relies on filters. Filters are a fundamental building block for any RF front-end of a transceiver. Nevertheless, it is problematic to combine the efficient active blocks developed on BiCMOS with filters and other passive blocks using

different technologies due to the interconnection, for instance Ball Grid Array (BGA) and wafer bonding packaging parasitics become significant beyond 50-100 GHz. Apart from mobile terminals at RF bands, where the use of acoustic waves filters is the must, filters are mainly produced in Printed Circuit Board (PCB) or Low Temperature Co-fired Ceramics (LTCC) technologies in RF, up to a few tens of GHz, along with an undeniable appeal of Substrate Integrated Waveguide (SIW) technologies in particular as of today. However, it is very tricky to use them, because the precision capabilities of these technologies does not make it possible to produce filters beyond 100 GHz, implying insufficient control of the resonance frequencies. Therefore, MMICs produced by BiCMOS technologies are a worthy choice for designing mm-wave integrated passive devices, not only because of its high-tech, but also with a moderate fabrication cost compared to Gallium Arsenide (GaAs) or Indium Phosphide (InP) counterparts.

Challenges Overview

Designing a good performed integrated passive filter while compensating the occurrence of high losses or parasitic effects, is really challenging. Filters based on lumped components topologies as inductors and capacitors are unsuitable at mm-waves, since the quality factor (QF) of capacitors drastically decreases with frequency. Hence, distributed circuits based on microstrip lines technology is preferable, as the QF of a Transmission Line (TLine) increases with frequency since the propagation constant, that is proportional to the frequency, increases faster than the attenuation constant. This is mainly driven by the skin depth and its frequency square root dependence. However, TLines based resonators are still considered lossy, since the width of the strips is limited by the reduced height of the Back-End-Of-Line (BEOL). Many promising studies based on slow-wave TLines, and in particular slow-wave coplanar waveguides (S-CPW) are considered a good resonator choice to have i) immunity against losses with better QF and ii) reduced dimensions [5]. Nevertheless, the compactness induces a significant cost in terms of design, because mastering the concepts of S-CPW is not easy. Also, it seems complicated to simply transfer this approach to designers of mm-wave circuits, and last but not least, the S-CPW quality factor becomes lower than the one obtained by microstrip lines above about 150 GHz.

More generally, the literature has encountered few works for passive filters that operate at mm-wave band and implemented on CMOS/BiCMOS technologies [6-52]. Only a single work exists for bandpass filter operating beyond 100 GHz [52]. It uses the coupled S-CPW topology to have flexible responses with reduction of losses and existence of transmission zeros (TZs). However, its measured unloaded quality factor for single resonator is still limited. Moreover, the lowest achieved fractional bandwidth for acceptable losses was not less than 20 %, which is a common challenge for filters at mm-wave. Conversely, patch filters, which are sophistically designed at RF and microwave bands, are an earnest choice to support multi-modes functionality [53-76], and hence in fine lead to compact size, even if the patch approach is a priori not very compact. Its electrical properties allow to have infinite number of modes within a single resonator at different frequencies. Moreover, its design simplicity makes it possible to control its degenerated modes by inserting well known perturbations. A high-performance design for bandpass filter with multi-layering technique was developed in [61;62;65;68;70]. A wide range of frequency response flexibility was achieved with a multiple of controlled TZs, thanks to the use of cross slots. Away from its good performance with higher power handling compared with microstrip topologies, designing compact patch filters is still an issue. Improving compactness would be possible by using shorting posts (vias). Theoretically, as reported in [72], a new generated LC-mode appears at lower frequency as compared to the fundamental mode of the patch resonator. This has allowed to develop a wide band compact triple mode bandpass filter [73;75;76]. However, developing compact narrowband dual-mode bandpass filter based on patch resonators is still a challenge.

Patch filter concept has never been explored at mm-waves and CMOS/BiCMOS technology, to the author's best knowledge. This makes it complicated to understand its behavior with multi-layering structure of IC. Thus, it seemed interesting to explore the "patch approach" to realize mm-wave filters above 100 GHz in CMOS/BiCMOS technologies, and compare it to more conventional Tline-based approaches.

Objectives

This dissertation introduces the first patch filter design at mm-waves band above 50 GHz, using the BiCMOS 55-nm integrated circuit technology that is provided by

STMicroelectronics. The two versions of BiCMOS55 (8 Metal Layers (8ML) and (9ML EVO), are exploited in order to gain margin in comparison between different filter designs performance. The aim is to design the first narrow-band dual-mode bandpass patch filter targeting frequencies above 120 GHz with 10% of fractional bandwidth. The framework collaboration between TIMA Laboratory and STMicroelectronics allowed the availability of participating in different realization tape-out runs in order to design and implement several original 2nd order and dual-band patch-like filters targeting frequencies at 50 GHz, 60 GHz, 90 GHz, 200 GHz and 270 GHz.

Since, the potentiality of the technology is not yet known for patch resonators, the unloaded quality factor Q_u is extracted and compared for all different metal/oxide layer substrates from the BEOL. Then, based on the extracted information, the suitable layers are chosen.

It is very pivotal to have compact patch filters at mm-wave bands. Then, a deep analysis of using grounded vias with patch resonators has encountered to understand its influence on size reduction and fundamental resonance modes. Grounded vias are used with antennas for modes suppression, but it is barely used with filters. This has led us to newly developing its synthesis methodology in order to design the asynchronous narrowband dual-mode bandpass filter. Moreover, filters with cascaded coupling scheme are conducted while using the traditional synthesis approach.

Implementation or layout scheme of the designed filters is pivotal in this work flow. Based on the design rule manual (DRM) provided by the manufacturer, the characteristics of the oxide layers along with the conductivity of the metal layers and other elements, such as vias models, are extracted. Due to the strict and picky design rules, especially for the Min/Max metal dimensions and surface metal densities, post-layout simulation is required to compensate their influence on the intended filter.

Organization

CHAPTER I is divided into two parts. Firstly, it shows the literature review of most designed dual-mode patch filters at RF and Microwave bands in order to classify and select the techniques used to provide the duality concept. Also, a literature review of the recent designed integrated filters at mm-wave highlighting the main challenges. In the second

part, general patch resonator analysis is conducted while comparing the different extracted Q_u in order to show the effect of BEOL height on the performance of the filter.

In CHAPTER II, the patch resonator theory, with and without vias, is recalled to examine the multi-resonance modes electrical performance. This helps in distinguishing the impact of using different perturbation elements techniques. Then, the full synthesis design methodology is thoroughly represented to design asynchronous tuned filters. The extraction of coupling matrix and its coupling scheme are also piloted.

CHAPTER III presents a full and detailed design study of several patch filters. It focuses on applying the design methodology presented in chapter III to synthesize the filter especially when using grounded vias as a new introduced mode. The extraction of external quality factor Q_e is discussed to show the influence of the feeding position on the overall performance of the filter. Filters with dual-mode and dual-band performance are developed along with patch-like miniaturized cascaded 2nd order filters that are designed and simulated.

In CHAPTER IV, the layout scheme and measurements of all developed filters are presented. It draws up the layout methodology that should be followed by passive integrated circuits designer in order to successfully implement and compensate the effect of unfavorable design rules. Then, 2-ports on-wafer measurements process and results are shown.

CHAPTER V opens the interval for discussion on what can be done in future. Also, it presents an interesting design for diplexer with RX/TX filter operating at 90 GHz. This will be considered the first integrated diplexer at mm-wave band.

Lastly, the whole work is concluded and summarized.

CHAPTER I: PATCH FILTER LITERATURE REVIEW

Through the last two decades, researchers have developed a huge and very sophisticated work regarding bandpass RF and microwave filters. Due to the demand of narrow band applications with size reduction, RF filters must satisfy different conditions:

1- Narrow Band (%FBW < 20 %)
2- Low power consumption
3- Compact size
4- Good out of band rejection
5- Sharp selectivity

Recently, planar technology was mostly used due to its low cost, open structure that makes it easy to be integrated with lumped components (L,C and varactor diodes), and weight. These characteristics were exploited to develop RF and microwave filters using different topologies such as: coupled-line, rings, stubs, patches and others. Higher order filters with cascaded form can be easily implemented on planar technology in order to reach better performance. However, when multiple resonators are used the overall size of the filter is drastically increased. So, dual- and multi-mode filters with minimum number of cascaded resonators have become pivotal.

In this chapter, the literature review of designed patches at frequencies below 10 GHz is conducted to get inspired with patch geometry and used perturbation techniques. Then, the state-of-art for filters that are developed on integrated circuits beyond 30 GHz are presented to check the main filter design challenges and the margin of improvements with patch resonators. Lastly, the first general patch resonator analysis on BiCMOS 55nm technology is interpreted.

1.1. Patch Filters' Literature Review

In the 1950's, Lin [53] was the first to introduce the dual-mode concept. This new concept allows the increase of filter's order without adding more resonators. The idea is to create coupling between the so-called degenerated modes to split them and form the dual-mode model. Initially, these modes operate at the same resonant frequency that is

determined by the overall structure of the design, but with different Electro-Magnetic (EM) field distribution. Two decades later in 1971, Wolf [54] used this concept on planar technology using circular dual mode ring resonator (Figure 1.1). In 1991, after the planar filters become more popular, Curtis and Fiedziuszko [55], took the initiative to present a miniaturized dual mode microstrip filter using full patch resonator as shown in Figure 1.2. They split the degenerated modes using an edge cut (inductive loading).

Hong and Lancaster in [56] and [57] developed the first sophisticated microwave dual-mode ring filters in 1995. They are based on the study presented previously by Wolf. Two studies were conducted at that time: one using a rectangular loop resonator (Figure 1.3(a)) and the other using the meandered loop resonator (Figure 1.3(b)). Both designs achieve the dual-mode characteristics, by splitting the degenerated modes through adding an edge triangular or square perturbation element (capacitive loading). Bandpass filters with two poles and single resonator were presented. Hong and Lancaster mentioned that the behavior of the degenerated modes in the loop resonator are approximately the same as for the full rectangular patch resonator. Later in 1999, Zhu *et al.* introduced a new technique to split the modes of a rectangular patch resonator [58]. The idea is based on adding diagonal cross etch slots inside the patch. Using asymmetric diagonal etch structure with Δl difference as shown in Figure 1.4, the degenerated modes can be split easily to form the dual-mode filter.

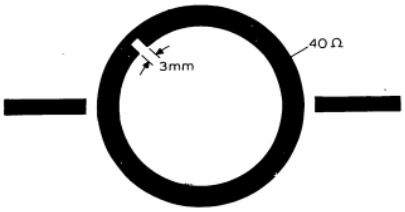

Figure 1.1: Microstrip ring resonator disturbed by a notch of width w and depth t of the structure proposed in [54].

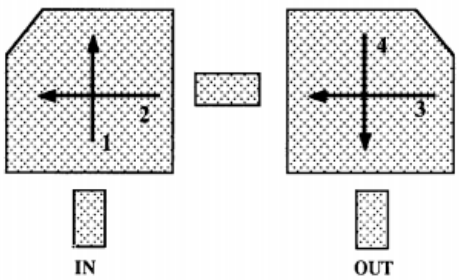

Figure 1.2: Sketch of a dual mode, four pole, microstrip filter proposed in [55].

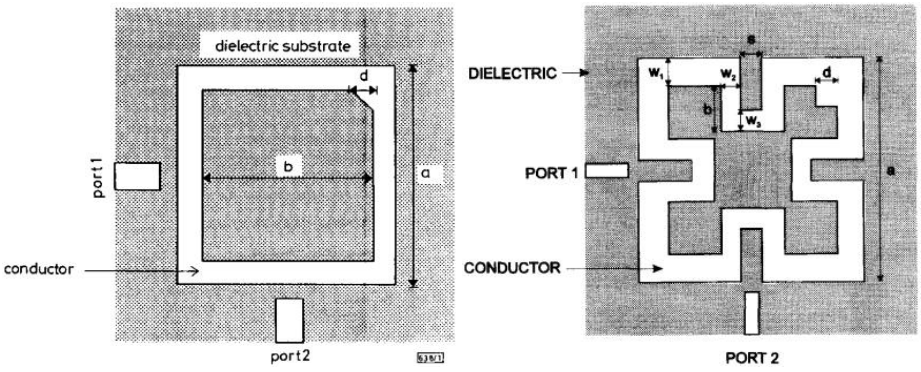

(a) (b)

Figure 1.3: (a) Dual-mode microstrip square loop resonator proposed in [56], (b) Dual-mode microstrip meander loop resonator proposed in [57].

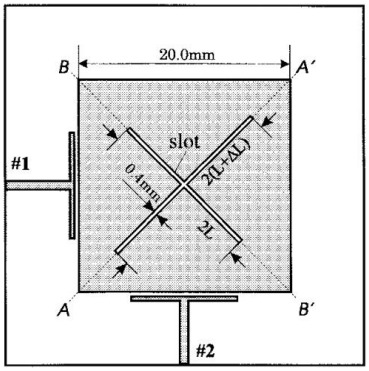

Figure 1.4: Geometrical view of a planar dual-mode bandpass filter etched with a pair of asymmetrical crossed slots with built-in control element of mode coupling or perturbation element ΔL proposed in [58].

In their study, the authors show that the patch unloaded quality factor Q_u decreases with frequency, although its radiation losses are reduced due to the usage of slots.

After this work, a lot of filters were developed using slot perturbation technique to build dual-mode filters [58-64], dual-band filters [65-67], Balun filters [68-69] and balanced filters [70-71]. From design methodology perspective, dual-mode filters are synthesized using the asynchronous tuning method that was presented in [77]. This method was thoroughly discussed and firstly introduced in [60] in order to build a tunable triangular patch filter. As shown in Figure 1.5, two etched slots were used to independently control each degenerated mode, where different biased varactors were inserted between the slots to provide tunability.

Despite their great performances, most of these filters still suffer from large size, which

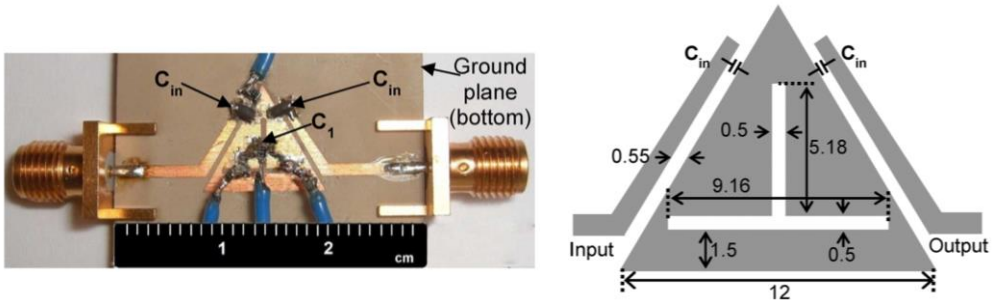

(a) (b)

Figure 1.5: (a) Fabricated tunable filter, (b) Layout [60].

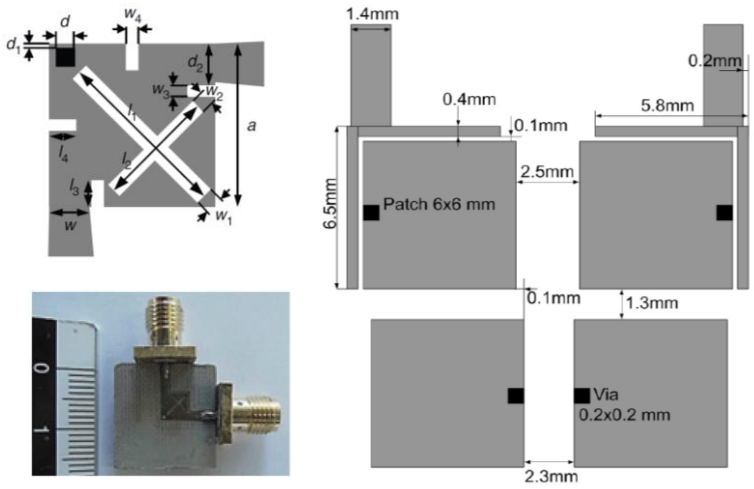

(a) (b)

Figure 1.6: (a) Triple mode wideband filter [73], (b) Cross-coupled 4th order filter [74].

make filters using TLine topology more favorable. In order to overcome this issue, grounded vias were used. The corresponding theory was originally developed in [72]. It is modeled as an LC circuit, and its resonance frequency is named zero-mode since it appears below the fundamental frequency of the patch resonator. This new mode was used with square patch resonator in [73] to build a compact wide band filter. In this work, authors have combined both crossed slots with single via (Figure 1.6(a)). The two slots control the degenerated modes and the dimension of via controls its self-resonance frequency. Another approach for using vias was to build a 4th order filter [74], where four grounded square resonators were implemented as shown in (Figure 1.6(b)). This time only via mode is used to build the filter using the cross-coupled synthesis methodology presented in [77]. Adjacent resonators were coupled by magnetic-coupling when *vias* are facing each other

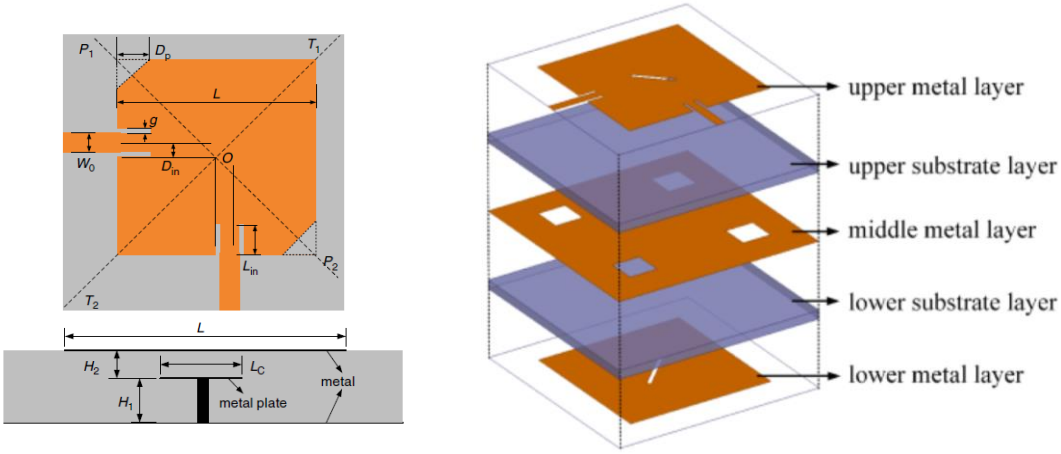

(a) (b)

Figure 1.7: (a) Triple-mode filter [61], (b) 4th order 3D filter [62].

and by electric-coupling where *vias* are aside. This allowed flexibility in tuning the filter's performance.

Another approach for size reduction is to use technologies that support multilayer structures. Authors in [61] and [62] used the multi-layered PCB technology in order to increase the order of the filter without increasing its size. In [61], a triple-mode bandpass filter using single square patch resonator was realized. As shown in Figure 1.7(a), the approach was based on edged-cut perturbation to split the degenerated modes and an embedded mushroom load to perturb the first higher order mode. Another advanced approach is presented in [62] using multi-layered PCB with same height and relative dielectric constant ε_r to build cascaded dual-mode patch filter in 3D sandwich, as shown in Figure 1.7(b). Both resonators provide dual-mode response using single diagonal etched slot. They are coupled to each other through aperture at ground level, which is in the middle. This work provides a 4th order bandpass filter with generalized responses.

Based on the presented summary, Table 1.1 shows different perturbation techniques that were used with patch resonators, along with their functionality. Perturbations are classified into either inductive perturbation where surface current J flow is affected, or capacitive perturbation where electric field E is affected. More than one technique can be used at a time with single resonator to build more sophisticated filter with flexible response. This will be discussed further in the coming chapters.

Table 1.1: Patch resonator's perturbation techniques.

Perturbation	Types	Functionality
Edge Cut	Inductive	Split fundamental modes
Edge Extension	Capacitive	Split fundamental modes
Shorted VIA	Capacitive	Split fundamental modes & adds new LC mode
Slots	Inductive	Split fundamental modes
Mushroom	Capacitive	Loads resonance mode

1.2. Integrated Filters' Literature Review

Filter design at mm-wave bands requires high flexibility in precision, which is currently offered by most of integrated technologies as BiCMOS/CMOS, GaAs, and InPs. Passive filters that are implemented on GaAs or Integrated Passive Devices (IPD) technologies, could achieve a very good performance especially when Q_u overcomes 100 at 30 GHz [78-85]. This is due to their significant thickness height for BEOL. Nevertheless, it is unlikely to be combined with active circuits like PAs or LNAs that require transistors to have operation capabilities to be higher than 60 GHz, and high-density digital circuits, which is not offered by them. On the other side, technologies as PCB and LTCC that support multi-layering structure are very usefull for frequencies below 60 GHz due to their availability. However, with higher bands it is not favorable, since the interconnection parasitics become significant when connecting devices with different technologies. For these reasons and more, in this subsection a full review on the recorded designed filters using BiCMOS/CMOS technologies are only described [5-52].

Table 1.2 shows the results of mostly designed filters at mm-wave bands covering the frequencies from 12.5 GHz up to 120 GHz, which are implemented on either CMOS or BiCMOS technologies with different released versions. All filters are compared on the following criteria: operating frequency f_c (GHz), relative fractional bandwidth % *FBW*, insertion loss (dB), return loss (dB), technology, unloaded quality factor Q_u, Shape Factor *SF* at 30 dB and 20 dB, and size. Usually, measured Q_u is calculated using (1.1).

$$Q_u = 4.343 \frac{\sum_{i=1}^{n} g_i}{FBW_{3dB} \cdot IL} \tag{1.1}$$

Table 1.2: State-of-Art for mm-wave filters on BiCMOS/CMOS technologies.

Ref	f_c *(GHz)*	*FBW (%)*	*IL (dB)*	*RL (dB)*	*Technology*	Q_u	SF_{30dB}	SF_{20dB}	*Size (mm²)*
[5]-a	60	18	2.6	11	0.13 µBiCMOS	28	0.31	0.34	0.14
[5]-b	60	18	4.1	11	0.13 µm CMOS	23	0.32	0.37	0.29
[7]-a	12.5	24	1.5	16		26	0.13	0.14	0.03
[7]-b	14	29	2.5	15	0.13 µm SiGe	23	0.20	0.24	0.07
[7]-c	17	28	3.5	15		17	0.19	0.21	0.05
[8]	31	66	3.6	15	0.13 µm BiCMOS	7	0.46	0.55	0.05
[9]	21	19	5	15	0.13 µm CMOS	17	-	-	0.11
[11]-a	23	78	2.3	15	0.13 µm BiCMOS	9	-	0.55	0.15
[11]-b	27	70	2.6	13	0.35 µm CMOS	9	0.61	0.63	
[12]-a	23	17	3.8	20		19	0.13	0.17	0.02
[12]-b	31	11	3.2	15	0.13 µm SiGe	34	0.11	0.14	0.02
[12]-c	31	18	2.7	23		26	0.16	0.20	0.04
[15]-a	24	42	3.6	15	0.18 µm CMOS	11	0.26	0.34	0.61
[15]-b	60	27	2.8	10		22	0.38	0.47	
[16]	25	31	2.5	20	0.13 µm CMOS	21	0.21	0.31	0.28
[18]-a	27	18	2.5	13	0.13 µm BiCMOS	22	-	0.09	0.03
[18]-b	29	27	3.5	25		18	-	0.29	
[20]	30	23	1.66	18	0.13 µm BiCMOS	25	-	0.12	0.01
[21]	31	58	2.2	15	0.13 µm SiGe	13	-	0.37	0.02
[22]	31	23	2.4	15	0.13 µm SiGe	27	-	0.13	0.02
[23]-a	31	51	3.9	12	0.13 µm SiGe	8	-	0.44	0.08
[23]-b	35	50	3.1	20		11	-	0.46	
[24]	33	18	2.6	15	0.13 µm SiGe	21	0.12	0.15	0.04
[26]	34	67	1.5	11	45 nm CMOS	17	-	0.81	0.07
[27]	35	22	1.7	18	0.13 µm CMOS	26	-	0.15	0.04
[28]	35	54	4.5	12	0.18 µm CMOS	7	0.35	0.41	0.12
[29]	35	61	1.6	18.3	0.13 µm CMOS	17	-	-	0.03
[30]	40	20	1.7	19	0.13 µm BiCMOS	18	-	0.13	0.01
[34]	57	35	3.5	10.2	0.18 µm CMOS	14	-	0.51	0.07
[35]	60	21	2.5	25	0.18 µm CMOS	18	-	-	0.16
[36]	60	23	2.77	20	0.18 µm CMOS	26	0.18	0.47	0.59
[37]	60	13	3.13	11	0.18 µm CMOS	40	-	-	0.03
[38]	60	12	5	38	0.25 µm CMOS	22	-	0.18	0.32
[39]	60	17	4.7	9	90 nm CMOS	17	0.13	0.18	0.04
[40]	60	16	4	20	0.18 µm BiCMOS	27	-	0.17	0.18
[41]	64	19	4.9	10	0.18 µm CMOS	18	0.4	0.43	1.71
[42]	60	22	3.3	30	0.18 µm CMOS	23	-	-	0.05
[43]	60	14	5.9	10	0.13 µm CMOS	20	0.34	0.61	0.35
[44]	60	24	4.2	12	90 nm CMOS	16	-	-	0.12
[45]-a	60	10	9.3	10	0.18 µm CMOS	18	0.23	0.40	0.14
[45]-b	77	10	9.3	10		18	0.26	0.48	0.11
[46]	65	51	2.7	15	0.18 µm CMOS	12	0.02	0.38	0.17
[47]	62	34	3.1	10	0.18 µm CMOS	16	-	-	0.13
[48]	70	26	3.6	12	0.18 µm CMOS	18	0.44	0.55	0.44
[49]	77	18	3.5	10	0.18 µm CMOS	26	0.35	0.42	0.39
[50]	77	27	2.9	20	0.18 µm CMOS	21	0.34	0.42	0.02
[51]	77	23	3.9	20	0.13 µm CMOS	18	-	0.44	0.08
[52]-a	115	18	7.1	20		17	0.32	0.48	0.05
[52]-b	115	24	5.2	25	55 nm BiCMOS	17	0.36	0.51	0.07
[52]-c	125	28	4.9	10		16	0.41	0.58	0.07

where g_i are the elements of the low-pass prototype of Butterworth filter, FBW_{3dB} is the fractional 3-dB bandwidth, and *IL* is the insertion loss at mid-band frequency. It was proposed in [77] for filters with Butterworth responses. It should be noted that applying this method for calculating Q_u is not rigorous, because we must assume concerning the type of filtering function that is used (it is decided to consider a function of Butterworth type where function was not indicated by authors). Thus, it can be considered as a simple indicator making it possible to provide additional information to the measured insertion loss with the relative bandwidth. On the other hand, *SF* at 30 dB and 20 dB is calculated using:

$$SF = \Delta f_{3dB} / \Delta f_{xdB} \tag{1.2}$$

where Δf_{xdB} is calculated as the bandwidth corresponding to an attenuation of x dB (in our case it is 30 dB and 20 dB, respectively). It is a very important parameter, because some publications report filters that are not very selective, with an application range therefore relatively modest. In order to appropriately analyze the recorded results, insertion loss, Q_u and *SF* are plot against the *3-dB* FBW, while filter size are extracted against the operating frequency, as shown in Figure 1.8(a), Figure 1.8(c), Figure 1.8(d), Figure 1.8(e) and Figure 1.8(f), respectively. Also, the acquired chip size is plot in Figure 1.8(b). Filters are categorized according to their operating frequency (f_c < 55 GHz, 55 GHz < f_c < 65 GHz and f_c > 65 GHz) for fair and better comparison.

From Figure 1.8(a), the majority of the works exhibits FBW that ranges between 15% and 30 % with insertion loss variation between 1.5 dB and 7.1 dB. Particularly, the designed filters in [7-a;20;27;30] that operate at 12.5 GHz, 30 GHz, 35 GHz and 40 GHz, respectively, have the lowest insertion loss (around 1.5 dB) with FBW around 23 %. Also they achieved the lowest chip size below 0.04 mm^2. However, they have very poor selectivity, below 0.15, at both 20 dB and 30 dB with only 10 dB of suppression for the upper band rejection. Filters in [5;34;38;47] that operate around 60 GHz, are considered good works with a moderate performance that is tangible to the drawn trend line (logarithmic average). Several works like [8;11;21;23;28;29;46], have ultra-wideband responses with FBW above 60 %, while only [21;26;29] exhibit insertion loss below the trend line (around 1.5 dB) with acceptable selectivity and upper band rejection. Although,

filters which are below the trend line exhibit better performance from insertion loss and FBW perspective, other works like in [52], which operate above 100 GHz have best selectivity and rejection levels. Moreover, it is worth to mention that designing filters at very high frequencies has more design constraints and significant parasitic effects than those that operate below 60 GHz. In this case, the achieved performance in [52] is considered acceptable. In regards to the out-of-band rejection, most of the filters have good rejection levels of around 20 dB at lower and upper bands with only few works like [5;7;30] having very low rejection below 10 dB. Moreover, most of the filters that operate below 55 GHz, suffer from very low selectivity at 20 dB level. A very important factor to look at is the variation of Q_u in Figure 1.8(c). The majority of the filters have Q_u between 15 and

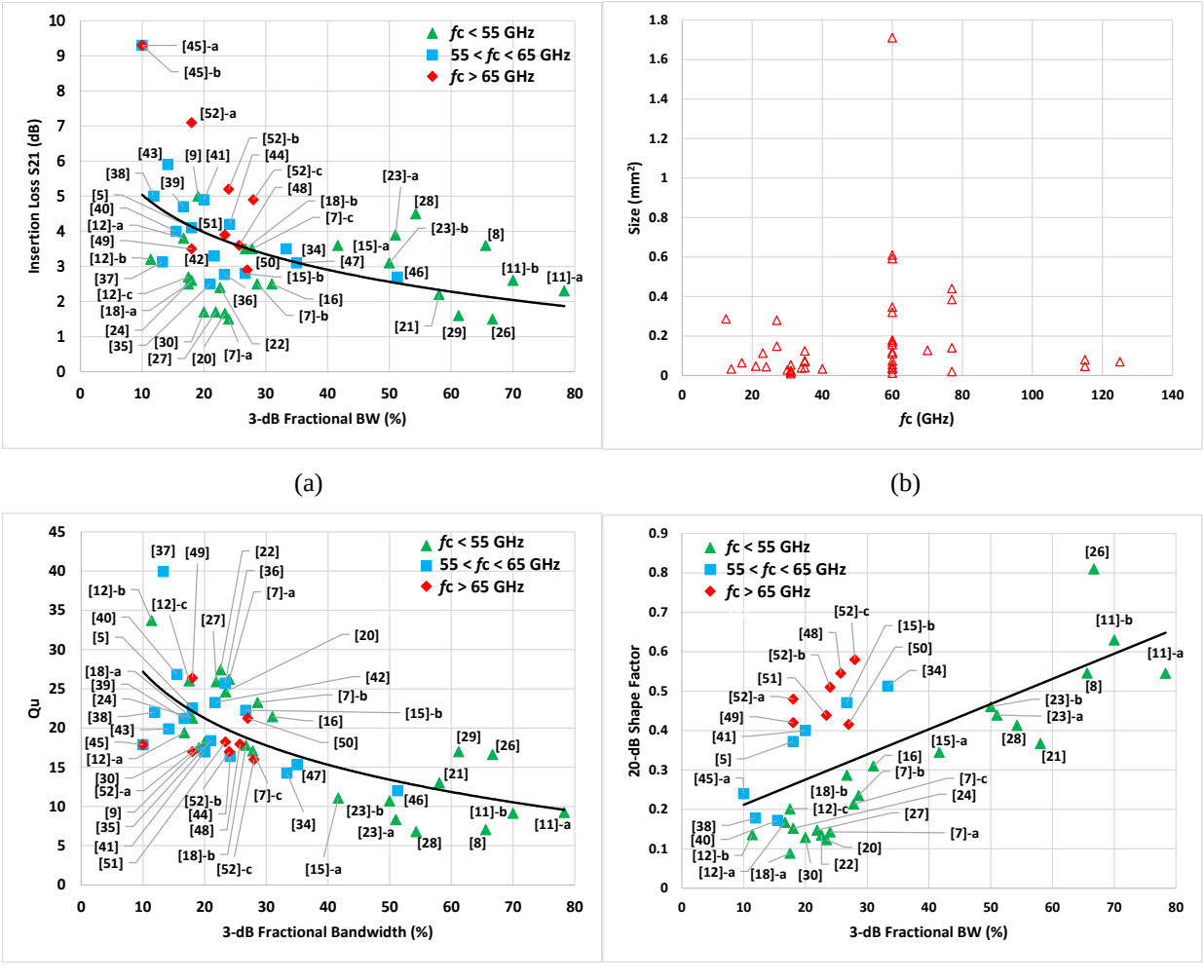

(a) (b)

(c) (d)

Figure 1.8: (a) minimum S_{21} (dB) versus 3-dB FBW, (b) size (mm^2) versus fc, (c) Q_u versus 3-dB FBW, (d) shape factor versus 3-dB FBW.

25 with FBW between 10 % and 30 %. Only two works, [12-c] and [37], have high Q_u of 34 and 37, respectively, but with very bad selectivity and rejection levels. Filters in [52] that operate at 120 GHz, have Q_u around 17. It is very interesting to check that in order to expect the design challenges beyond 100 GHz. As mentioned before, this comparison is not really accurate because Q_u depends normally on the technology used, which is not taken into consideration with this plot. In particular, CMOS technologies have different heights for BEOL, which directly effects the achieved Q_u even for the same filter configuration. Last but not least, most of the filters have an average chip size below 0.15 mm^2 with some filters of ultra-compact size below 0.02 mm^2.

In comparison to the operating frequencies, more than 80 % of the presented works operate below 55 GHz, along with 15 % at around 70 GHz and few works above 100 GHz. This indicates that filters' behavior is not well discovered at very high frequencies. Actually, it comes from the fact that defined applications are still few over this band. Moreover, researchers whom are working on the filters synthesis, are still relatively far from microelectronics technologies, and its many constraints. However, since applications begin to emerge beyond 60 GHz, with medical monitoring or automotive radars and the back-haul for the future 6G telecommunication standard, as already mentioned in the introduction, it becomes necessary for our research community to be proactive in demonstrating the possibility to create filters with acceptable performances, which could be integrated into mm-wave front-ends. Moreover, the frequency band beyond 100 GHz is certainly little used today, and one might think that the filtering behavior of amplifiers is sufficient, but this will probably no longer be true when the operating frequency of many systems gradually increases. Secondly, it always proves dangerous to compare the performance of passive circuits (and even active ones) realized using different technologies from microelectronics. As we show later, the quality factor of a patch or TLines depends enormously on the thickness of the BEOL of the technology, so the performance sometimes turns out to be much more linked to the specificities of the technology rather than to the quality and to the originality of the design.

Nevertheless, and despite the two critical points just mentioned, this comparison is made to discuss the main challenges of filters design at mm-waves. It shows that designing a narrow band filter with FBW below 20% and low insertion loss is considered the key

challenge. In addition to that, especially for filters that operate at f_c > 65 GHz, they should have a very good selectivity at lower out-of-band rejection in order to suppress responses below 40 GHz because for the moment most of 5G frequency allocations are at this band, along with satellite communications. The third challenge is to design filters with specific applications in mind especially for those above 60 GHz. This can lead to completely different sets of design specifications, for example to reject specific frequency bands or provide notches at certain frequencies.

Skimming the topologies used with the presented filters, it appears that only filters with TLine resonators or coupled-line resonators were used. So, and to our best knowledge, filters at mm-wave bands with patch resonators topology are not recorded. Then it is interesting to check its potentiality with integrated circuits like BiCMOS, as explained in the coming subsection.

1.3. General Patch Resonator Analysis on BiCMOS 55 nm

STMicroelectronics offers two versions of BiCMOS 55 nm (B55) technology with different BEOL, i.e. 8ML and 9ML EVO. The choice of this high-performance technology was guided by the frequencies that were considered for the realized filters, i.e. beyond 150 GHz, for which transistors, having figures of merit (f_{max} and f_t) greater than 400 GHz, are necessary in order then be able to produce active circuits (LNA and PAs) with acceptable performance in terms of gain.

The overview structures of the 8ML and 9ML BEOL are shown in Figure 1.9 (a) and Figure 1.9 (b), respectively. The obligation of confidentiality does not allow us to disclose the thicknesses and conductivities of all metals, or even the dielectric constants of the materials between the metal layers. The BEOL consists of 8 and 9 copper layers: (M1 to M8U) for 8ML and (M1 to M9V) for 9ML, along with one top aluminum layer (AluCAP AP) for both. All metal layers are dipped in oxide, and each two consecutive metal layers are separated by dielectric layers stack with different relative dielectric constant ε_r. Usually most of circuits that use B55 8ML technology, are implemented at M8U layer since it is the thicker (h_{M8U} = 3 µm), but AP (h_{AP} = 1.45 µm) seems to be useful too, since it makes the BEOL thicker as will be seen further. Moreover, the B55 9ML will be used in this dissertation for first time, because it was just released by the manufacturer. The advantage

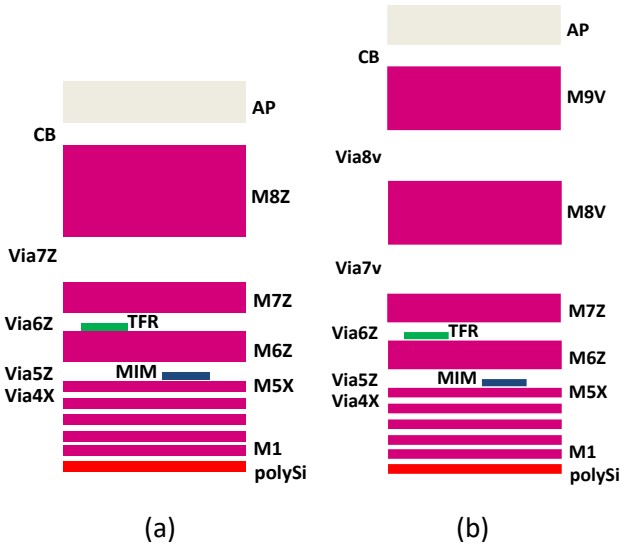

Figure 1.9: BiCMOS 55-nm Technology Back-End-Of-Line. (a) 8 Metal Layers, (b) 9 Metal Layers.

of using this version is simply due to the thicker BEOL, which improves Q_u, as will be discussed in this subsection.

In order to check the potentiality of B55 technology with patch resonators, Q_u is plotted for different patches' layouts (Rectangular R, Circular C, Hexagonal H and Octagonal O), as shown in Figure 1.10 (a). The 8ML version is used with all patches, which are implemented on M8U with ground on M1. Q_u is extracted at 100 GHz and 200 GHz from (1.3) with weakly loaded patches (insertion loss > 30 dB):

$$Q_u = \frac{f_c}{FBW} \tag{1.3}$$

where f_c is the center frequency and FBW is the 3-dB fractional bandwidth. All of them have approximately the same Q_u of 13.5 and 22 at 100 GHz and 200 GHz, respectively. Nevertheless, R has the smallest area size of 0.12 mm^2 at 200 GHz among them all (Figure 1.10(b)). So for the moment, we are going to use the rectangular patch resonator to design bandpass filter at first stage. Then with optimization, layout modifications might occur to achieve better performance.

In order to illustrate on the effect of BEOL thickness, Q_u of single patch resonator operating at 200 GHz is plotted in Figure 1.11 (a) for substrate height sub_h variation. The patch is implemented on different stacks from 8ML and 9ML as follows: M9v:M1, M9v:M6z, AP:M1 and AP:M6z. Note that AP, M6z and M1 have same thickness in both

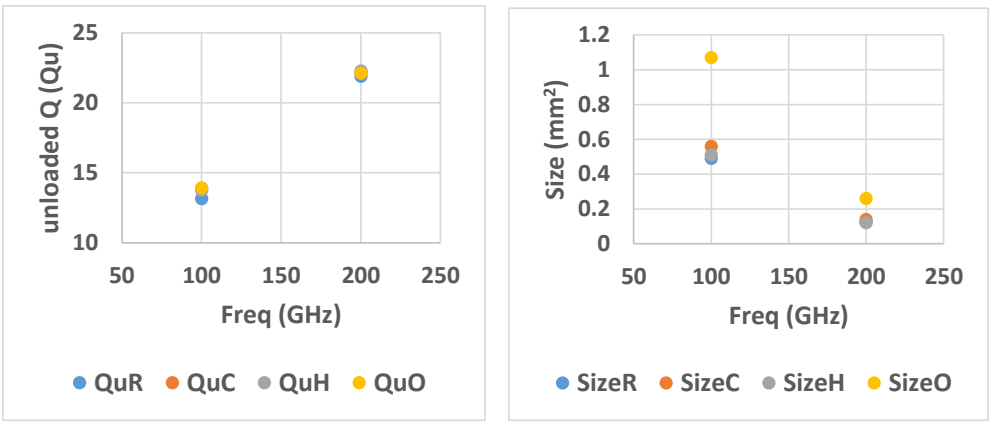

(a) (b)

Figure 1.10: Unloaded quality factor Q_u and size of different patch resonators at 100 GHz and 200 GHz.

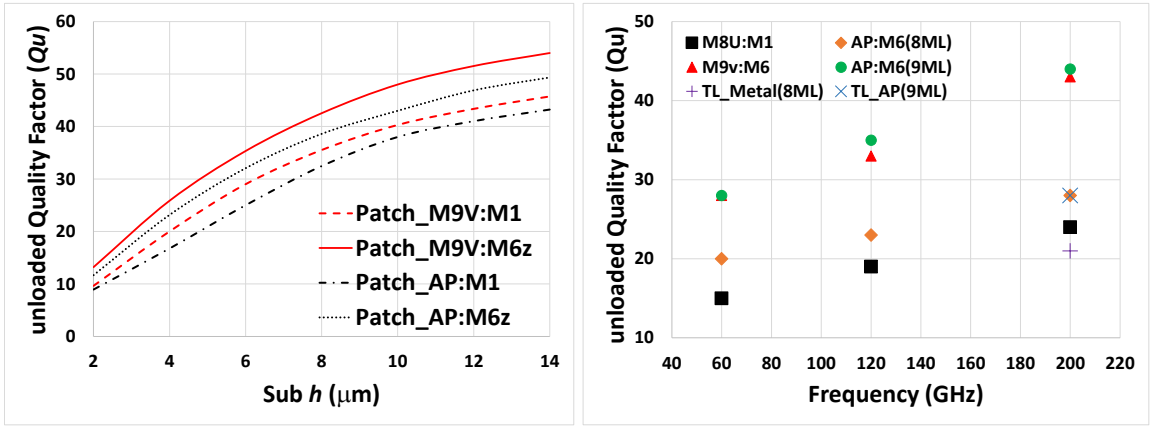

(a) (b)

Figure 1.11: (a) Q_u versus sub_h at f_c = 200 GHz, (b) Q_u at f_c = 60 GHz, 120 GHz and 200 GHz for selected stacks.

8ML and 9ML versions. This configuration leads to deep analysis for the effect of metal conductivity (between copper and aluminum) and layer's thickness on the extracted Q_u. It is obviously shown that for all configurations, extracted Q_u is increasing with sub_h. For example, with M9v:M1, it varies from 10 with sub_h = 2 µm up to 43 with sub_h = 14 µm. Moreover, when GND layer becomes thicker (in case of M6z use), Q_u improves to 14 and 54, respectively. It is of same behavior for the patch implemented at AP.

Next, for an exact extraction of Q_u for the selected layers, single patch resonators were implemented on each stack to be operating, individually, at f_c = 60 GHz, 120 GHz and 200 GHz, respectively. The dimensions are summarized in Table 1.3 along with the width (W_{TL}) of a 50-Ω TLine implemented on each stack. Note that for the 8ML BEOL, it couldn't be possible to select M6z layer for GND instead of M1 because sub_h would have

Table 1.3: Selected BEOL stacks.

STACK	Approximate Height (sub_h)	50-Ω TLine (W_{TL})
M8U:M1	6 µm	7.7 µm
AP:M6z (8ML)	7 µm	10.5 µm
M9v:M6z	8 µm	12 µm
AP:M6z (9ML)	11 µm	19 µm

been very small, thus increasing the losses. The results are plotted in Figure 1.11(b). It shows that Q_u is linearly increasing with frequency, and that the best achieved results are for the AP:M6z stack from 9ML version with Q_u values of 28, 35 and 44, respectively. This is due to the thicker constructed BEOL. This doesn't contradict with the results in Figure 1.11(a), where M9v:M6z shows higher potential with BEOL height than other because in reality sub_h of 11 µm corresponding to AP:M6z, cannot be constructed with the available M9v and M6z layers. Moreover, results in Figure 1.11(b) show that there is a big improvement in performance when using 9ML version with patch resonators (and also TLines). For example, in comparison to AP:M6z for both versions, a difference of 11 in Q_u is occurred. It is a significant improvement for passive resonators. This will be thoroughly analyzed and compared later when presenting the proposed filters.

Next, for more illustration on the potentiality of B55 technology with different BEOL, two 50-Ω mirostrip lines (TL-Metal and TL-AP) were implemented at M8U (from 8ML) and AP (from 9ML) layers with GND at M1 and M6z, respectively. The width $W_{TL-Metal}$ and W_{TL-AP} are 7.7 µm and 19 µm for M8U:M1 and AP:M6z stacks, respectively. The achieved results were extracted at 200 GHz, and are shown in Figure 1.11(b). The Q_u equals 21 and 28 for sub_h around 6 µm and 10 µm, respectively. In comparison to Q_u for patch resonator, it is observed that the usage of patch resonators leads to better performance than TLines. Note that it is clear that the width W_{TL} is increasing with the BEOL. This could have a double impact for mm-wave filter design based on TLlines topologies. It is a kind of compromise between better Q_u and higher design complexity, since, for large W_{TL}, meandering and junctions become less flexible in design. This issue and others can be solved by using patch resonators instead.

1.4. Conclusion and Design Challenges

This chapter presented the state-of-art for main patch filter designs that were conducted at RF and microwave bands, in order to show the techniques used to gain flexibility in controlling the filters responses. It was underlined that patch resonators with grounded *vias* can have high miniaturization capabilities, which is necessary for integrated filter design. On the other side, a full review for most of the recorded filters at mm-wave bands was conducted. The results show that the achieved dominant FBW is between 25 and 30 %. So, it is clearly a key challenge, at mm-wave bands, to design narrow band filters with FBW below 20% and acceptable losses.

Patch resonators, which were not used before for mm-wave filters, are implemented on BiCMOS 55 nm integrated technology to check their potentiality. The results show that Q_u is increasing with BEOL height and frequency, and reaches, for specific stack, 53 at 200 GHz. At this frequency, the extracted Q_u for patch resonators is better than TLines-based resonators. Also, the filter design with TLine resonators becomes more complex. Thanks to the availability of multi-layering BEOL with several thick metals, different designs for patch filters with dual-mode responses can be developed, as demonstrated in the next chapter.

CHAPTER II: PATCH RESONATOR DESIGN PRINCIPLES AND SYNTHESIS

The theory of bandpass filters based on patch resonators is well developed, but the key design challenge is relied on understanding its electro-magnetic (EM) fields distribution behavior and how each resonance mode can be perturbed independently. In this context, this chapter presents a full description of the patch resonator design principles along with its modes behavior. Also the detailed explanation of the synthesis design methodology that will be used further for designing dual-mode filters at mm-wave bands with grounded *vias* is conducted.

2.1. Square Patch Resonator Principle

2.1.1. Conventional Square Patch Resonator

The conventional square patch resonator in Figure 2.1 acts as a wheeler cavity with perfect electrical walls in the top and bottom metallic layers while surrounded by magnetic walls provided by middle dielectric layer. The EM modes existing inside the patch are the Transverse Magnetic (TM^{z}_{mn}), where m and n are the order of the modes. It is defined that only electric field E exists in the z direction, which is perpendicular to the ground plane. The EM modes and their corresponding resonance frequencies can be extracted from Maxwell equations as for patch antenna, which are summarized in (2.1) and (2.2), respectively [77]:

$$\left\{\begin{array}{c} E_z = \sum_{m=0}^{\infty}\sum_{n=0}^{\infty} A_{mn}\cos\left(\frac{m\pi}{L_{ef}}x\right)\cos\left(\frac{n\pi}{L_{ef}}y\right), \\ H_x = \left(\frac{j\omega\varepsilon_{reff}}{k_c^2}\right)\left(\frac{\partial E_z}{\partial y}\right), H_y = -\left(\frac{j\omega\varepsilon_{reff}}{k_c^2}\right)\left(\frac{\partial E_z}{\partial x}\right), \\ k_c^2 = \left(\frac{m\pi}{L_{eff}}\right)^2 + \left(\frac{n\pi}{L_{eff}}\right)^2, \end{array}\right\} \tag{2.1}$$

$$f_{mn\,0} = \frac{c}{2L_{ef}\sqrt{\mu_r\varepsilon_{eff}}}\sqrt{(m)^2 + (n)^2} \tag{2.2}$$

where A_{mn} is the mn mode E field magnitude, m and n are infinite non-negative and non

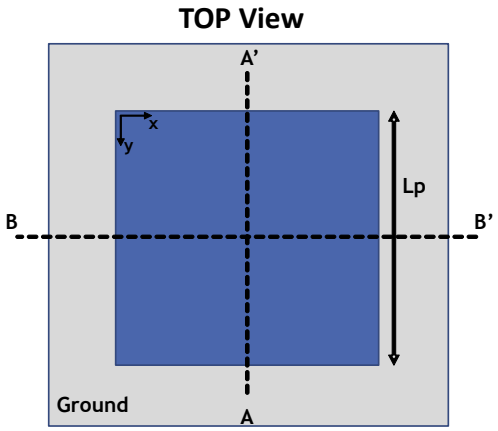

Figure 2.1: Conventional Patch Resonator.

both-zero integers TM_{mn}^{z} mode indices corresponds to *x* and *y* axis directions, ω is the frequency, k_c is the wave number, *c* is the light speed in vacuum, μ_r is the relative magnetic permeability ($\mu_r = 1$), ε_{eff} is the effective permittivity and L_{eff} is the effective length of the patch with:

$$\left\{\begin{array}{c} L_{eff} = L_p + \left|2\Delta L_p\right| \\ \Delta L_p = 0.412h\left(\frac{\varepsilon_{reff}+0.3\frac{L_p}{sub_h}+0.264}{\varepsilon_{reff}-0.258\frac{L_p}{sub_h}+0.8}\right) \\ if\ m=0\ or\ n=0\text{: } \varepsilon_{reff} = \varepsilon_{reffauxiliar} \\ \text{otherwise: } \quad \varepsilon_{reff} = \frac{\varepsilon_{reffauxiliar}}{\varepsilon_r} \\ \text{with: } \varepsilon_{reffauxiliar} = \frac{1}{2}\left[\varepsilon_r + 1 + \frac{\varepsilon_r - 1}{\sqrt{1+10\left(\frac{h}{L}\right)}}\right] \\ \boldsymbol{L_p} \text{ rectangular patch length, } \boldsymbol{sub_h} \text{ substrate height and } \boldsymbol{\varepsilon_r} \text{ is the substrate relative permitivity} \end{array}\right\} \quad (2.3)$$

The first two modes, TM_{01} and TM_{10}, are considered the fundamental modes of the patch and their resonance frequency, which appears at $\lambda/2$ is:

$$f_c = f_{01} = f_{10} = \frac{c}{2L_{eff}\sqrt{\mu_r \varepsilon_{reff}}} \quad (2.4)$$

These modes are naturally combined, and their splitting depends on perturbations, which

Table 2.1: Extracted E field and resonant frequency equations of first 3 pair modes of patch cavity.

m ; n	E Field	Resonant Frequency
m = 0 ; n = 1	$A_{010}cos(\frac{\pi}{L_{ef}}y)$	$f_{010} = \frac{c}{2L_{ef}\sqrt{\varepsilon_{reff}}}$
m = 1 ; n = 0	$A_{100}cos(\frac{\pi}{L_{ef}}x)$	$f_{100} = \frac{c}{2L_{ef}\sqrt{\varepsilon_{reff}}}$
m = 1 ; n = 1	$A_{110}cos(\frac{\pi}{L_{ef}}x)cos(\frac{\pi}{L_{ef}}y)$	$f_{110} = \sqrt{2} \times \frac{c}{2L_{ef}\sqrt{\varepsilon_{reff}}}$
m = 1 ; n = 0	$A_{200}cos(\frac{2\pi}{L_{ef}}x)$	$f_{200} = 2 \times \frac{c}{2L_{ef}\sqrt{\varepsilon_{reff}}}$
m = 3 ; n = 0	$A_{300}cos(\frac{3\pi}{L_{ef}}x)$	$f_{300} = 3 \times \frac{c}{2L_{ef}\sqrt{\varepsilon_{reff}}}$

generate coupling between them. Their E fields equations and those for higher order modes are presented in Table 2.1. A general observation to the extracted equations allows to configure that each mode has its specific field distribution along the patch area, which in some cases appears to be uncoupled. For TM_{01} it is defined along *y*-axis while TM_{10} is along *x*-axis, where both modes are orthogonal to each other. Also, their electric fields change their phase for π along the patch. Therefore, theoretically, both modes have maximum electric field at the edges of the patch along their axis of definition and null in the middle. The first higher order mode, TM_{11} appears at $f_{11} = \sqrt{2}f_c$ GHz, where E field equation shows a maximum E field at the 4 corners of the patch and null in the middle. Afterwards, a generation of pair modes started to appear at resonance of $i \cdot f_c$, where i is 2, 3, 4… etc. At the moment, higher order modes are out of interest.

For more illustration on the field distribution of the patch resonator in Figure 2.1, the *eigenmode* solution solver from ANSYS HFSS software was used to derive the E field and surface current J of the first 3 resonance frequencies, corresponding TM_{01}, TM_{10} and TM_{11} modes, respectively, which are presented in Figure 2.2 (a), (b) and (c), respectively. The E field distribution of each mode allows to determine its area of definition along the patch, which helps in specifying the best feeding point to excite it. While J flowing direction allows to determine its electrical length in order to efficiently insert the suitable perturbation element for resonance frequency controllability. TM_{01} mode has maximum E field at the top and buttom edges of the patch resonator and null in the middle, as shown in

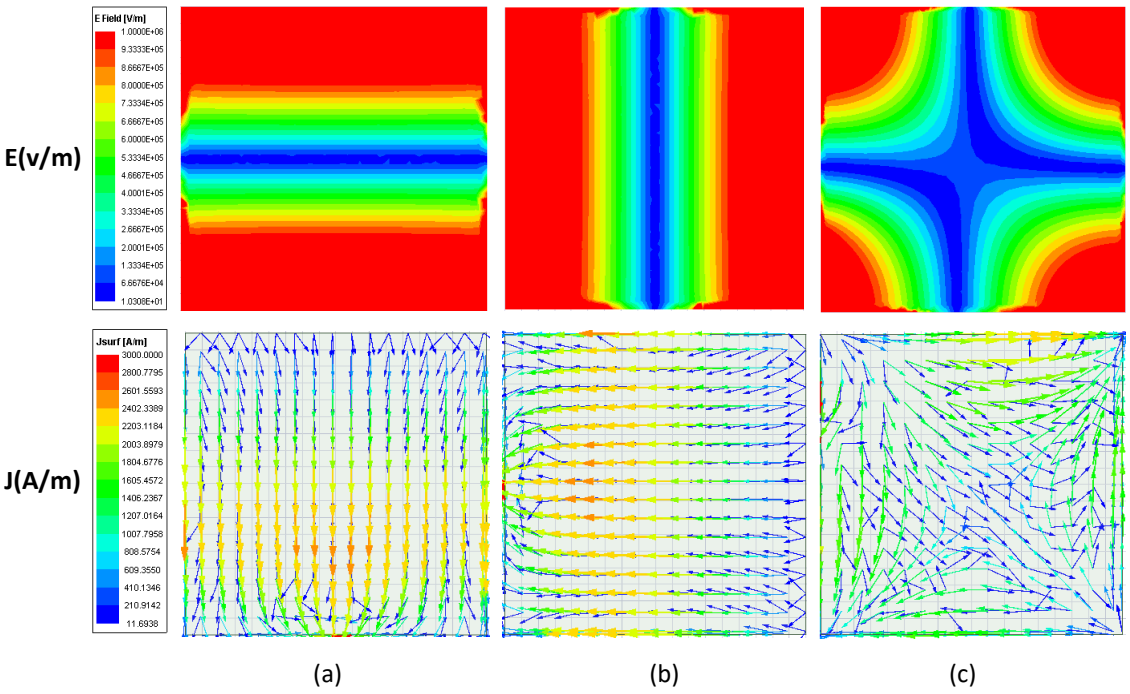

Figure 2.2: Electric-Field and Surface-Current distribution of: (a) TM_{01}, (b) TM_{10} and (c) TM_{11} modes of rectangular patch resonator.

Figure 2.2 (a). Its J flows vertically along the *AA'* axis with maximum in the middle. It is obvious that when E field is maximum, we found J as minimum, since for lossless passive circuits, the electrical and magnetic fields are 90° out of phase. In this case, perturbations can be either inserted in the middle of the patch for J disturbance, or at the edges for E field disturbance, as well. The same behavior is recorded for TM_{10}, but with orthogonal fields distribution defined along *BB'* axis. This orthogonality between TM_{10} and TM_{01} is due to the symmetry of the square patch resonator. As mentioned before, TM_{11} is defined at the 4 corners of the patch resonator, with J flowing at the edges and towards the corners (top-left and bottom-right).

For demonstration, a patch resonator of L_p = 360 µm is implemented on B55 8ML technology using ANSYS HFSS software. The patch is weakly coupled through two-port structure and designed at M8U layer with ground at M1. Figure 2.3 shows the transmission coefficients S_{21} (dB) for all the resonance frequencies within the band from DC up to 600 GHz. The first resonance frequency appears at f_c = 200 GHz, which refers to the fundamental modes (TM_{01} and TM_{10}). TM_{11} resonance frequency appears at 280 GHz, which is approximately equal to $\sqrt{2} \cdot f_c$ and TM_{20} resonance frequency appears at 400 GHz

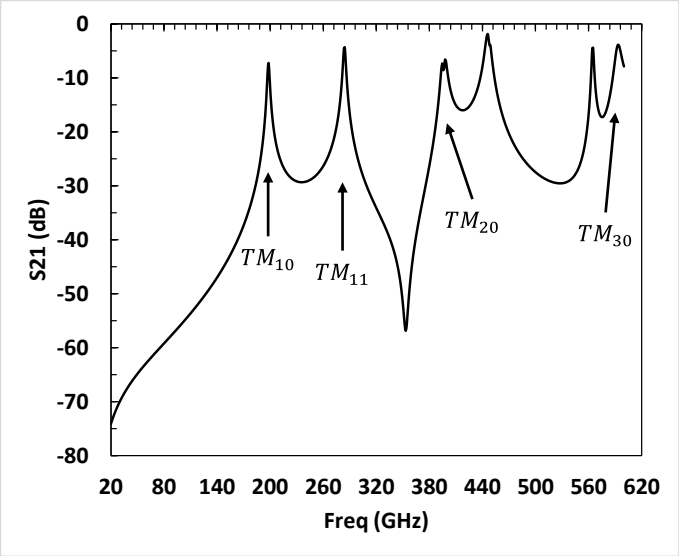

Figure 2.3: Transmission response S_{21} of conventional patch resonator's modes.

which is $2 \cdot f_c$. It is worth to mention that at such high frequency band the only way to verify the simulated results for patch resonator, before the measurements, is by comparing it to the theoretical calculations because, for our best knowledge there is no records in the literature for patch resonators responses.

2.1.2. Grounded Square Patch Resonator

One of the weakness of patch resonators is their size compared to other topologies. As seen in the literature, different techniques were used to reduce its size, but the most efficient way is by inserting shorting posts (*vias*). The usage of *vias* has two main impacts: first it adds a new resonance mode to the patch recalled *LC-mode,* and second it perturbs the conventional existing modes. *LC-mode* is electrically modeled as $L_{via}C_{via}$ circuit, where the inductance L_{via} depends on the *via*'s self-inductance, and the capacitance C_{via} depends on the patch capacitance C_p. *Via* has a direct impact on the overall size of the patch through adding a new lower resonance frequency $f_{LC-mode}$, which allows patch compactness. Also, it perturbs the natural existing modes, especially when it splits the fundamental modes (this will be discussed further). It is worth to mention that $f_{LC-mode}$ is mainly controlled by the size of the *via* and its position along the patch. Figure 2.4 (a) shows the electrical model, exclusively, for TM_{10} mode from the conventional patch resonator presented in Figure 2.3,

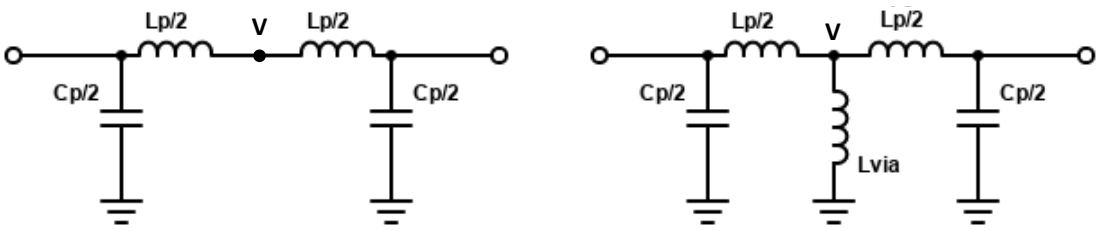

(a) (b)

Figure 2.4: Electric model: (a) Conventional patch resonator (TM_{10}), (b) Grounded patch resonator.

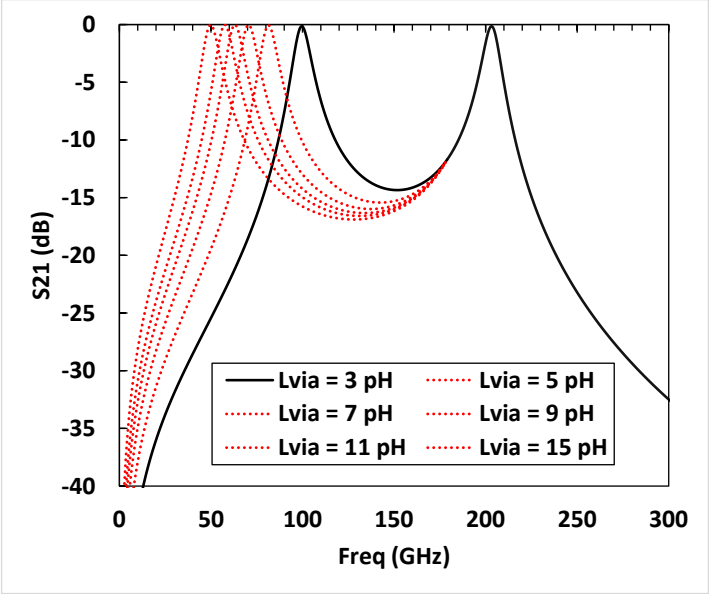

Figure 2.5: Transmission coefficient variation of the *via* electric model.

and Figure 2.4 (b) shows the electrical model of the same patch but with grounded *via* in the middle. This model is true only if the *via* is placed in the middle of the patch along *AA'* axis, where TM_{10} has null E field and is not perturbed. Using the *Maxwell 3D* tool from ANSYS HFSS, C_p and L_p were extracted and recorded 0.64 pF and 3.91 pH, respectively. Then the circuit model in Figure 2.4 (b) was simulated using Keysight ADS software to check the effect of tuning L_{via}. The transmission coefficient S_{21} (dB) is plot in Figure 2.5 vs frequency from DC to 300 GHz. The resonance mode TM_{01} is fixed and unchanged at f_c = 200 GHz, while $f_{LC-mode}$ varies from 100 GHz to 50 GHz when L_{via} changes from 3 pH to 15 pH, respectively. It indicates that when L_{via} is increasing, $f_{LC-mode}$ is intuitively decreasing. Therefore, this behavior allows a big reduction of the overall size of the patch if the *via* is well designed and placed.

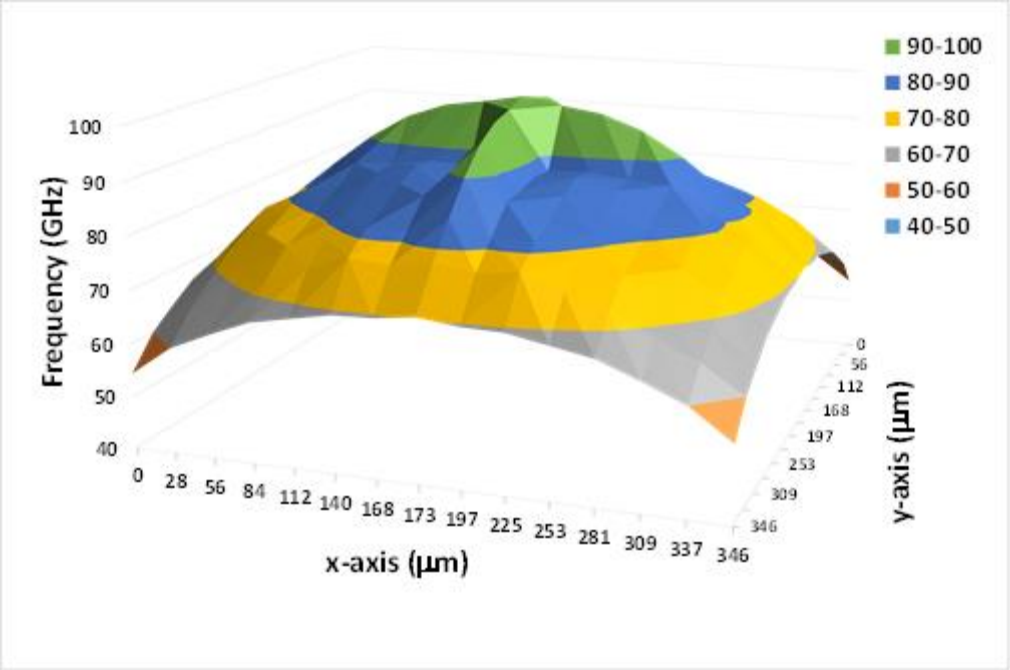

Figure 2.6: $f_{LC-mode}$ variation with the position of the via along the patch area.

In order to have a more practical and general view on the effect of different positions of the *via*, Figure 2.6 shows the variation of $f_{LC-mode}$, which is extracted from the *EM* simulation of a single *via* inserted simultaneously across the whole area of the patch resonator presented in Figure 2.1. It can be noticed that $f_{LC-mode}$ varies from 50 GHz to 100 GHz when the *via*'s position is changed along the patch. The lowest resonance frequency is achieved when the *via* is placed at the corner of the patch while the highest resonance frequency is achieved when the via is placed at its middle. Moreover, $f_{LC-mode}$ doesn't change uniformly across the whole area. Its variation across the diagonal axis is different and higher from those along the *AA*' or *BB*' axis, accordingly. That means the inductance L_{via} is higher when the *via* is moved along the diagonal axis. Hence, to highlight physicaly about this idea, 3 positions of via_{middle}, via_{top}, via_{corner} are selected and their configuration with patch resonator is shown in Figure 2.7(a), (b) and (c), respectively. Also, their E field and surface current J are shown in Figure 2.8(a), (b), and (c) respectively. Generally, a grounded via has a uniform or even E field distribution across the patch resonator except at its position where the E field is null. On the other hand, J flows radially across the patch starting from the *via* position, where it is maximum because *via* is purely inductive and shorted, towards the corners where E field is maximum. For the via_{middle},

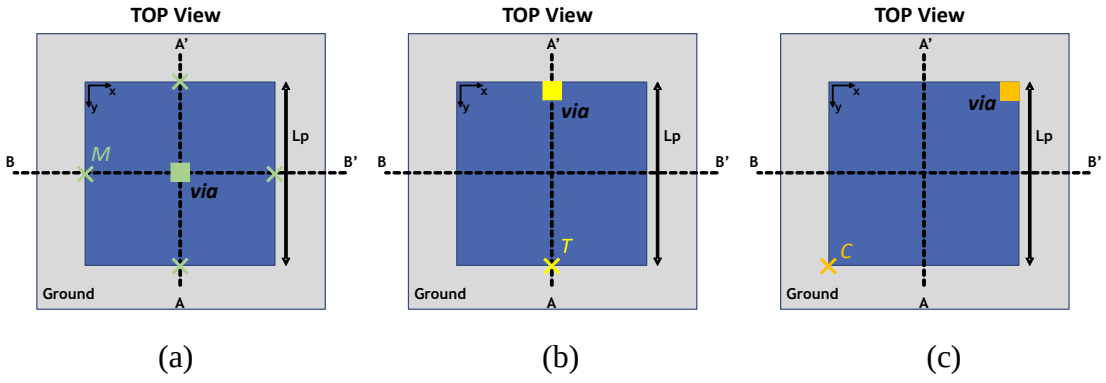

Figure 2.7: Grounded patch resonator with: (a) via_{middle}, (b) via_{top}, and via_{corner}.

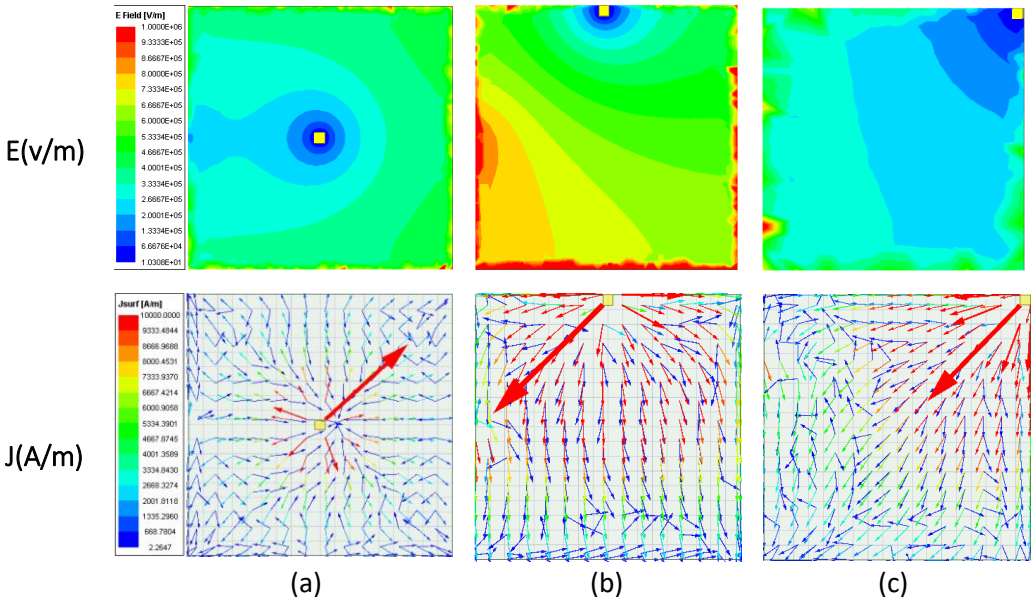

Figure 2.8: *E* field and *J* current for: (a) via_{middle}, (b) via_{top}, and via_{corner}.

it flows from the center *O* of the patch towards all edges, with a minimum physical length L_{OM} being at point *M*. The minimum physical length is chosen where *J* becomes null and *E* field is maximum, because at that point the excitation ports should be connected, as will be illustrated further. As for via_{top}, *J* flows from the top of the patch towards the edges of the patch with minimum physical length L_{OT} at point *T*. Last but not least, for via_{corner}, *J* flows form the corner to the other edges of the patch with minimum physical length L_{OC} at the symmetrical corner with point *C*. Their resonance frequencies $f_{via-middle}$, $f_{via-top}$ and $f_{via-corner}$ are equal to 100 GHz, 70 GHz and 50 GHz, respectively. Thus, if the patch resonator's size has to be reduced and stay resonating at 200 GHz, its side length L_p will

be changed from $\lambda/2$ to $\lambda/4$, $\lambda/5.7$ and $\lambda/8$, respectively. The miniaturization percentage $\%M$ can be calculated from (2.5).

$$\%M = (1 - \frac{AS_{miniature-Filter}}{AS_{conventional-Filter}}) \times 100 \quad (2.5)$$

where AS is the surface area of the patch resonator.

In this cases a massive area reduction of 94 % could be reached if the via is integrated at the corner.

2.1.3. Input/Output Feeding and External Quality Factor

Usually, to excite a specific mode inside the patch resonator, Input/Output (I/O) feeding ports should be placed at its maximum E field or at a so-called radiating edge, otherwise this mode doesn't appear. By changing the I/O ports along its axis of definition, the input impedance $Z_{in-TMmn}$ of a given mode changes accordingly, and this leads to a variation in the external quality factor Q_e. So, the feeding position should be chosen carefully because in some designs only "single point" could be efficient.

I/O Feeding

In order to illustrate more on the Z_{in} variation with I/O, a conventional square patch resonator (Figure 2.9) of L_p = 360 µm is fed by a single port P_1, which is deviated by distance D_t from the center of the patch. When P_1 is at the middle of the patch (D_t = 0 µm), only TM_{10} is excited with f_{TM10} = 200 GHz as shown in Figure 2.10(a), while other modes

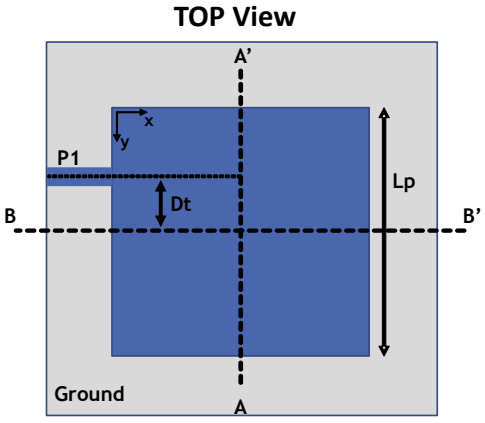

Figure 2.9: Square patch resonator with a single feeding port P_1.

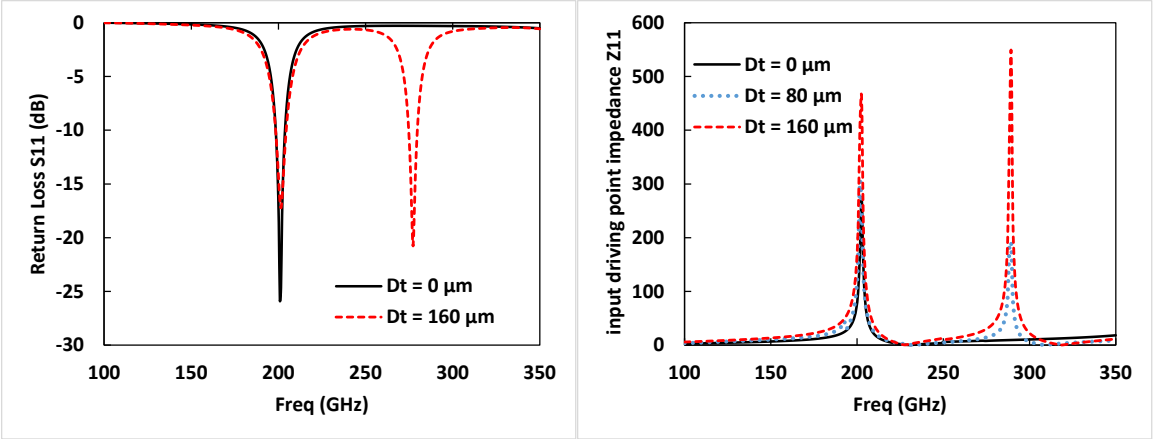

(a) (b)

Figure 2.10: Return loss S_{11} (dB) of square patch resonator with single port P_1 variation.

TM_{01} and TM_{11} are not appearing. According to the E field in Figure 2.2, TM_{10} has maximum E field at this position while TM_{01} and TM_{11} have null E field. However, when P_1 is moved upwards or downwards along the *AA'* axis and reaches the edges with D_t = 180 µm, TM_{10} and TM_{01} are both excited with single resonance f_c that appears at 200 GHz, because they are still uncoupled. Also TM_{11} is excited and resonates at 280 GHz. This variation of D_t allows to vary the input driving point impedance Z_{in} for the mode, and effectively for TM_{01} and TM_{11}, because their E field vary at P_1 alignment. When D_t = 0 µm, $Z_{in-TM01}$ = 0 as shown in Figure 2.10(b), while $Z_{in-TM10}$ is maximum. As D_t increases to 180 µm, $Z_{in-TM11}$ varies and reaches its maximum and so TM_{11} is highly excited. It is worth to mention that $Z_{in-TM10}$ is constant until D_t = 80 µm, then it increases gradually (see Figure 2.10 (a) at 200 GHz) because from this point both TM_{01} and TM_{10} are now excited. Therefore, the position of the feeding port allows to have flexible responses to meet the needed criteria.

In practice, patch resonators are excited by two 50-Ω feeding ports P_1 and P_2. They might have different types of configurations, but the most common ones are the collinear 180° and the orthogonal 90° structures, as shown in Figure 2.11 (a) and (b), respectively. In collinear configuration, the behavior of the modes and their field distribution are those discussed earlier in this chapter, while for the orthogonal configuration, fields distribution of the fundamental modes are rotated by 45° as shown in Figure 2.12. This rotation is due to the change of the axis of symmetry from horizontal or vertical axes to the diagonal axes.

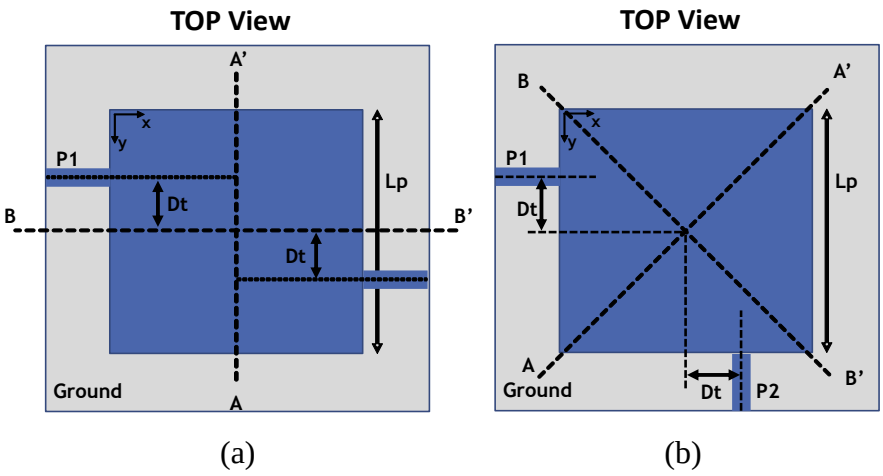

Figure 2.11: Patch resonators with: (a) collinear configuration and (b) orthogonal configuration.

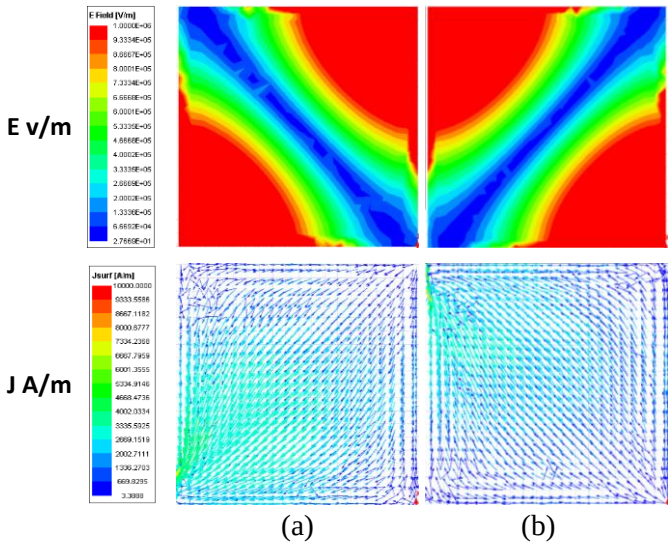

Figure 2.12: E field and surface current distribution with orthogonal port configuration of: (a) TM_{01} and (b) TM_{10}.

The surface current J of TM_{01} and TM_{10} flows diagonally along the *AA*' and *BB*', respectively. The 90° configuration is more flexible with perturbations where both fundamental modes can be excited at the same time. In this case, they are recalled as the *even*- and *odd*-modes. TM_{01} is the *even*-mode and TM_{10} is the *odd*-mode because P_1 and P_2 are at the same potential E for TM_{01} while they are in differential with TM_{10}. This will be more elaborated in chapter III when discussing the dual mode filter design.

External Quality Factor

The flexibility in varying the position of the I/O ports, allows to determine the external

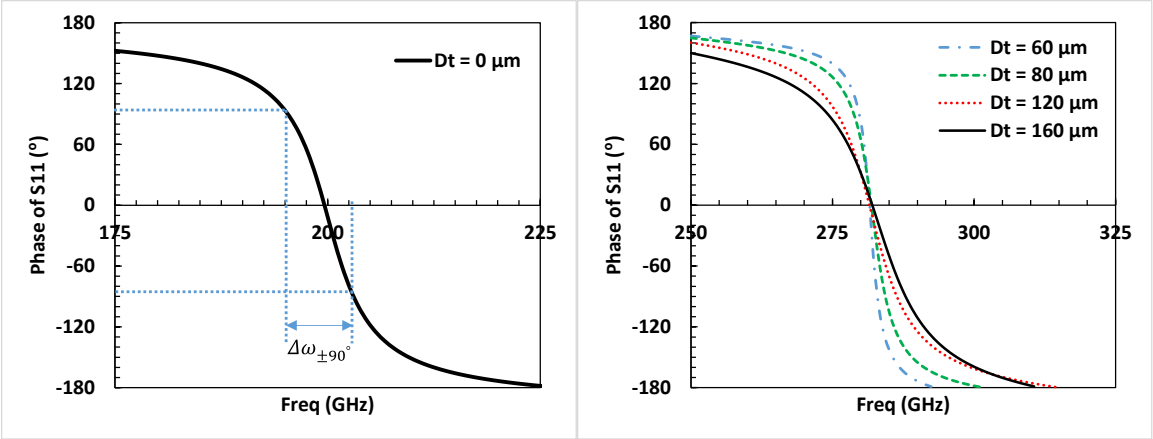

(a) (b)

Figure 2.13: Phase variation of: (a) TM_{10} and (b) TM_{11}.

quality factor Q_e variation. It is an important parameter for building the synthesis of the filter. Q_e represents the strength of coupling between a resonant TM mode and the input signal. Usually, Q_e is extracted using a single port structure as in Figure 2.9 and its value is calculated from (2.6) [77]:

$$Q_e = \frac{\omega_0}{\Delta\omega_{\pm 90^\circ}} \tag{2.6}$$

where ω_0 is the resonance frequency and $\Delta\omega_{\pm 90^\circ}$ is determined from resonance frequency at which the phase shift is equal to $\pm$ 90° with respect to the absolute phase at ω_0. Taking the example where only TM_{10} is excited (D_t = 0 µm), Figure 2.13 (a) shows the S_{11} (dB) and its phase φ_{TM10} (°) at 200 GHz. Q_e will vary when Z_{in} changes, it is not noticeable for TM_{10} with collinear feeding configuration, since it has uniform E field along AA' axis. However, it is not the case for TM_{11}, as shown in Figure 2.13 (b). When P_1 is moved toward the edges, its phase φ_{TM11} is widened with D_t, which increases $\Delta\omega_{\pm 90^\circ}$, thus Q_e varies and decreases accordingly.

2.1.4. Modified Patch Resonator

As mentioned above, patch resonators can support dual-mode concept through inserting perturbations across their axis of symmetry to create coupling between the degenerated modes and split them. Based on the presented techniques in CHAPTER I, this

subsection describes in details the effect of grounded *via*s, edge cut and cross slot integration on the resonance modes.

Vias

Grounded *via*s are only effective (from modes perturbation perspective), if they are inserted at $E \neq$ Null for a given mode. In this case, it has to be away from the center of the patch, as in the configurations of Figure 2.7 (b) and Figure 2.7 (c) where via is placed at top and corner, respectively. For more illustration about the effect of *via*, Figure 2.14 (a) and Figure 2.14 (b) show the first 4 resonance frequencies extracted from ANSYS HFSS software, for the presented modified patch resonator, respectively. Their equivalent E field distribution is shown in Figure 2.15. In case of *via* at top, the degenerated modes TM_{01} and TM_{10} are split with f_{TM10} unchanged at 200 GHz and f_{TM01} perturbed. Since *via* is shorted, then part of electric field for TM_{01} is decreased, thus f_{TM01} is shifted upwards. This is obvious when looking at its E field distribution in Figure 2.15 (b), where part of the fields are shorted. TM_{11} mode is unperturbed and resonates at f_{TM11} = 285 GHz. In via_{corner} configuration, where the *even*-mode TM_{01} and *odd*-mode TM_{10} E fields are defined and aligned along the diagonal axes, TM_{01} and TM_{11} are perturbed and split. The resonance frequency f_{TM10} is unchanged at 200 GHz since the E field of TM_{10} is null at the *via* position (Figure 2.15(g)), while both f_{TM01} and f_{TM11} are perturbed and shifted upwards. Therefore, as discussed earlier, for any *via* configuration, $LC - mode$ has a uniform E field

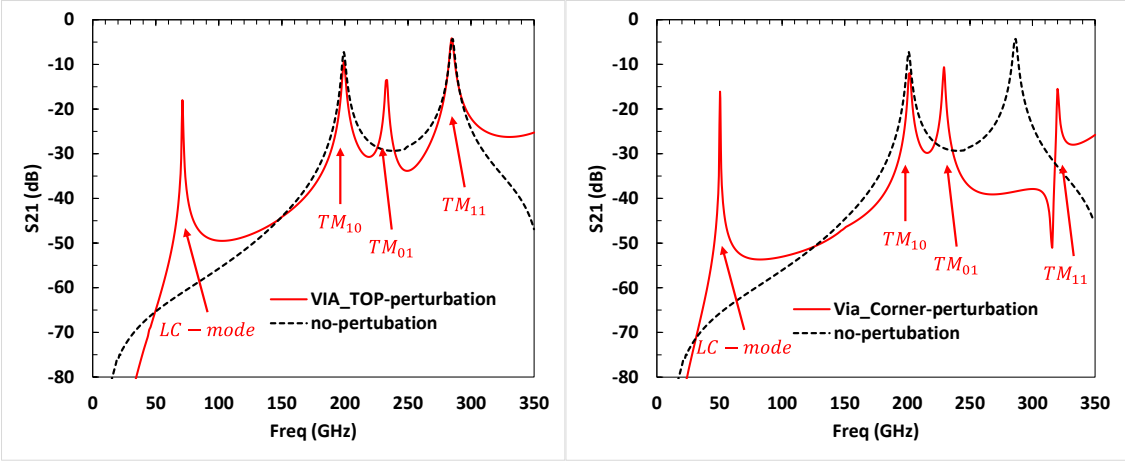

(a) (b)

Figure 2.14: First 4 resonance frequencies of grounded patch with configurations: (a) via_{top} and (b) via_{corner}.

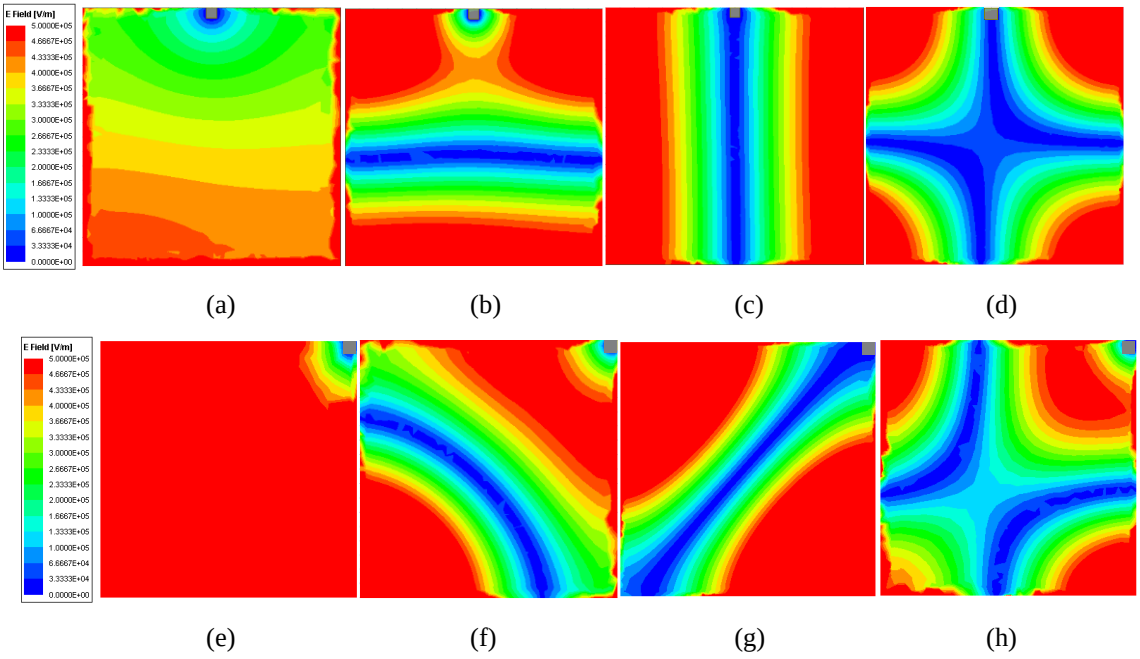

Figure 2.15: Grounded patch *E* fields with *via* top: (a) $LC-mode$, (b) TM_{01}, (c) TM_{10} and (d) TM_{11}; Grounded patch *E* fields with *via* corner: (a) $LC-mode$, (b) TM_{01}, (c) TM_{10} and (d) TM_{11}.

distribution outside the *via* (Figure 2.15 (a) and (e)). In regards to the higher modes, grounded *vias* affects their E field distribution, which shifts upward their resonance frequencies. It is worth to mention that this deformation in the E fields will have to be considered for the definition of the feeding ports position for given modes excitation.

Edge Cut

Perturbation through *Edge Cut* (inductive loading) is the conventional way of splitting the fundamental modes of the square patch resonators inspired from the capacitive loading technique *Edge extension* used with square loop resonators, as previously shown in Figure 1.3. Its configuration is shown in Figure 2.16 (a), where a square patch resonator is weakly loaded and modified with two square edge cuts of length cut_d along the diagonal axis of symmetry *AA*'.

Without any perturbation (cut_d = 0 µm), the fundamental modes are still uncoupled and not degenerated. In this case, and because of the orthogonal feeding, there is no bandpass response at the output of the resonator as shown from the insertion loss S_{21} plot in Figure 2.16 (b). Both modes operate at the same frequency with orthogonal phases. Then, when perturbation is added ($cut_d \neq 0$), the degenerated modes are split. The degree

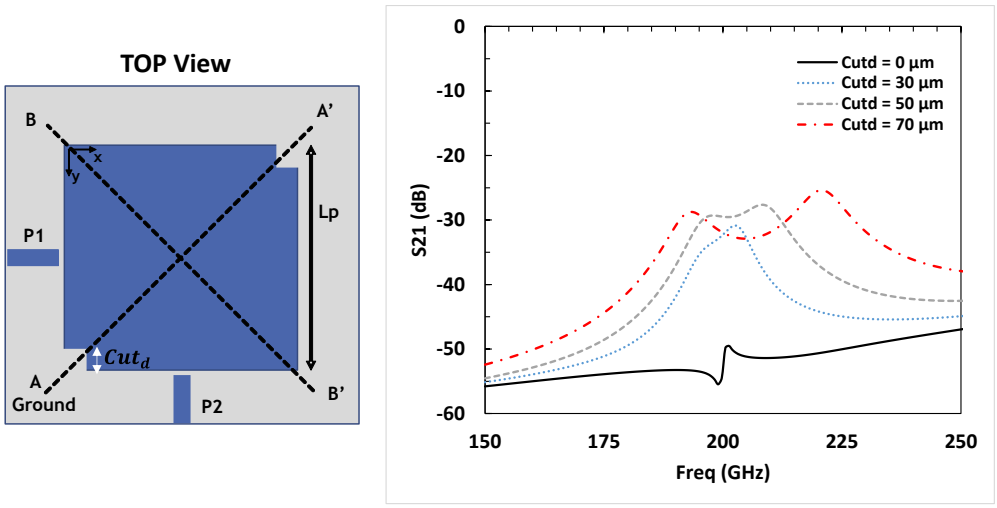

(a) (b)

Figure 2.16: (a) Patch resonator with *Edge cut*, (b) insertion loss S_{21} variation with Cut_d.

of coupling between modes is strongly linked to cut_d. For example, when cut_d is increased from 30 µm to 70 µm the splitting difference between degenerated resonance modes increases from 2 GHz to 28 GHz. This kind of perturbation doesn't have a lot of freedom since it is limited in the patch area and the performance cannot be flexible.

Cross Slots

It is the most used technique to split and control the degenerated modes. Adding more slot etches inside the patch resonator leads to more reduction in its overall size, which is an interesting feature for integrated circuits. Also, inserting slots in the design effectively helps in controlling the modes, once the perturbation is placed at the maximum J in order to disturb the current flow of a specific mode.

For demonstration, square patch resonator of L_p = 360 µm with symmetrical and asymmetrical cross slots is implemented with collinear and orthogonal feeding as shown in Figure 2.17 (a) and (b), respectively. Initially without any slot, the patch resonator in Figure 2.17 (a) operates at f_c = 200 GHz (for TM_{10} and TM_{01} modes). It includes symmetrical cross slots at *AA*' and *BB*' diagonal axes with length L_s. In order to check the effect of L_s variation on the f_c of the patch, a single mode TM_{10} is excited through the collinear feeding configuration. Current flow for TM_{10}, as shown before, is maximum at the middle of the patch along *x*-axis. On the contrary, when slots are inserted, current flow is now maximum at the edges of the slots as seen in Figure 2.18 (a), indicating a distortion

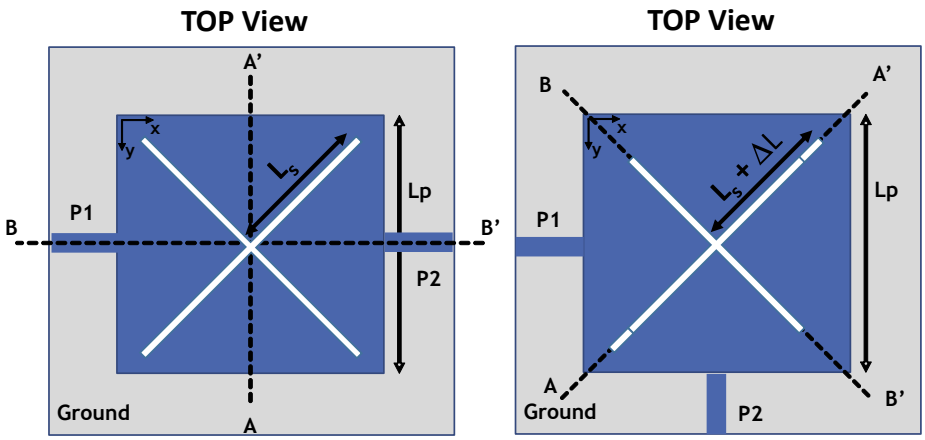

(a) (b)

Figure 2.17: Patch resonator with cross slots: (a) symmetrical with collinear feeding, (b) asymmetrical with orthogonal feeding.

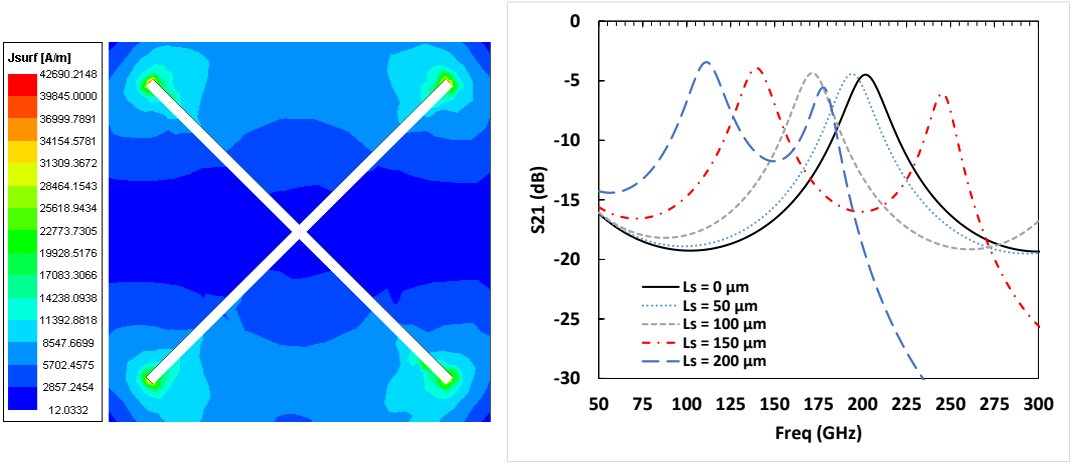

(a) (b)

Figure 2.18: Patch resonator with symmetric cross slots: (a) Surface current J of TM_{10} mode, (b) insertion loss S_{21} variation vs L_s.

of J and allowing a current flow from source P_1 to load P_2 rerouted around the slots. So the signal path is electrically extended and leads to drop off of the resonance frequency. This will reduce some radiation loss at the operating frequency. Interestingly, etches can be characterized as inductive loading, so it can be considered that a slow-wave occurs. With such a slow-wave technique, the frequency is shifted downward since the inductance and resonant frequency are inversely proportional. As the length of cross etches increases, the resonance frequency is shifted downward (Figure 2.18(b)). For variation of L_s from 0 to 200 µm, the resonance frequency shifts from 200 GHz down to 111 GHz. This leads to a an overall size reduction of the rectangular patch resonator with maximum miniaturization

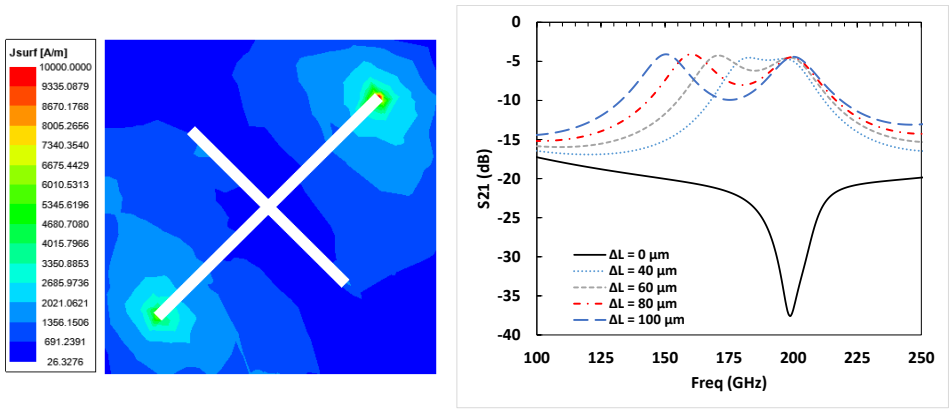

(a) (b)

Figure 2.19: Patch resonator with asymmetric cross slots: (a) Surface current *J* of Odd mode, (b) insertion loss S_{21} variation with ΔL.

of 69% calculated from (3.5).

This result is used to study the dual-mode behavior of the rectangular patch resonator by differentiating the length of the two diagonal slots and rearranging the external ports to excite both modes at the same time as shown in Figure 2.17 (b). The symmetrical cross slots of L_s = 100 μm is selected and accordingly the patch size L_p is minimized to 272 μm to keep the operating frequency at f_c = 200 GHz. Then, the slot across the *AA*' axis is extended by length ΔL in order to create coupling between the degenerated modes. As already mentioned, these modes are referred to be the *odd*- and *even*-modes, which are being controlled by the slots along *AA*' and *BB*', respectively. Figure 2.19(a) shows the surface current J flow of the *odd*-mode. Since its E field is defined along BB', as shown before in Figure 2.12 (b), its current is obliged to rout around the extended slot from the source to the load. So the electrical length $\theta_{odd} > \theta_{even}$ due to ΔL, then f_{odd} is split and shifted downward while f_{even} stays unchanged at 200 GHz. Figure 2.19 (b) shows the variation of the insertion loss S_{21} of the degenerated modes with different values of ΔL. When ΔL = 0 μm, no transmission occurs, which means there is great isolation between the two modes. But when ΔL is increased, S_{21} rapidly jumps to -4.5 dB and successively, the degenerated modes start to couple and split. For example, with ΔL = 100 μm, the f_{odd} reaches 150 GHz while f_{even} is unchanged at 200 GHz. This duality and controllability of the modes allows to design dual-mode patch filters with flexible responses.

2.2. Design Methodology for Dual-mode and Cascaded Patch Filters

It is pivotal to explain the design methodology that is followed in order to build up the intended filters, especially for mm-wave filter circuit design. Our interest is to present the synthesis methodology for narrowband dual-mode filters with grounded *via*s, which for our best knowledge was not recorded before. Moreover, a flow design chart is presented and thoroughly explained to bring an overview for any future filter design in integrated technology.

2.2.1. Dual-Mode Patch Filter Synthesis

Conventionally, filters based on patch cavity or microstrip topologies are synthesized through the general coupling scheme presented by Cameron in [86]. Each resonator has a single resonance mode with single resonance frequency, which is either coupled to the successive resonator or to the source/load, where source/load is only coupled to one resonator. This type of synthesis can produce $N-2$ frequency transmission zeros (FTZ) where N is the number of resonators. Thus, filters with low order $N < 3$, can suffer from bad rejection bands due to the limitation in producing any FTZ. Moreover, filters with single resonator that support dual-mode resonances cannot be synthesized using such approach.

Another optimized approach is the adaptive synthesis methodology that was presented in [87]. It is the evolution of Cameron's concept but obeys to source/load-multiresonator coupling. Its N^{th} order coupling scheme is presented in Figure 2.20. The source *S* and load *L* are denoted by "white" nodes, while the resonators are denoted by "black" nodes. Our discussion here is about modes so each node can be referred to a single mode in the patch cavity instead of resonators. The main coupling or direct path between nodes is denoted by solid line and indirect coupling or an admittance inverter is denoted by dotted line. Such approach allows multiple couplings between source/loads and resonators (M_{sn}/M_{Ln}), resonators to resonators ($M_{n,n+1}$) and between source and load (M_{sL}) itself. So, the generation of FTZ depends on the multi-path between the source and load. This coupling scheme can be also expressed by a coupling matrix *CM* with $N+2$ rows and $N+2$ columns as in (2.7), where N is the filter's order.

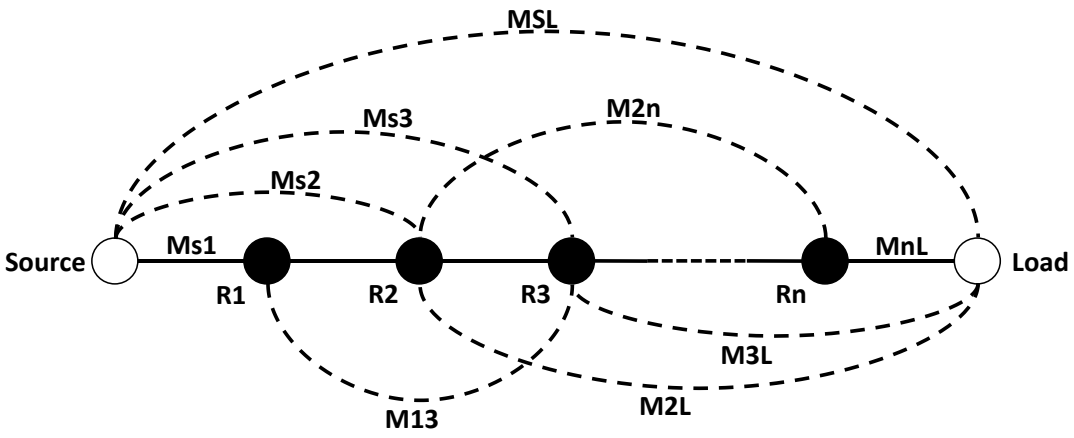

Figure 2.20: Routing and coupling scheme of n coupled resonators with source/load-multiresonator coupling. Solid line: direct coupling, dashed lines: bypass or indirect coupling.

$$M_{n^{th}Order} = \begin{bmatrix} M_{ss} & Ms1 & M_{s2} & M_{s3} & \cdots & M_{sn} & M_{sL} \\ M_{1s} & M_{11} & M_{12} & M_{13} & \cdots & M_{1n} & M_{1L} \\ M_{2s} & M_{21} & M_{22} & M_{23} & \cdots & M_{2n} & M_{2L} \\ M_{3s} & M_{31} & M_{32} & M_{33} & \cdots & M_{3n} & M_{3L} \\ \vdots & \vdots & \vdots & \vdots & \vdots & \vdots & \vdots \\ M_{ns} & M_{n1} & M_{n2} & M_{n3} & \cdots & M_{nn} & M_{nL} \\ M_{Ls} & M_{L1} & M_{L2} & M_{L3} & \cdots & M_{Ln} & M_{LL} \end{bmatrix} \tag{2.7}$$

The first row designated to the source, the second up to the $N+1$ designated to the first up to the N^{th} resonant mode, and the last row designated to the load. The matrix elements represent the normalized coupling coefficients between each part of the filter in the rows and columns, and are frequency-independent. The main diagonal has non-zero elements except for M_{SS} and M_{LL}, which are null terms with no meaning. The others represent the susceptance elements M_{11}, M_{22}, M_{33},…M_{nn} of modes "1", "2", "3", … "n", respectively. They are related to the offset of each self-resonance frequency (f_{01}, f_{02}, f_{03}, …f_{0n}) from the filter center frequency (f_c). M_{nn} and f_c are calculated from (2.8) and (2.9), respectively [77]:

$$M_{nn} = \frac{\frac{f_c}{f_{0n}} - \frac{f_{0n}}{f_c}}{FBW_{3dB}} \tag{2.8}$$

$$f_c = \left(\prod_{i=1}^{N} f_i\right)^{1/N} \tag{2.9}$$

where f_{0n} is the self-resonance frequency of a given mode and FBW_{3dB} is the 3-dB fractional bandwidth of the defined filter. The center frequency f_c is the geometric mean of all the resonant frequencies. By inspecting (2.8), it is deduced that if f_{0n} is less than f_c then M_{nn} is positive, and vice versa. The farther f_{0n} from f_c the bigger is M_{nn} coefficient. In regards to the coupling between two resonators m and n, the general coupling coefficient M_{mn} is extracted from (2.10):

$$M_{mn} = \pm\frac{1}{2}\left(\frac{f_{0m}}{f_{0n}}+\frac{f_{0n}}{f_{0m}}\right)\times\sqrt{\left(\frac{f_m^2-f_n^2}{f_m^2+f_n^2}\right)^2-\left(\frac{f_{0m}^2-f_{0n}^2}{f_{0m}^2+f_{0n}^2}\right)^2} \qquad (2.10)$$

where f_{0m} and f_{0n} are the self-resonant frequencies of modes m and n, and f_m and f_n are the resonant frequencies of modes m and n when coupled to each other. For a dual-mode patch resonator, both frequencies can be extracted from EM simulation. When the filter is simulated with weakly coupled feeding ports, f_m and f_n can be extracted, while f_{0m} and f_{0n} can be extracted using the method of placing magnetic wall or electric wall in the filter's axis of symmetry [60]. This will excite only the *even*-modes or *odd*-modes, respectively. Another important element is related to the coupling coefficients M_{sn} or M_{Ln} from (2.11) between the resonator n and the S/L:

$$M_{sn}^2 = \frac{1}{Q_{en}} \qquad (2.11)$$

which is linked to external quality factor Q_{en} of given mode. For *even*-mode, $M_{sn} = M_{Ln}$ but for odd mode $M_{sn} = -M_{Ln}$.

Synchronous and asynchronous tuning

According to the above general coupling matrix, two types of filters can be designed, i.e. synchronous and asynchronous tuning filters, respectively. The synchronous tuning filters are the conventional cascaded filters where the self-resonant frequencies $f_{0n} = f_{0m} = f_c$. Thus, the main diagonal M_{nn} is null and coupling coefficient M_{mn} is simplified to:

$$M_{mn} = \pm\sqrt{\left(\frac{f_m^2-f_n^2}{f_m^2+f_n^2}\right)^2} \qquad (2.12)$$

The asynchronous tuning filters are those with independent control of resonance frequencies, while self-resonant frequencies $f_{0n} \neq f_{0m}$. It has two scenarios: i) $M_{mn} = 0$, if $f_{0n} = f_n$ and $f_{0m} = f_m$, which indicates that each mode is controlled independently. ii) $M_{mn} \neq 0$, if $f_{0n} \neq f_n$ and $f_{0m} \neq f_m$. This means all the elements in the CM are not null.

Multi-mode patch filters are naturally asynchronous tuning networks because each mode resonates at a different frequency. So the simplified coupling matrix for a dual-mode patch filters with two independently controlled modes is summarized in (2.13):

$$M_{2^{nd}Order} = \begin{bmatrix} 0 & Ms1 & Ms2 & MsL \\ M1s & M11 & 0 & M1L \\ M2s & 0 & M22 & M2L \\ MLs & ML1 & ML2 & 0 \end{bmatrix} \tag{2.13}$$

$M_{12} = M_{21} = 0$. As for the FTZ with normalized frequency Ω that can be produced from the dual-mode filter with this scheme, it is provided as follows [77][88]:

$$\Omega = \frac{M_{11}M_{S1}^2 - M_{22}M_{S2}^2}{M_{S1}^2 - M_{S2}^2} \tag{2.14}$$

According to (2.14), if $M_{S1} < M_{S2}$ then Ω > 0, thus FTZ is located at upper stopband. Ideally, the reverse is true, if $M_{S1} > M_{S2}$ then Ω < 0, thus FTZ is located at the lower stopband.

The theoretical curves of the transmission coefficient S_{21} and the reflection coefficient S_{11} for the defined coupling matrix CM, are derived from the loop current equations that are expressed in matrix form and grouped in vector $[I]$, which is summarized in (2.15) [87].

$$[-jR + \omega' W + CM][I] = [A][I] = -j[e] \tag{2.15}$$

Where:

- j^2 = -1 and $[R]$ is a $(N + 2) \times (N + 2)$ matrix, in which only nonzero entries are $R_{11} = R_i$ and $R_{N+2,N+2} = R_o$, both normalized to 1 (the reference is 50 Ω).
- $[W]$ is a $(N + 2) \times (N + 2)$ identity matrix, with $W_{11} = W_{N+2,N+2} = 0$.
- ω' is the lowpass prototype normalized angular frequency given by (3.16):

$$\omega' = \frac{\omega_c}{\Delta\omega}\left(\frac{\omega}{\omega_c} - \frac{\omega_c}{\omega}\right) \tag{2.16}$$

where: ω_c is the center angular frequency of the filter and $\Delta\omega$ is the bandwidth of the filter.

- [CM] is the coupling matrix.
- $[e]$ is a $(1 \times N)$ vector that represents the filter stimulus, in which only nonzero entry is e_{11} = 1.

Then the scattering parameters curves are given by (2.17) and (2.18).

$$S_{21} = -2j[A^{-1}]_{N+2,1} \tag{2.17}$$

$$S_{11} = 1 + 2j[A^{-1}]_{11} \tag{2.18}$$

A Matlab code provided in APENDIX was used to plot the theoretical curves.

2.2.2. Integrated Filter Design Methodology

The design of mm-wave filters is not simple because the behavior of filters at higher frequencies above the sub-wavelength band has more constraints due to parasitics. Also, implementing passive circuits on integrated technologies has a lot of designing rules to be considered and in most cases, they introduce negative drawbacks. In this work a general overview of the proposed design methodology is presented, to be followed in order to successfully implement any future mm-wave filters. To further demonstrate the design approach for an integrated bandpass filter, a summary of thorough step-by-step design procedure is shown in Figure 2.21.

Step 1) Usually at this stage the filter characteristics (center frequency, FBW and rejection levels) are chosen according to the intended application. Moreover, the resonator topology should be chosen carefully in order to check its flexibility in responses to build up the filter. It is recommended at this stage to choose the stack from the BEOL of the selected technology, in order to determine the finite Q of the filter.

Step 2) The filter function (Chebyshev, quasi-elliptic, Butterworth…etc.) is chosen at this stage, including the finite FTZ that could be produced. The initial values of

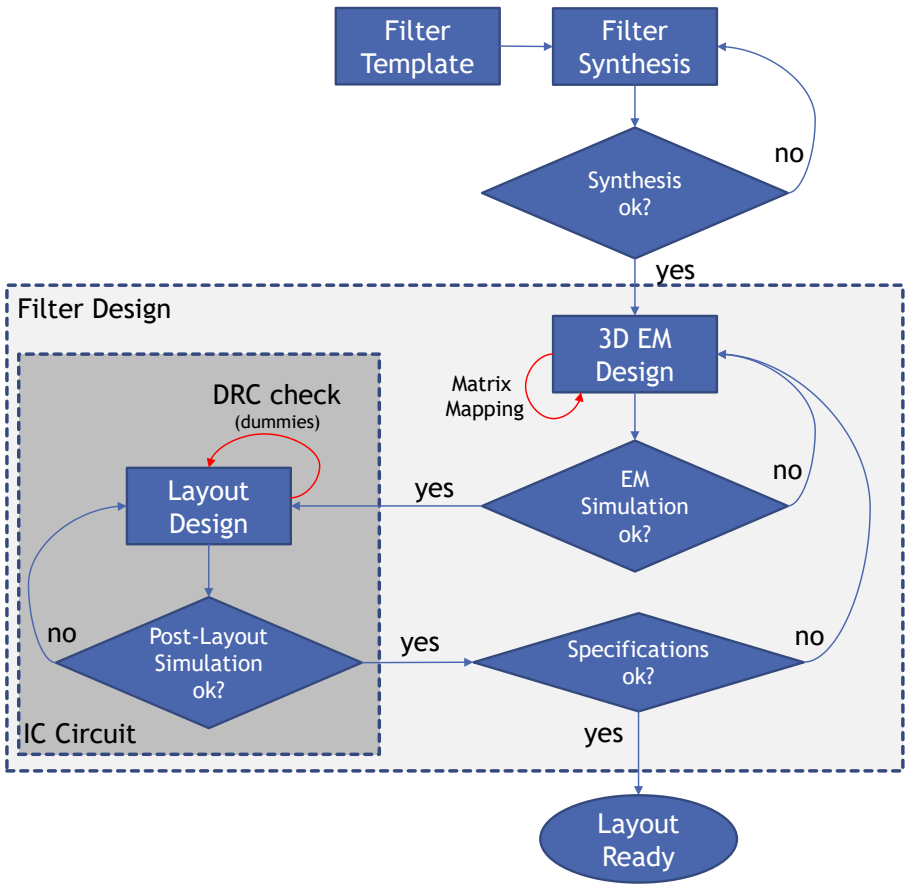

Figure 2.21: Integrated filter design flow chart.

the coupling matrix are extracted from the lowpass prototype parameters using (2.19) and (2.20):

$$Q_{ei} = \frac{g_i g_{i+1}}{FBW}$$
$$M_{s(L)i} = \frac{1}{Q_{ei} \times FBW} \qquad \text{for } i\text{=1 to } n \qquad (2.19)$$

$$M_{i,i+1} = \frac{1}{\sqrt{g_i g_{i+1}}} \quad \text{for } i = 1 \text{ to } n\text{-1} \qquad (2.20)$$

where n is the order of the filter, Q_{ei} is the external quality factor of a given node at the source or load, $M_{s(L)i}$ is the external quality factor corresponding to the normalized coupling coefficient at the source or load, and $M_{i,i+1}$ is the normalized coupling coefficient between the adjacent nodes. After that the optimization technique in [77] is used to achieve the intended filter response.

Step 3) After the lossless filter response is fixed, the physical dimensions are extracted from the mapping between the coupling matrix and the elements of the design. The EM simulation of the designed filter is conducted (using ANSYS HFSS software in the present work). Then a comparison between the simulated and theoretical results is conducted to make sure that we are still within the filter template specifications.

Step 4) This is a very important stage where the filter design is implemented within the integrated technology framework. All the design rules from the manufacturer's Design Rule Manual (DRM) must be taken into consideration at this step. It includes the minimum and maximum allowed physical dimensions for a strip line at the top metal. In addition to the minimum and maximum allowed metal density on each metallic layer from the BEOL, it is worth to mention that the design rules checker (DRC) may oblige to add metals in undesired zones, where it adds parasitics to the filter. So, modifications to the 3D design is required to compensate the added losses. After a successful post-layout simulation and DRC validation, the layout is ready for fabrication.

2.3. Conclusion

In this chapter a full and detailed description of the integrated patch filter design aspects was conducted. It is decomposed into two main parts: square patch design principles and filter synthesis methodology.

Patch resonators with integrated grounded *via*s allow a great reduction to the overall size, as thoroughly explained, which is an important feature for integrated passive circuits design. Also, an analysis to the effect of different perturbation techniques on the fundamental and higher order modes through exploring their resonance frequencies and fields' distribution, is discussed.

The second part focuses on the filter synthesis methodology, using the adaptive techniques through extracting the coupling matrix elements and with optimization technique, the intended filter can be designed. Dual-mode filters are considered as asynchronous tuned networks, where the resonance modes are independently controlled and different from the center frequency of the filter. Also, the cascaded filter topology is

considered as synchronous tuned networks where self-resonant frequency of all the resonators are equal to the center frequency of the filter. Finally, an integrated filter design flow chart, starting from the filter template and passing through 3D design and layout implementation, is presented.

CHAPTER III: MM-WAVE PATCH FILTER DESIGN

Designing a new and novel patch filter is still considered one of the big challenges, because the literature, as presented CHAPTER I, is very rich of ideas and techniques. It is true that our focus in this dissertation is to test bandpass filters based on patch resonators on BiCMOS integrated technology at mm-wave bands, but having a well fashioned design is a key measure. Based on this aim, this chapter thoroughly presents several bandpass filter designs with an original modified patch resonator. It is decomposed into two main parts: i) the first part presents the design and synthesis of dual-mode and dual-band patch filters that operate above 100 GHz and implemented on different stacks from BiCMOS 55nm technology. The duality is rebuild using a hybrid perturbation approach that combines both grounded *vias* and slots. ii) In the second part a 2nd order ultra-compact patch-like bandpass filters is developed. Original techniques like Complementary Split Ring Resonator (CSRR) and loading "mushrooms" are integrated along with grounded *vias* to provide a massive miniaturization to the conventional patch resonator.

3.1. Dual-Mode narrowband BandPass Filter above 100 GHz

3.1.1. Grounded Patch Filter with Collinear Feeding

Proposed Patch Resonator with Perturbation

Two techniques are selected from Table 1.1 in order to (i) reduce the dimensions of the square patch resonator, and (ii) flexibly control its modes, which are the grounded *vias* of size $viad$ and single vertical slot of length L_s, as shown in Figure 3.1 and Figure 3.2, respectively. This hybrid combination can improve the capability to control the modes and increase the miniaturization factor obtained by using only one way. The filter is built up by two steps: first the fundamental modes TM_{01} and TM_{10} are split using grounded *vias*, which perturb their E field. Afterwards, the vertical slot perturbs the surface current J of TM_{10} with full controllability of its resonance frequency. So, the duality is rebuilt again, but with $LC-mode$ and TM_{10}.

To further illustrate on the relationship and the manipulation between modes, perturbations in the resonator are carefully and separately analyzed. Figure 3.1 (a) shows the configuration of modified patch resonator with two grounded metallic *vias* at its top/bottom sides along *AA*' axis. Two *vias* are used instead of one, in order to increase the

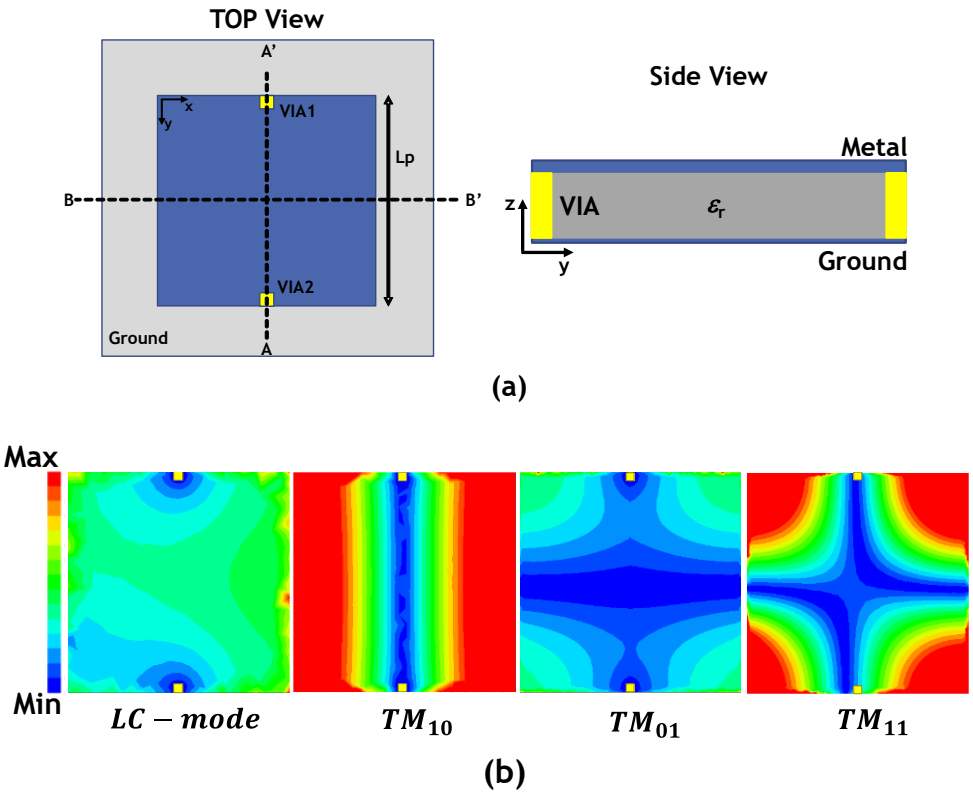

Figure 3.1: (a) configuration of perturbed patch by *via*. (b) Electric field distribution of first four resonance modes.

coupling between the fundamental modes, for upper band rejection improvement. The E field distribution of the first four modes ($LC-mode$, TM_{10}, TM_{01} and TM_{11}), derived from the *eigenmode* solution solver in ANSYS HFSS, is shown in Figure 3.1 (b). As discussed before, LC-mode has a uniform electric field along the surface area of the patch, except at both *vias* position, where the electric field is null. So, this mode is affected either by changing its $viad$ or patch L_p. Since *vias* are implemented at the middle of the patch edges, TM_{10} and TM_{11} modes are unaffected, while TM_{01} could be greatly perturbed because its electric field is maximum at the top and bottom edges (in the absence of *vias*) as shown in Figure 3.1 (b). Next, a vertical slot perturbation element is etched in the middle of the patch along *AA*' axis, to control TM_{10} and TM_{11} modes, as shown in Figure 3.2 (a). Mainly this slot is intended to control the TM_{10} mode, since its surface current J is maximum in the middle of the patch and flows orthogonally to the slot along *BB*' axis. The surface current J distribution of the first three *eigenmodes*: TM_{10}, TM_{01} and TM_{11}, is shown in Figure 3.2 (b). It is clear that TM_{01} mode is almost unchanged since the inserted

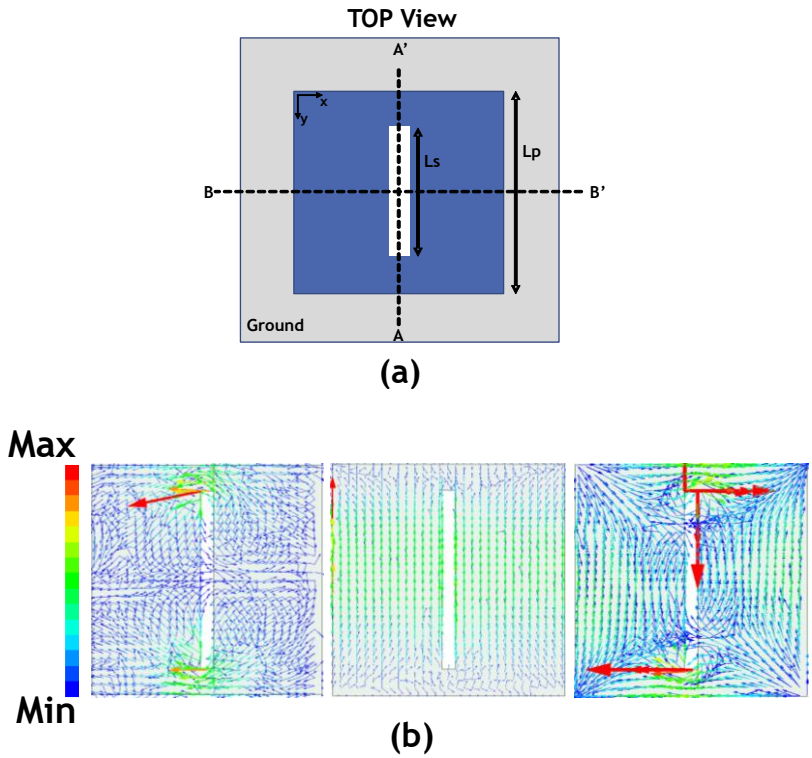

Figure 3.2: (a) configuration of perturbed patch by vertical slot. (b) Electric field distribution of the first three resonance modes.

vertical slot is in parallel with its surface current flow. While TM_{10} is drastically perturbed by the vertical slot since its surface current has to follow the path around the edges of the slot in order to pass from source to load (I/O feeding), and so its electrical length is increased accordingly. For TM_{11} mode, its surface current flows horizontally and vertically at the four edges of the patch only. When the vertical slot reaches the edges, the top and bottom current flow are affected and slightly perturbed.

In order to deeply analyze the effect of both perturbations on the resonance frequencies of each mode, Figure 3.3 shows the transmission response (S_{21}) of the four intended modes, which are simulated through two-ports structure weakly coupled to the patch resonator**.** The conventional square patch resonator without perturbation in Figure 2.1 is recalled, with L_p = 360 µm and central frequency f_c at 200 GHz. When there are no perturbations, fundamental modes (TM_{01} and TM_{10}) are still combined at the center frequency of the patch while TM_{11} appears at f_{11} = 285 GHz, as theoretically predicted. In case of single *via* perturbation, the new $f_{LC-mode}$ appears at 70 GHz, then it shifts to 100 GHz when two *vias* are inserted, because $f_{LC-mode}$ and $viad$ are proportional. TM_{10} and TM_{11} resonance

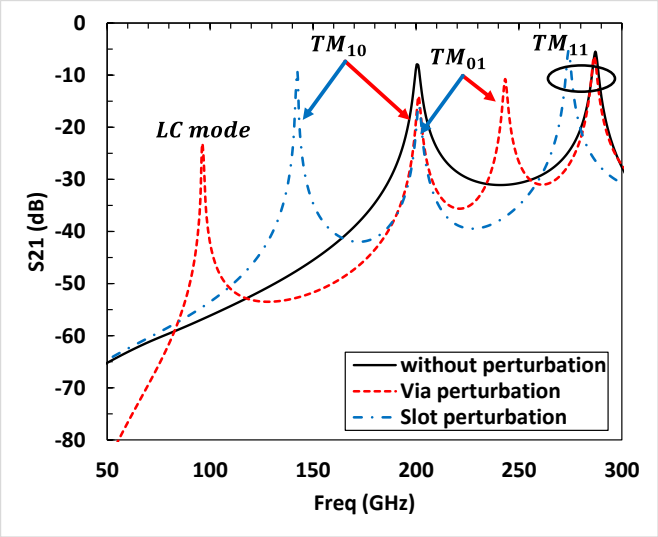

Figure 3.3: Transmission response S_{21} of patch resonator with and without perturbations.

frequencies are not changed, while TM_{01} resonance frequency is split and shifted upwards. It is more perturbed when two *vias* are inserted, where its f_{TM01} shifts from 220 GHz to 245 GHz. Lastly, when vertical slot is inserted, TM_{01} is unchanged as expected and still resonating at f_c, while TM_{10} and TM_{11} resonance frequencies are shifted downwards. This confirms the observation carried out in Figure 3.2 (b), e.g. the vertical slot has big impact on TM_{10} with TM_{11} slightly changed, since it perturbs part of its current.

Original Dual-Mode Square Patch Filter

Figure 3.4 shows the proposed configuration for the dual-mode square patch filter with its equivalent coupling scheme. The patch resonator is of length L_p and implemented on M8U:M1 stack from BiCMOS 55 nm technology of 8 ML version. The proposed design (Figure 3.4 (a)) combines both perturbations presented previously with two *vias* of size $viad$ are inserted along the *AA*' axis and vertical slot of length L_s and width W_s inserted in the middle of the patch. The designed filter is desired to have a narrow band dual-mode response with operating frequency f_c = 200 GHz, supported by LC-mode and TM_{10} modes. Its out-of-band rejection is controlled, through creating an indirect path from source to load supported by the higher order modes TM_{01} and TM_{11}. In order to efficiently control these modes, horizontal slots of length L_h and width W_h are inserted along the BB' axis. Consequently, the feeding input/output (I/O) ports are configured collinearly at 180°. The chosen I/O arrangement excites both modes (LC-mode and TM_{01}) simultaneously, because

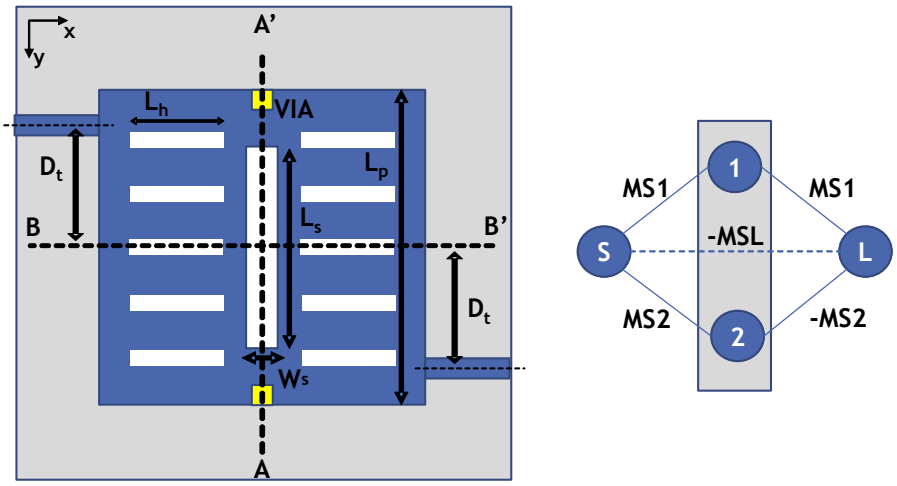

(a) (b)

Figure 3.4: (a) Layout of the dual-mode patch filter. (b) Equivalent doublet coupling scheme (SL: source/load, 1: TM_{10}, 2: LC-mode, solid line: main coupling, dotted line: S-L coupling).

their E fields are maximal at the edges. This means, the filter is symmetrical across AA' axis. I/O ports can be deviated from the center by distance D_t to realize different strengths of main coupling paths. This $\pm$ deviation breaks the filter's symmetry to create transmission zeros (FTZ) provided by higher order modes (TM_{01} and TM_{11}). In that case, asymmetric filter is developed.

Initially, a grounded square patch resonator of $L_p = \lambda/2 = 360$ µm is designed and simulated using ANSYS HFSS software with two integrated *vias* of initial size of $viad = 1$ µm. A lower resonance due to the $LC - mode$ appears at 100 GHz. Then, as a first step, the patch is shrinked to have $L_p = 200$ µm (69% of miniaturization), which in return shifts all its higher resonance frequencies including LC-mode upwards. Thanks to the compactness capabilities of *vias*, the first four resonance frequencies are: $f_{LC} = 155$ GHz, $f_{TM_{10}} = 356$ GHz, $f_{TM_{01}} = 410$ GHz and $f_{TM_{11}} = 503$ GHz, respectively. The effect of varying $viad$, L_s and L_h on the resonance frequencies is checked sequentially. Figure 3.5 shows the variation of the intended resonance frequencies versus $viad$. When $viad$ varies from 1 µm to 7 µm, f_{LC} is increased from 155 GHz up to 200 GHz. By increasing $viad$, the equivalent inductance of the via is decreased, thus explaining the increase of f_{LC}. As for $f_{TM_{10}}$ and $f_{TM_{11}}$, they are mostly constant, while $f_{TM_{01}}$ is shifted upwards from 410 to 446 GHz. So, as expected, $viad$ is only affecting f_{LC} and $f_{TM_{01}}$.Then, fixing $viad$ to 4 µm,

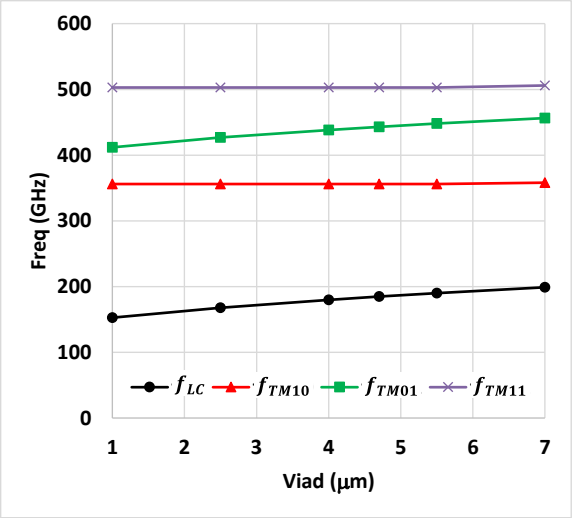

Figure 3.5: Resonance frequencies variation vs via diameter $viad$ (L_p = 200 μm).

in order to put f_{LC} near 200 GHz, vertical slot is inserted with variable length L_s.

Figure 3.6 (a) shows the variation of the intended resonance frequencies versus L_s, while slot width W_s is chosen in way to have enough slot gap to avoid electrical coupling. In this analysis it was fixed to 10 µm. f_{LC} and $f_{TM_{01}}$ are almost unchanged, a slight shift occurs only when L_s reaches the edges of the patch, while $f_{TM_{10}}$ is drastically decreased from 356 GHz to 212 GHz when L_s varies from 0 to 190 µm. Also, $f_{TM_{11}}$ is constant when L_s< 120 µm, and decreases to 465 GHz when L_s reaches 190 µm. So the vertical slot is mainly controlling $f_{TM_{10}}$, and when it reaches the edges, $f_{TM_{11}}$ is affected.

Figure 3.6 (b) shows the variation of the intended resonance frequencies when horizontal slots are inserted. The width of all horizontal slots was fixed to $W_s = 10$ µm. f_{LC} and $f_{TM_{10}}$ are constant and not affected by the variation of L_h, while both $f_{TM_{01}}$ and $f_{TM_{11}}$ are significantly decreased. When L_h is increased from 0 to 60 µm, $f_{TM_{01}}$ and $f_{TM_{11}}$ are decreased from 441 GHz and 465 GHz to 390 GHz and 412 GHz, respectively. Here it is good to mention that since horizontal slots are initially inserted at the edges of the patch, $f_{TM_{11}}$ is directly affected and decreases by the same manner of $f_{TM_{01}}$.

Based on the presented analysis, a dual-mode filter can be designed using the first resonance frequencies with an advantage of flexible responses, not only within the pass band but also within the out-of-band.

Extracted External Quality Factor and Source-Load Coupling

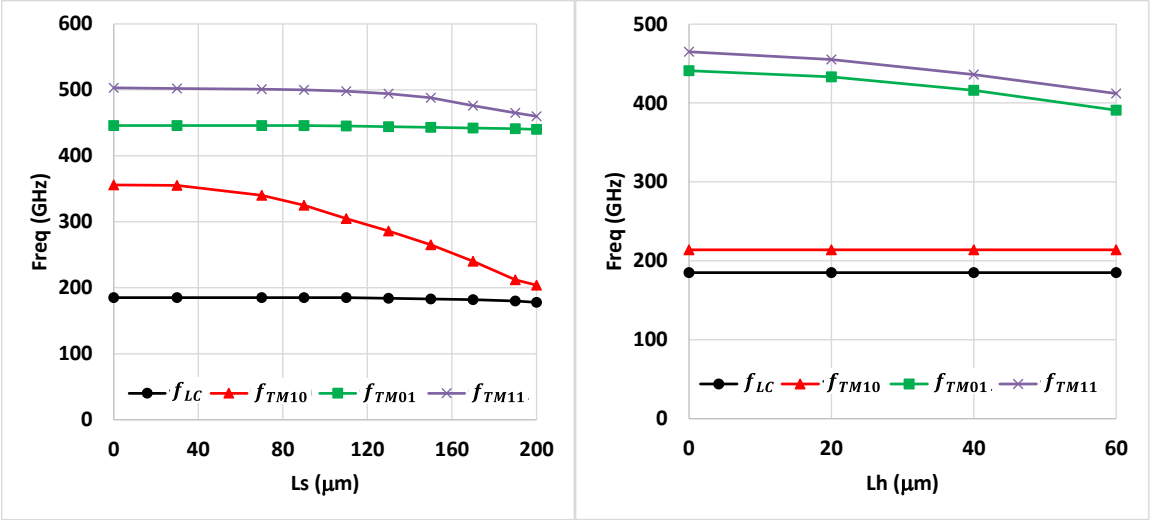

(a) (b)

Figure 3.6: Resonance frequencies variation vs: (a) vertical slot length L_s (L_p = 200 μm,$viad$ = 4 μm & W_s = 10 μm). (b) horizontal slots length L_h (L_p = 200 μm, $viad$ = 4 µm, L_s = 190 μm,W_s = 10 μm & W_h = 10 μm).

The previous variations study shows that there is a wide range of modes controllability for designing the dual-mode filter, if all modes are excited simultaneously. For this purpose, I/O ports are deviated by Dt from the center of symmetry to vary Q_e. Using the method presented in CHAPTER II, Q_e is extracted for LC-mode and TM_{10} mode and plotted in Figure 3.7 (a). When D_t = 0 µm, Q_{e-LC} and $Q_{e-TM_{10}}$ are almost equal, with $Q_{e-LC} =$ 13 and $Q_{e-TM_{10}} =$ 13.78. In this case the proposed structure is symmetrical, so the dual-mode filter can be realized with two poles, but without FTZs. When the absolute value of D_t increases, both modes are quietly increased, with more rapid variation for $Q_{e-TM_{10}}$, because they have almost uniform E field distribution at the left and right edges. Moreover, $Q_{e-TM_{10}}$ is always greater than Q_{e-LC}, i.e. source/LC-mode (M_{S2}) coupling is always greater than source/TM_{10} (M_{S2}) coupling, which means only one FTZ can be realized. This will be more elaborated further.

To verify this analysis, the transmission response (S_{21}) of the proposed dual-mode patch resonator is plotted in Figure 3.7 (b) for several D_t deviations. As discussed, when the feeding I/O ports are at the origin (D_t = 0 µm), the symmetry is not broken and no FTZ is observed. As D_t is increased to 40 µm, a single FTZ appears at the upper band of the patch, while the lower band rejection is almost unchanged. Therefore, FTZ is controlled to

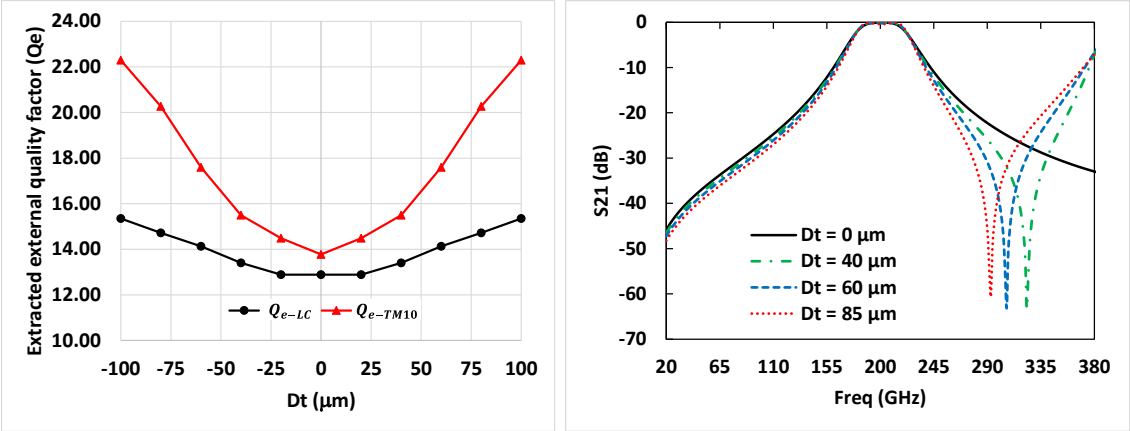

(a) (b)

Figure 3.7: Extracted Q_e factors for LC-mode and TM_{10}. (b) Transmission response S_{21} variation with Dt.

manage the upper band rejection, according to the filter specifications. Indeed, by putting the I/O ports near to the edges, higher order modes (TM_{01} and TM_{11}) are excited, which explains why the FTZ appears in the upper band. Then, Source/Load coupling is created and managed by the deviation D_t.

Filter Synthesis and Coupling Matrix

Based on the proposed architecture for modified patch resonator and the detailed discussion of the resonance modes behavior, a dual-mode bandpass filter can be designed as a doublet coupling scheme that is shown in Figure 3.4 (b). The two nodes "1" and "2" have a main coupling with source and load, while an indirect coupling between the source and load exists, only with asymmetrical ports feeding, as discussed before. The variations of resonance modes show that asynchronous filter can be designed since its main modes (LC-mode and TM_{10}) are independently controlled.

Conventionally for any dual-mode patch filter, *odd* ("1") and *even* ("2") -modes are naturally coupled. However, in this proposed modified patch, LC-mode and TM_{10} are uncoupled modes. Yet, based on the previously analyzed E fields, LC-mode can be referred to be the new *even*-mode since its E_z sign changes identically and simultaneously at the source and load, while TM_{10} is still considered as the *odd*-mode where its E_z has opposite signs at the source and load. So, the two different and initiated uncoupled modes are reconfigured to construct the filter. The synthesis methodology presented in CHAPTER II is used.

Recalling CM from (2.13), the main diagonal elements M_{11} and M_{22} refer to modes "1" (TM_{10}) and "2" (LC-mode). Since LC-mode exhibits always the lowest resonance frequency, then $f_{LC} < f_c$, so $M_{22} > 0$. As for TM_{10}, its $f_{TM10} > f_c$, then $M_{11} < 0$. Also, both modes are uncoupled, then $M_{12} = M_{21} = 0$. Moreover, $Q_{e-LC} < Q_{e-TM10}$, then $M_{s2} > M_{s1}$, therefore, according to (2.14), FTZ can be produced in the upper stop band. This is compatible with the variations in Figure 3.7 (b). In addition, $M_{s1} = -M_{1L}$ because TM_{10} has *odd* signs at the source and load, while $M_{s2} = M_{2L}$, because LC-mode has *even* signs at the source and load. M_{SL} is null when there is no coupling between the source and the load (case of asynchronous symmetrical filter) and it is ≠ from zero when there is coupling between the source and load (case of asynchronous asymmetrical filter).

From the presented theory for coupling matrix, and using the initial parameters in [27] for Chebyshev response, a 2nd order asynchronous symmetrical bandpass filter is designed, with center frequency $f_c = 200$ GHz, fractional bandwidth (FBW) of 20%, and return loss S_{11} of 20 dB. Its initial coupling matrix for infinite Q is:

$$M_{2^{nd}\,Order\,-SYMM} = \begin{bmatrix} 0 & 0.65 & 0.7 & 0 \\ 0.65 & -0.92 & 0 & -0.65 \\ 0.7 & 0 & 0.93 & 0.7 \\ 0 & -0.65 & 0.7 & 0 \end{bmatrix} \tag{3.1}$$

Since the desired filter should have flexible responses due to the modes independency, the initial coupling matrix is modified to:

$$M_{2^{nd}\,Order\,-SYMM} = \begin{bmatrix} 0 & 0.65 & 0.7 & 0 \\ 0.65 & -0.92 + y & 0 & -0.65 \\ 0.7 & 0 & 0.93 + x & 0.7 \\ 0 & -0.65 & 0.7 & 0 \end{bmatrix} \tag{3.2}$$

where coefficients M_{11} and M_{22} vary separately by factors x and y, respectively. The theoretical S_{21} and S_{11} responses with the variation of x and y, are plot in Figure 3.8. It is clearly shown that, when x or y vary separately, M_{11} and M_{22} are modified independently. In both cases, this variation modifies the center frequency and bandwidth. In order to map the achieved coupling matrix for symmetrical bandpass filter to the real dimensions of the patch filter, the optimization technique in [27] is used. Also, *EM* solver from ANSYS HFSS is utilized to extract the self-resonance frequencies of each mode, by weakly coupling the

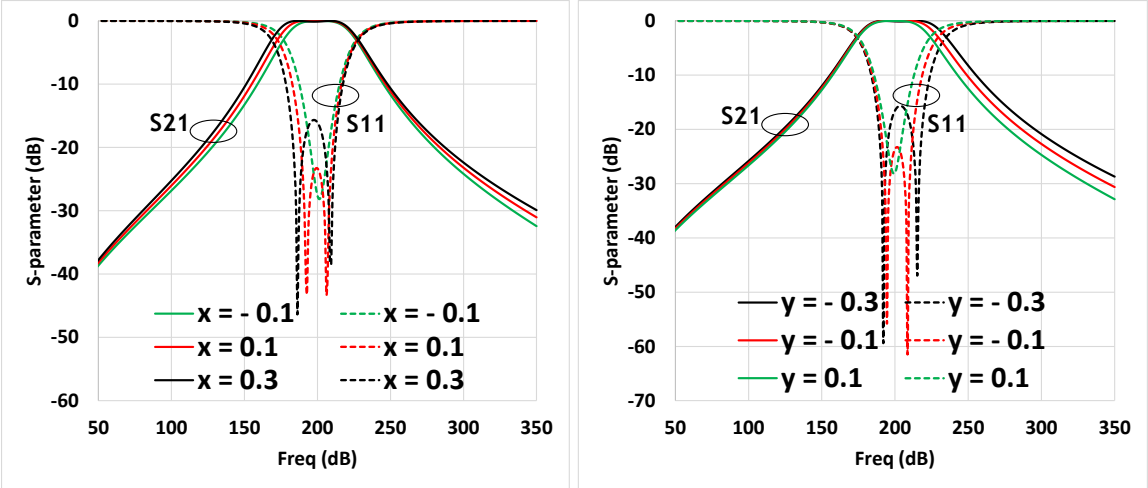

(a) (b)

Figure 3.8: Theoretical filter response with (a) variable M_{22} shifted by *x* and (b) variable M_{11} shifted by *y*.

patch resonator to the source and load, instead of using *electric* or *magnetic* walls technique. For LC-mode, it is fine-tuned by $viad$ size, while TM_{10} mode is fine-tuned by the length of the vertical slot L_S. Their values are extracted from the variations in Figure 3.5 and Figure 3.6 (a), and mapped to the elements of CM in (3.2). Moreover, for symmetrical filter no FTZ can be produced, then D_t is set to 0 µm. The *EM* simulation results with final patch elements dimensions, and theoretical results from the synthesized CM in (3.3) are shown in Figure 3.9 (a). The achieved responses show a great agreement between simulation for infinite Q and extracted CM.

$$M_{2^{nd}\,Order\,-SYMM} = \begin{bmatrix} 0 & 0.65 & 0.7 & 0 \\ 0.65 & -0.92 & 0 & -0.65 \\ 0.7 & 0 & 0.93 & 0.7 \\ 0 & -0.65 & 0.7 & 0 \end{bmatrix} \tag{3.3}$$

In order to improve the performance of the filter and add FTZ, the symmetry of the filter is broken thanks to the asymmetric capabilities of the 180° feeding ports configuration. The CM in (3.3) is modified to include the coupling coefficient M_{SL} and summarized in (3.4).

$$M_{2^{nd}\,Order\,-ASYMM} = \begin{bmatrix} 0 & 0.52 & 0.61 & -0.002 \\ 0.52 & -0.61 & 0 & -0.52 \\ 0.61 & 0 & 0.79 & 0.61 \\ -0.002 & -0.52 & 0.61 & 0 \end{bmatrix} \tag{3.4}$$

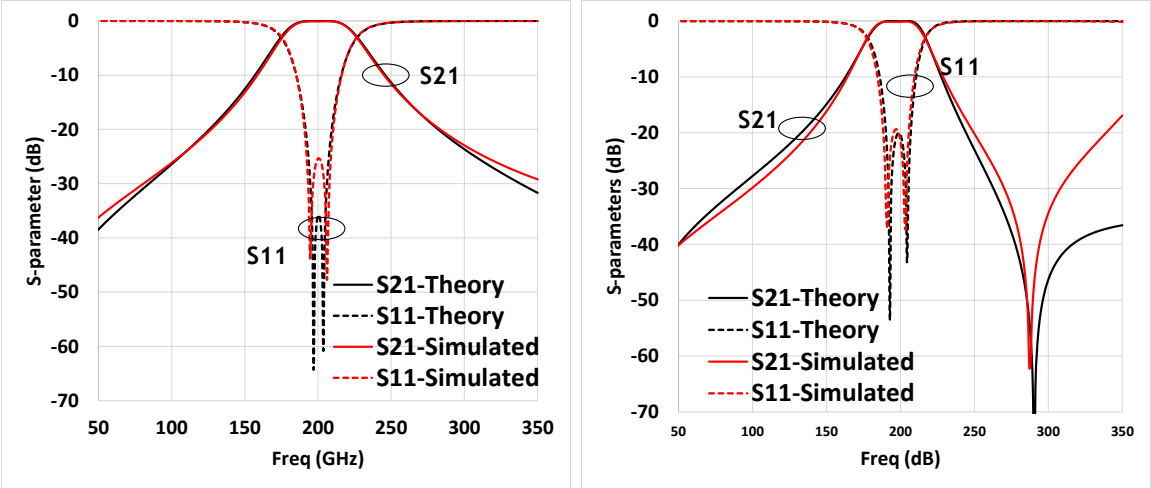

(a) (b)

Figure 3.9: Comparison between theoretical and simulated responses for: (a) symmetrical filter (L_p = 200 mm, L_s = 188 μm, W_s = 10 μm, L_h = 60 μm, W_h = 8 μm, D_t = 0 μm), and (b) asymmetrical filter (L_p = 200 mm, L_s = 188 μm, W_s = 14 μm, L_h = 60 μm, W_h = 8 μm, D_t = 96 μm).

This is mapped to the change of Q_e when feeding ports are deviated from the origin of the patch. It creates an indirect coupling between S/L supported by the excitation of higher-order modes. For the same defined filter template, the extracted CM for the desired asymmetrical filter with its theoretical S_{21} and S_{11} responses are compared to the achieved simulation results, with infinite Q, and plotted in Figure 3.9 (b). As expected, FTZ is added in the upper-band of the filter, which improves the upper selectivity and the out-of-band rejection.

Multiple Filter Designs

The variation of Q, as discussed in CHAPTER I, depends on the chosen stack of the BEOL. The presented results in the synthesis do not take into consideration the losses occurred within the BEOL layers. In order to consider finite Q, the metallic layers are chosen to have copper conductivity of $\sigma_c = 5.1 \cdot 10^7$ s/m. The achieved results for the asymmetrical dual-mode filter are plotted in Figure 3.10 for the same optimized dimensions. The recorded insertion loss is S_{21} = -2.5 dB at the center frequency of 200 GHz. The filter is well matched with a return loss equal to 20 dB and a FBW 20%. These results are very promising especially at this high frequency which was not targeted before, to our best knowledge. Moreover, the proposed filter has flexible responses where

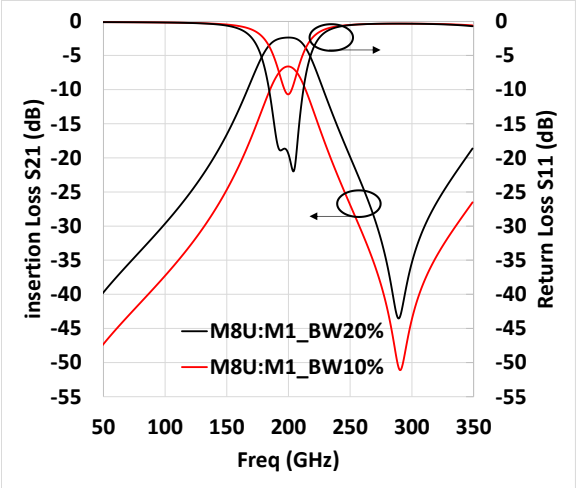

Figure 3.10: Asymmetrical dual-mode BPF simulated responses with finite *Q* for 20% and 10 % of FBW.

10 % of FBW is possible by changing the self-resonance frequencies of LC-mode and TM_{10} mode. However, after optimization ($viad$ = 6.3 µm and W_s = 22 µm), an insertion loss around 7 dB is occurred for the 10% FBW. In order to improve the performance and compensate the added losses, the B55-9ML version is chosen to check its potentiality with the same filter topology.

The proposed patch resonator is implemented on M9v:M6z stack, where Q_u is 50 for a single patch resonator, which is two times better as compared to M8U:M1 stack (Q_u = 22). At the very beginning the patch wasn't well matched, so we added shorted stubs of length L_{stub} = 100 µm and width W_{stub} = 10 µm at the input and output ports as shown in Figure 3.11 (a). An optimization for the patch resonator elements is required to adjust the responses with L_p = 190 µm, $viad$ = 6.3 µm and L_s = 24 µm. The achieved simulated results are plotted in Figure 3.11 (b). The recorded S_{21} is really impressive, with maximum insertion loss of 3 dB at center frequency of 200 GHz with great return loss better than 20 dB for narrow FBW of 10%. A big compensation of losses around 4 dB from M8U:M1 stack is achieved, due to the improvement of Q_u provided by the B55-9ML using the M9v:M6z stack.

The presented synthesis methodology verifies the *EM* simulations and the drawn objectives for the proposed patch filter. Based on this, a total of seven patch filters were designed and implemented on B55-8ML, as described here below.

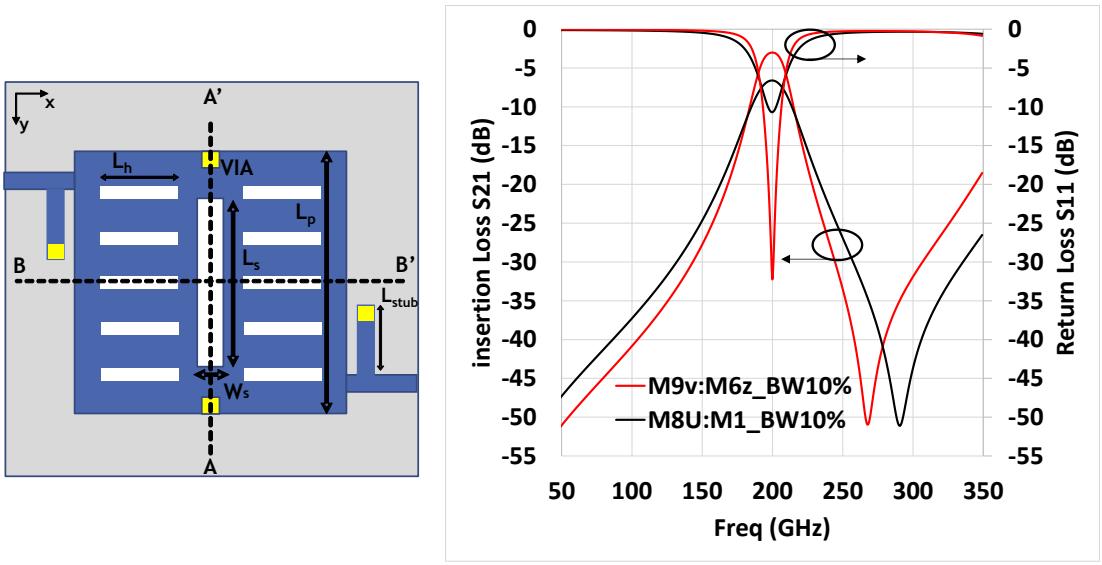

(a) (b)

Figure 3.11: Proposed BPF: (a) configuration at M9v:M6z stack, (b) simulated responses with finite *Q*.

1) Two patch filters with single order serve as a reference and are denoted by F-Ref1 and F-Ref2. These filters are conventional patch resonators operating at 200 GHz, without any perturbation (*via* or slot). They have large dimensions of 0.36 µm*0.36 µm (0.13 mm^2), but allow an estimation of the quality factor for two combinations of metals: M8U: M1 (patch on M8U and ground on M1) for F-Ref1 and AP:M6z for F-Ref2. Conventional patch resonators operating at 120 GHz have not been produced due to their dimensions, which would involve a high silicon cost.
2) Two dual-mode patch filters denoted by F-1 and F-2 operating at 120 GHz have been made on a stack M8U:M1, with symmetrical feeding version and asymmetrical feeding version, respectively.
3) In the same way, two similar dual-mode patch filters operating at 200 GHz were made on the same stack M8U: M1 with symmetrical and asymmetrical versions denoted by F-3 and F-4, respectively. Also, a dual-mode patch filter operating at 200 GHz was realized on AP:M6z stack and denoted by F-5.

In addition to those filters and to improve Q_u, two filters were designed and implemented on B55-9ML with the configuration as in Figure 3.11.

1) A conventional patch filter with single response at 200 GHz, implemented on M9v:M6z stack and denoted by F-Ref3.
2) A dual-mode filter operating at 200 GHz with FBW of 10 %, implemented on M9v:M6z stack and denoted by F-6.

All of these configurations allow, (i) to compare the dimensions and performance of the filters at two different frequencies, (ii) to compare the symmetrical and asymmetrical feeding versions, and finally (iii) to compare M8U:M1 stack with an AP:M6z stack from B55-8ML versions and M9v:M6z from B55-9ML version. All possible configurations were not realized due to technology costs. These filters were synthesized to have return loss of 20 dB and FBW of 20 %. Since the presented synthesis doesn't consider the occurrence of losses (infinite Q), the analysis for the expected losses after the layouts is made in CHAPTER IV along with filter layout and measurement results.

3.1.2. Dual-Band Grounded Patch Filter with Collinear Feeding

The dual-mode filter presented previously shows that it has flexible responses if the self-resonance frequencies of the first four modes are carefully controlled and managed. It could have dual-band dual-mode response with single patch resonator, thanks to multi-resonance modes with grounded *vias*. The proposed patch filter in Figure 3.4 (a) was modified to have both dual-mode asymmetric response and dual-band response as shown in Figure 3.12. The originality of this modified version allows to have multiple response with small modification. In Figure 3.12 (a) a dual-mode asymmetric bandpass filter is designed with two grounded *vias* aligned horizontally at the edges along the *BB*' axis, along with couple horizontal slots. This approach turns into dual-band filter response, as in Figure 3.12 (b), if vertical slot is inserted in the middle of the patch along *AA*' axis. Both filters are fed by collinear two-ports with 180° configuration.

Perturbed Square Patch Resonator

In order to explain the effect of *vias* orientation on the perturbed resonance modes, Figure 3.13 shows the E field and surface current *J* distribution of the first four resonance frequencies, LC-mode, TM_{01}, TM_{10} and TM_{11}, respectively. This time, only TM_{10} is affected by *vias*, since they shorten part of its E field to the ground, while TM_{01} and TM_{11}

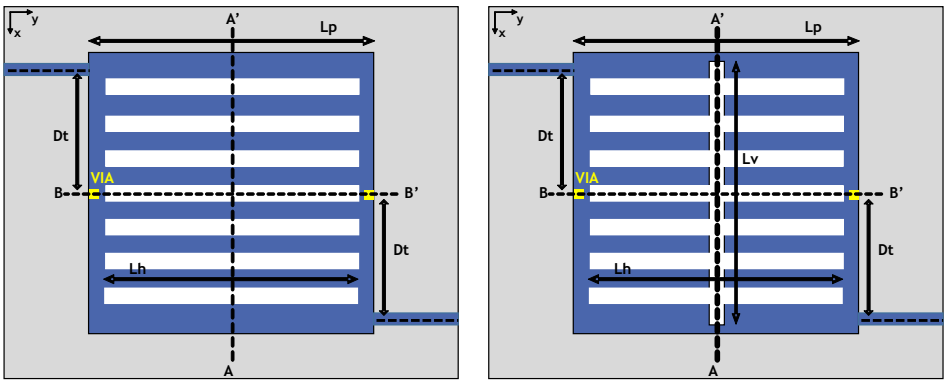

Figure 3.12: (a) proposed dual-mode filter, (b) proposed dual-band dual-mode filter.

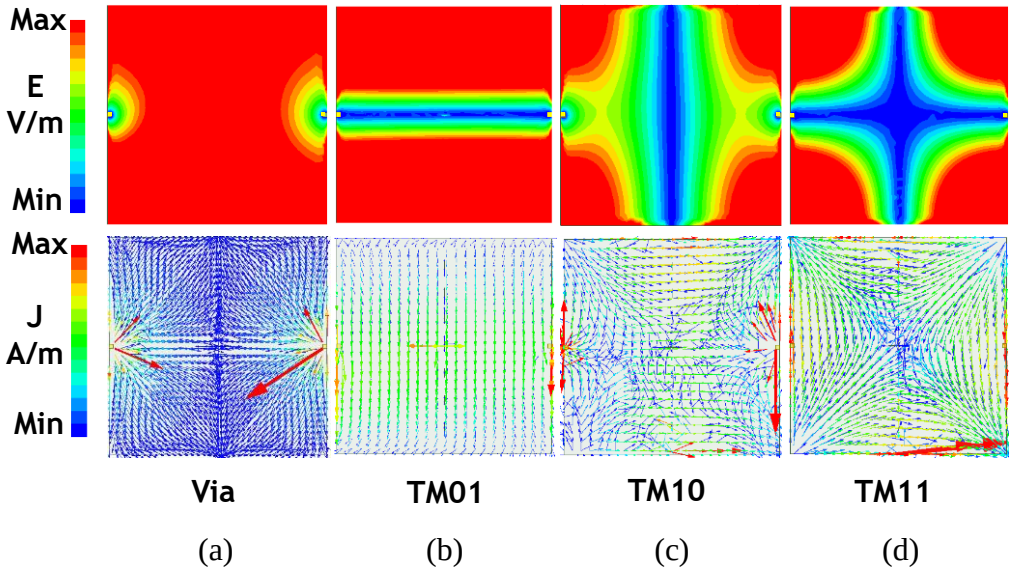

Figure 3.13: Electric field *E* and surface current *J* distribution of first four resonance modes of modified patch resonator with grounded vias.

modes are not affected because they have null E field at the position of the *vias*. Moreover, when observing the J current distribution, multiple horizontal slots would efficiently perturb TM_{01} mode, since its current flows vertically along *AA*' axis, with significant impact on TM_{11} mode especially when slots reach the edges. TM_{10} mode is significantly perturbed by vertical slot, as discussed in previous proposed filter. Our goal here is to gain more controllability on modes to build up the modifiable dual-band filter. So, the first two resonance modes (LC-mode and TM_{01}) are used to build the lower single-band asymmetric dual-mode filter. Then it is be combined with the other two resonance modes (TM_{10} and TM_{11}) to build the dual-band dual-mode bandpass filter.

Single-Band Dual-Mode Patch Filter

The proposed single-band dual-mode patch filter in Figure 3.12 (a) is designed using the same synthesis methodology presented in section 3.1.1. It is equivalent to the doublet scheme shown in Figure 3.4 (b) with node "1" representing the *odd*-mode TM_{01} and node "2' representing the *even*-mode LC-mode.

Following the same steps, Q_e of both modes are extracted from (2.6) and its variation is plotted in Figure 3.14 against the ports' deviation D_t. As previously explained, Q_{e-LC} is always less than Q_{e-TM01}, then $M_{s2} > M_{s1}$, so according to (2.14), one FTZ exists at the upper band rejection. Furthermore, the variation of Q_e for both modes is changing in a wide interval with values for TM_{01} ranging between 50 to 15, with D_t variation between 40 µm 100 µm. In comparison to the previous extracted Q_e in Figure 3.7, the difference can be explained by observing the E field in Figure 3.13, where both modes (LC-mode and TM_{01}) have non uniform E field distribution along the axis of D_t variation. For example, with D_t = 40 µm, the feeding ports are partially (low E magnitude) exciting TM_{01} mode, which increases Q_e. Nevertheless, it has good impact on adjusting the matching of the filter, where it is recommended according to this analysis, to place the excitation ports near the edges.

For demonstration, square patch resonator with two grounded *vias* of initial diameter size $viad$ = 1 µm, is designed and implemented on M8U:M1 stack using ANSYS HFSS software. Its initial side length is L_p = λ/2 = 360 µm. Since its first resonance frequency f_{LC} appears at 100 GHz, the modified patch's size is shrunk by approximately 69% to have

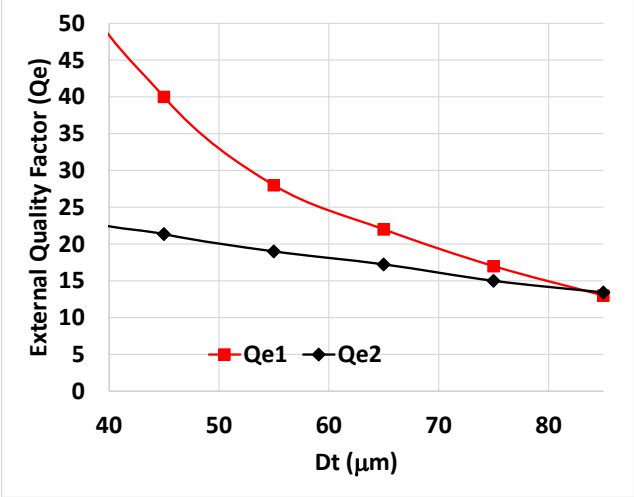

Figure 3.14: Extracted external quality factors for TM_{01} mode and LC-mode.

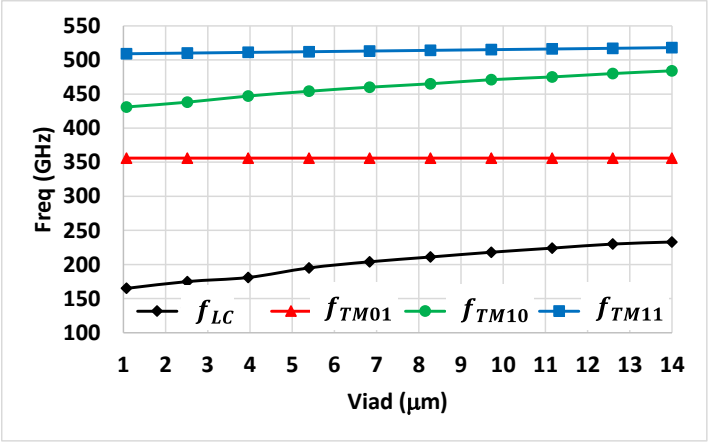

Figure 3.15: Resonance frequencies variation using via diameter (viad).

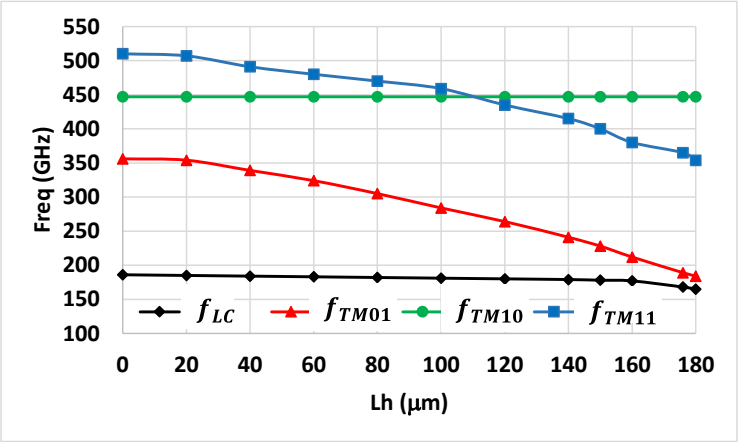

Figure 3.16: Resonance frequencies variation using horizontal slot length L_h (viad = 3.96 μm).

$L_p \approx \lambda/4$ = 200 µm. The first four resonance frequencies are: f_{LC} = 165 GHz, $f_{TM_{01}}$ = 356 GHz, $f_{TM_{10}}$ = 431 GHz and $f_{TM_{11}}$ = 509 GHz, respectively. At this stage the interest is in controlling the frequencies of LC-mode and TM_{01} mode only. LC-mode is adjusted by varying $viad$, which modifies the inductance of both *vias*, as shown in Figure 3.15. When $viad$ varies from 1 µm to 14 µm, f_{LC} increases linearly from 165 GHz to 233 GHz. Also, $f_{TM_{10}}$ increases from 431 GHz to 484 GHz. So, f_{LC} and $f_{TM_{10}}$ are directly affected by via size, while $f_{TM_{01}}$ and $f_{TM_{11}}$ are unchanged.

TM_{01} mode is mainly controlled by the length L_h and width W_h of the horizontal slots. W_h is fixed to 10 µm, and its impact is the same as L_h. The maximum number of slots is used, in order to increase the capability of controlling TM_{01} mode, which helps in fine tuning the filter. Figure 3.16 shows the effect of varying L_h on the resonance frequencies

while fixing $viad$ to 3.96 μm. It is clear that $f_{TM_{01}}$ and $f_{TM_{11}}$ are drastically decreased by the insertion of the horizontal slots. $f_{TM_{01}}$ decreases from 356 GHz to 184 GHz while $f_{TM_{11}}$ decreases from 510 GHz to 354 GHz when L_h increases from 0 to 180 µm. f_{LC} is smoothly unchanged, until the slots are near to the edges (thus perturbing the current around the *vias*). So, when L_h is greater than 160 µm, f_{LC} barely decreases from 182 GHz to 165 GHz. $f_{TM_{11}}$ is unchanged because the horizontal slots are in parallel to its current distribution.

The proposed single-band dual-mode square patch filter is synthesized to operate at center frequency of 180 GHz, with FBW of 15% and return loss of 20 dB. Its extracted asynchronous CM after optimization is summarized in (3.5).

$$M_{single\ -band} = \begin{bmatrix} 0 & 0.54 & 0.63 & -0.002 \\ 0.54 & -0.75 & 0 & -0.54 \\ 0.63 & 0 & 0.68 & 0.63 \\ -0.002 & -0.54 & 0.63 & 0 \end{bmatrix} \tag{3.5}$$

For comparison and verification, the synthesized responses based on the coupling scheme and its mapped simulated responses of the proposed layout configuration, are shown in Figure 3.17. The achieved result shows great agreement between theoretical responses from extracted CM and simulated results, for infinite quality factor. A single FTZ appears at 265 GHz in the upper band rejection. The only specification imposed during the design

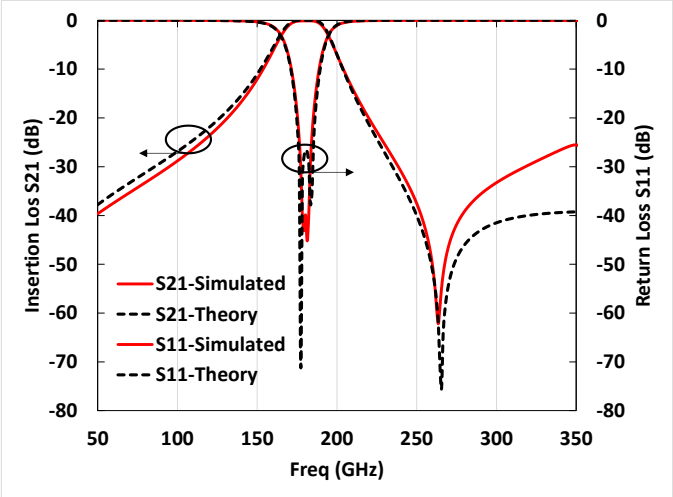

Figure 3.17: Comparison between theoretical and simulated responses for single-band dual-mode BPF *(L_p* = 200 μm, L_h = 176 μm, W_h = 8 μm, and D_t = 85 μm).

concerning the operating frequency, between 170 GHz and 180 GHz, and the fractional bandwidth, between 15% and 20%, is that a very reduced bandwidth would lead to unacceptable insertion loss, given the quality factor of patch resonators when considering the 8ML BEOL of the B55 technology, even if this quality factor is higher than that of transmission lines made with the same technology.

Dual-Band Dual-Mode Patch Filter

The dual-band filter is made on the same principle as the single-band filter just described, with the addition of a second band using the upper resonance modes TM_{10} and TM_{11}. According to the surface current J distribution in Figure 3.13, TM_{10} has a horizontal current flow along *BB'* axis, so vertical slot of length L_v and width W_v is added to reduce its resonance frequency, as presented in Figure 3.12 (b).

The effect of varying the vertical slot on LC-mode, TM_{01}, TM_{10} and TM_{11} modes is shown in Figure 3.18. It is clear that L_v has no impact on f_{LC} and f_{TM01}. When L_v increases from 0 to 188 µm, f_{TM10} steeply decreases from 445 GHz to 263 GHz. This "steep" behavior can be explained because, for each variation interval, vertical slot forms a closed loop with couple of horizontal slots. So, the current has to flow around the slots to reach the output. Next, f_{TM11} is affected when L_v is greater than 100 µm. It decreases from 343 GHz to 292 GHz, since the slot reached the edges. Hence, it is clear that vertical slot mainly controls the upper band.

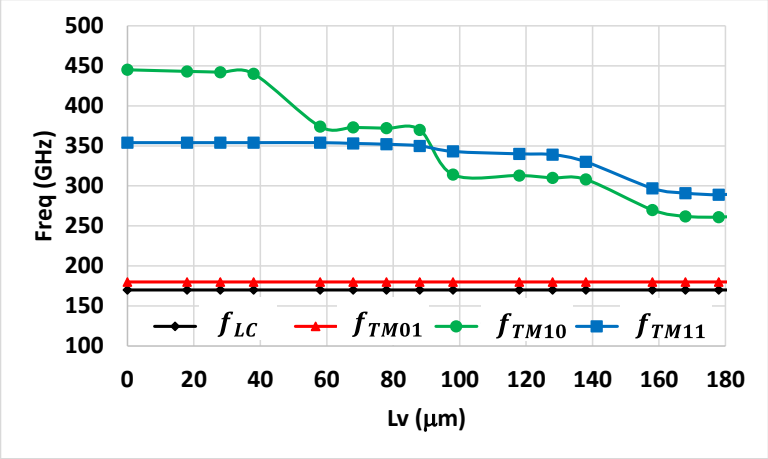

Figure 3.18: Resonance frequencies variation using vertical slot length L_v ($viad$ = 3.96 μm, L_h = 177 μm and W_v = 8 μm).

Table 3.1: Basic design guide of variable elements effect

Design Element	LC-mode	TM_{01}	TM_{10}	TM_{11}
Via	x	-	x	-
Horizontal slot	x	x	-	x
Vertical slot	-	-	x	x

In order to summarize the effect of each element in the proposed layout, Table 3.1 provides a basic design guide for the dual-band dual-mode filter response, i.e. x: significant impact, x: limited impact and -: no impact. Therefore, the presented variations show that the second band can still be modeled as the doublet coupling scheme in Figure 3.4 (b).

So, following the same synthesis methodology presented previously, a dual-band filter of center frequencies f_{c1} = 180 GHz and f_{c2} = 270 GHz, fractional bandwidths FBW_1 = FBW_2 = 15 % and RL = 20 dB is designed. The synthesized coupling matrices of 1st band and 2nd band are shown in (3.6) and (3.7), respectively.

$$M_{band\ 1} = \begin{bmatrix} 0 & 0.46 & 0.6 & -0.002 \\ 0.46 & -0.61 & 0 & -0.46 \\ 0.6 & 0 & 0.61 & 0.6 \\ -0.002 & -0.46 & 0.6 & 0 \end{bmatrix} \tag{3.6}$$

$$M_{band\ 2} = \begin{bmatrix} 0 & 0.6 & 0.61 & -0.07 \\ 0.6 & -0.75 & 0 & -0.6 \\ 0.61 & 0 & 0.92 & 0.61 \\ -0.07 & -0.6 & 0.61 & 0 \end{bmatrix} \tag{3.7}$$

The final dimensions of the dual-band patch filter is: L_p = 200 µm, $viad$ = 3.96 µm, L_h = 176 µm, W_h = 8 µm, L_v = 170 µm, W_v = 24 µm and D_t = 85 µm. Its extracted responses along with the simulated responses of the proposed layout configuration are shown in Figure 3.19. The achieved results show a great agreement between the simulation and extracted coupling matrix, for infinite Q.

In order to consider finite Q, the metallic layers are chosen to have copper conductivity. The achieved results for dual-band dual-mode filter is plotted in Figure 3.20. The recorded insertion loss (given by S_{21}) is equal to 2.6 dB for both bands. The filter is well matched with return loss (given by S_{11}) equal to 15 dB and FBW_1 = FBW_2 = 15%. It couldn't be possible with same configuration and same stack to achieve a lower FBW with acceptable

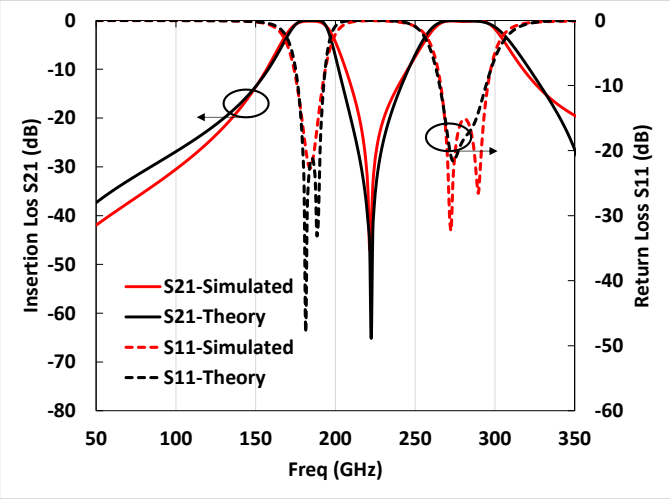

Figure 3.19: Comparison between theoretical and simulated responses for dual-band dual-mode BPF (L_p = 200 μm, L_h = 176 μm, W_h = 8 μm, L_v = 170 μm, W_s = 16 μm,and D_t = 85 μm).

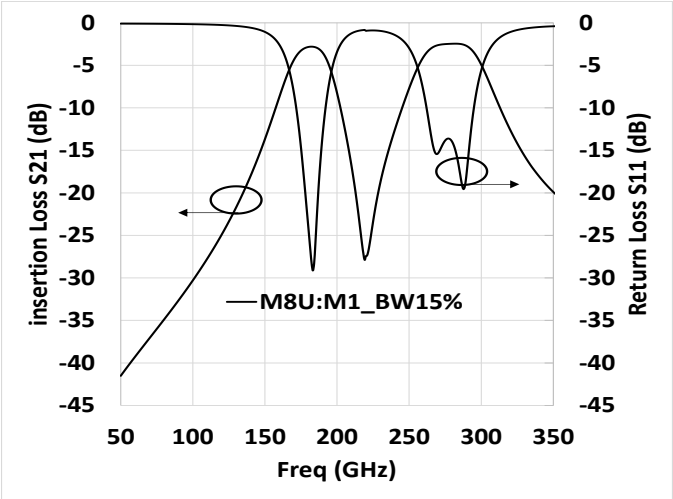

Figure 3.20: Dual-band dual-mode BPF simulated responses with finite Q for 15% of FBW.

s-parameters. So, to improve the performance, the B55-9ML version is chosen to check its potentiality with the same filter topology. As in previous design, the patch wasn't well matched, hence we added shorted stubs of length L_{stub} = 100 µm and width W_{stub} = 10 µm at the input and output ports as shown in Figure 3.21 (a). An optimization for the patch resonator elements is required to adjust the responses with L_p = 190 µm, $viad$ = 6.3 µm and L_s = 24 µm. The achieved results are plotted in Figure 3.21 (b). The recorded S_{21} is -2.8 dB and -2.5 dB at fc_1 = 185 GHz and fc_2 = 280 GHz, respectively. A great return loss better than 20 dB and narrow FBW of 10%. The compensation of losses is due to the improvement in the Q_u provided by the B55-9ML Usage of the M9v:M6z stack.

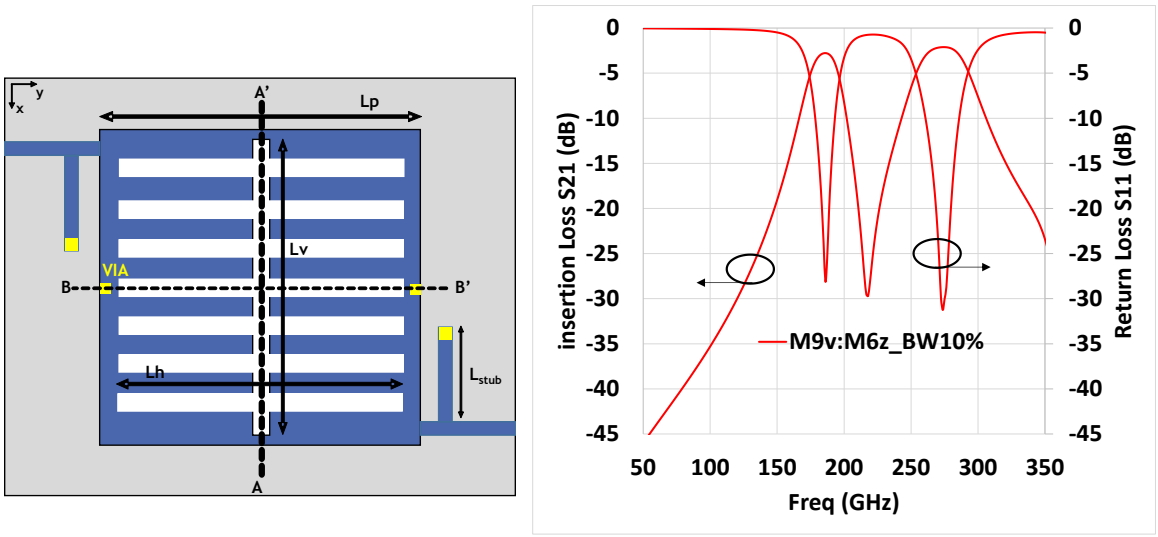

(a) (b)

Figure 3.21: Proposed dual-band BPF: (a) configuration at M9v:M6z stack, (b) simulated responses with finite Q.

The presented synthesis methodology verifies the *EM* simulations and the drawn objectives for the proposed single-band and dual-band patch filter. Based on this, a total of two filters were designed and implemented on B55-8ML, as described below.

1) A single-band dual-mode bandpass filter operating at 180 GHz and dual-band dual-mode bandpass filter operating at 180 GHz and 270 GHz, were developed on the same stack M8U:M1 denoted by F-7 and F-8, respectively. These filters were synthesized to have return loss of 20 dB and FBW of 15 %.

In addition to those filters and to improve Q_u, two filters were designed and implemented on B55-9ML.

2) A single-band dual-mode bandpass filter operating at 180 GHz and dual-band dual-mode bandpass filter operating at 180 GHz and 270 GHz, were developed on the same stack M9v:M6z denoted by F-9 and F-10, respectively. These filters were synthesized to have return loss of 20 dB and *FBW* of 10 %.

All of these configurations allow, (i) to analyze the performance of the filters at high frequencies, and (ii) to compare M8:M2 stack from B55-8ML version and M9v:M6z from B55-9ML version. Since the presented synthesis doesn't consider the occurrence of losses

(infinite Q), the analysis for the expected losses is made in CHAPTER IV along with filter layout design and measurement results.

3.1.3. Selective Grounded Patch Filter with Orthogonal Feeding

Taking the advantage of hybrid perturbations (grounded *vias* and slots) approach that is just presented with dual-mode filters, and combining it with orthogonal port feedings instead of collinear configuration, a new and original dual-mode bandpass filter design operating at 120 GHz is developed. The new approach improves the selectivity of the filter by creating multiple of transmission zeros at the out-of-band rejection along with better in-band filter responses. Also, because we aim in this dissertation to check the potentiality of the BiCMOS 55 nm technology with patch filters at mm-wave, another stack (AP:M6z) from B55-8ML version is used for demonstration.

Patch Resonator with Perturbations

The grounded *vias* are integrated this time at the TOP/RIGHT edges of the patch resonator as shown in Figure 3.22 (a), in order to perturb both modes simultaneously modified patch is excited by orthogonal ports feeding with Dt deviation from its center of origin. This configuration, flexibly, allows full excitation of several higher order modes. In this case, the axis of symmetry is rotated by 45° and aligned diagonally at *AA*' axis due to the boundary conditions created by the inserted *vias*. Our talk about the orientation of axis of symmetry and ports configuration is very important to determine the splitting technique for fundamental modes and creation of FTZs by upper modes. Without addition of any other perturbation like slots (as in Figure 3.22 (a)), TM_{10} and TM_{01} are still combined and uncoupled, because the symmetry between both modes is unbroken. However, a grounded

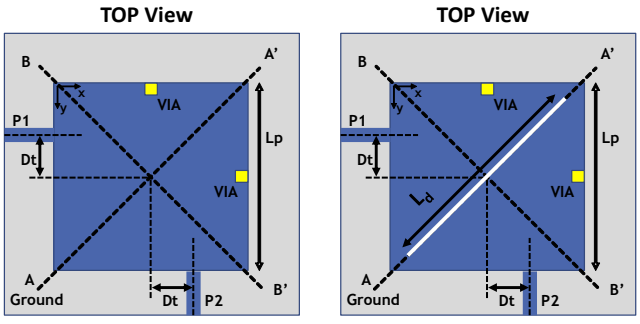

(a) (b)

Figure 3.22: Proposed grounded patch resonator with TOP/RIGHT *vias*: (a) without slot, (b) with diagonal slot.

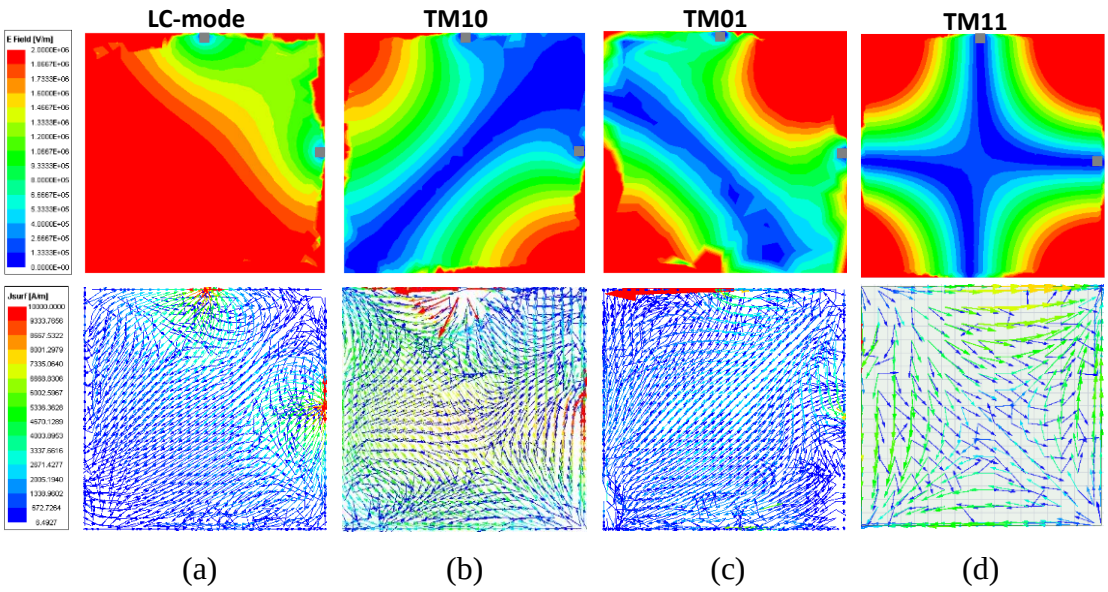

Figure 3.23: Electric Field and Current Density of Patch with TOP/Right edge *via*: (a) LC-mode, (b) TM_{10} mode, (c) TM_{01} mode, (d) TM_{11} mode.

vias might affect their resonance frequencies since it perturbs part of their E field simultaneously. To illustrate more about the effect of *vias* in this configuration, the *eigenmode* solution solver from ANSYS HFSS software is used to derive the E field and surface current J of the first 4 resonance modes, LC-mode, TM_{10}, TM_{01}, and TM_{11}, respectively. LC-mode has a full E field distribution across the patch geometry except at both positions of *vias* with its maximum current, flows radially, outside the *vias*, as shown in Figure 3.23 (a). TM_{10} and TM_{01} represent the degenerated modes of conventional patch with small modification on their E field at the TOP/RIGHT edges as shown in Figure 3.23 (b) and (c), respectively. This deformation is due to the existence of shorted *vias*. Generally, TM_{11} field is unaffected because vias are inserted at its maximum J as shown in Figure 3.23 (d).

For demonstration, a conventional patch resonator without any perturbation is designed with L_p = $\lambda/2$ at the operating frequency f_c =120 GHz. Since TM_{10} and TM_{01} are defined diagonally and operate at same f_c, D_t has to be deviated ($>$ 0 µm) to efficiently and separately excite one of them, along with TM_{11} that is defined at the 4 corners of the patch. This deviation is mandatory, for the moment, to avoid having zero transmission at f_c because fundamental modes are still uncoupled. Our focus in this filter design is to use LC-mode and TM_{10} mode only, while other modes will be used to improve the selectivity. The

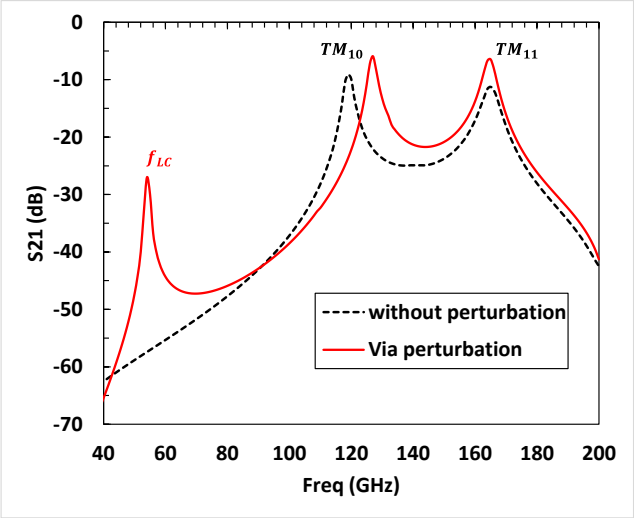

Figure 3.24: transmission response S21 for patch resonator with and without via perturbation.

patch resonator is weakly coupled and simulated using ANSYS HFSS software. The extracted transmission response S_{21} is plotted in Figure 3.24 where f_{TM10} = f_{TM01} = 120 GHz and f_{TM11} = 165 GHz. When *vias*, of $viad$ = 1 µm, are inserted, a new resonance mode f_{LC} appears at 55 GHz as shown Figure 3.24. f_{TM10} (f_{TM01}) is slightly shifted upward to operate at 128 GHz and f_{TM11} is fixed at 165 GHz. As in the previous filter design methodology, the patch resonator' size is reduced to have L_p = λ/4 at the same operating frequency of f_c = 120 GHz – thanks to the addition of *vias*. The first 3 resonances, f_{LC}, f_{TM10} (f_{TM01}), and f_{TM11} are shifted upward to re-operate at 106 GHz, 280 GHz and 380 GHz, respectively. For fine tuning and to illustrate more on the effect of *vias* size on the resonance frequencies, Figure 3.25 (a) shows the variation of the first 3 resonance frequencies versus $viad$. As previously discussed, the increase of $viad$ impressively affects and shifts upward f_{LC} and f_{TM10} (f_{TM01}). For instance, when $viad$ = 4 µm, f_{LC} = 120 GHz and f_{TM10} (f_{TM01}) = 295 GHz. As $viad$ increases and reaches 24 µm, f_{LC} = 150 GHz and f_{TM10} (f_{TM01}) is shifted to 350 GHz. A slight increase of f_{TM11} occurs, because when the size of *vias* increase, part of the *E* field of TM_{11} mode is shorted and so its resonance frequency is shifted upward.

After fixing $viad$ to 4 µm to have f_{LC} = 120 GHz, a diagonal slot of size L_d is inserted to mainly perturb the *odd*-mode TM_{10}. In this case, the degenerated modes are coupled and split. Figure 3.25 (b) shows the variation of the first 4 resonance frequencies versus L_d. In

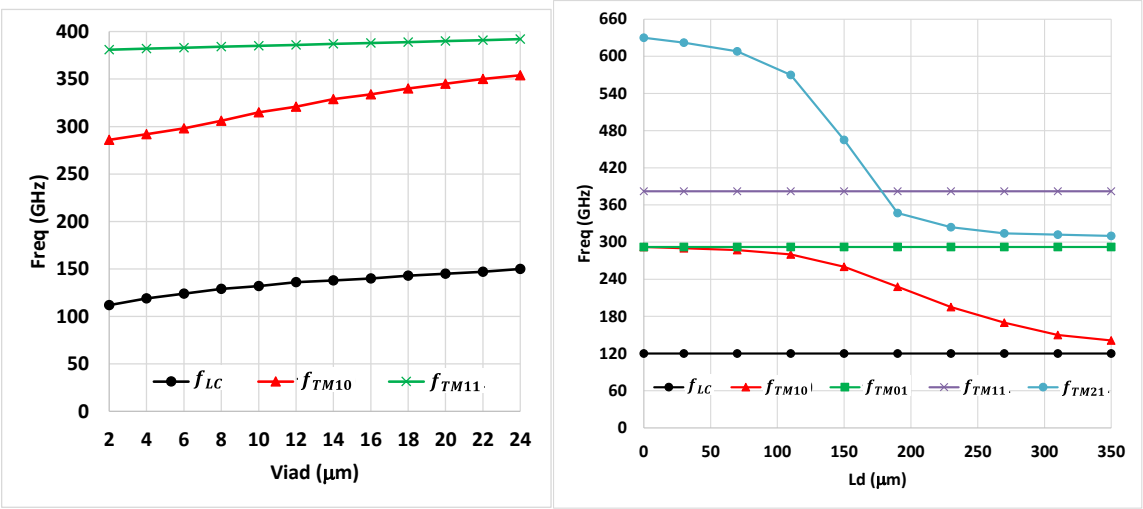

(a) (b)

Figure 3.25: Modified patch resonance frequencies variation with : (a) $viad$, (b) slot L_d.

addition to upper mode TM_{21} that is drastically affected by the diagonal slot because it efficiently perturbs its current flow. Starting with L_d = 0 µm, then f_{LC} = 120 GHz, f_{TM10} = f_{TM01} = 295 GHz, f_{TM11} = 382 GHz and f_{TM21} = 630 GHz. When L_d increases from 0 µm to 350 µm, f_{TM10} is drastically decreased from 290 GHz to 150 GHz. Also, f_{TM21} decreases from 630 GHz to reach 310 GHz, while f_{LC} and f_{TM01} are unaffected. Also f_{TM11} is slightly decreased and reaches 375 GHz.

This configuration of *vias* and slots shows its efficiency in building dual-mode filter with smaller size and better selectivity. Since it has the ability to bring the higher order modes from very far resonance frequency to operate at the upper-band rejection of the filter, which will create FTZs, as will be seen further.

Bandpass Filter Design

Following the same synthesis methodology presented previously, a dual-mode bandpass filter operating at 120 GHz with FBW of 20 % and return loss of 20 dB is designed. The final design configuration of the proposed filter is shown in Figure 3.26. As observed, 3 slots of lengths, L_{d1}, L_{d2} and L_{d3}, respectively, are added. Actually, when L_d is increased to its longest limit (350 µm), the lowest f_{TM10} that could be reached is 140 GHz, as shown in Figure 3.25 (b). This confines the availability to reach low FBW. So to solve this limitation in frequency shift, L_{d1} and L_{d2} slots are added. Moreover, L_{d3} is added to perturb both LC-mode and TM_{10} mode concurrently for center frequency control

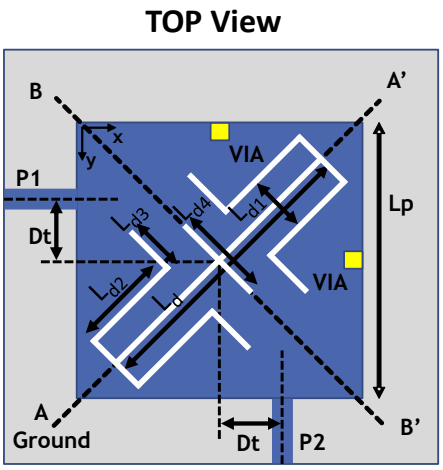

Figure 3.26: Proposed dual-mode patch resonator configuration with TOP/RIGHT edge *vias* and crossed slots.

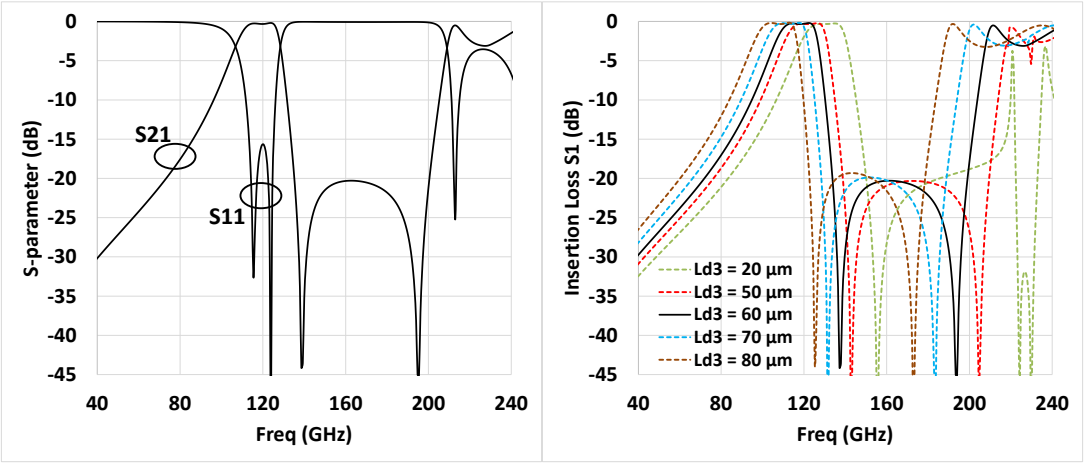

(a) (b)

Figure 3.27: (a) proposed dual-mode filter response, (b) variation of S_{21} (dB) versus L_{d3}.

without affecting the FBW. In addition, diagonal slot of length L_{d4} is inserted along *BB*' axis to fine tune the upper modes for better upper-band rejection, After optimization, the final elements' dimension of the filter are: L_p = 267 µm, D_t = 40 µm, $viad$ = 10.44 µm, L_d = 298 µm, L_{d1} = 70 µm, L_{d2} = 120 µm, L_{d3} = 60 µm and L_{d4} = 130 µm. The width W_s of all slots is fixed to 5 µm. Using the EM simulator from ANSYS HFSS the extracted responses for infinite Q are plotted in Figure 3.27 (a). The achieved results meet well with the initial definition of the filter of f_c = 120 GHz and FBW = 20 %. For more illustration on the effect of L_{d3} slot on the overall results, Figure 3.27 (b) shows the variation of the transmission coefficient S_{21} with L_{d3}. When L_{d3} increases, the whole filter response and f_c decreases. So f_c and L_{d3} are proportional to each other. This is due to the simultaneous

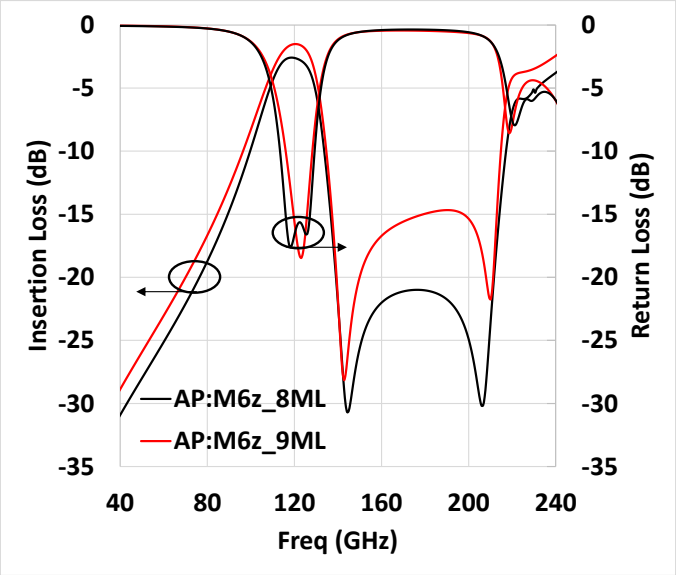

Figure 3.28: Comparison between 8ML and 9ML stack versions for dual-mode filter at 120 GHz with finite Q.

perturbation of both LC-mode and TM_{10} mode, since the position of L_{d3} is placed where the surface current of *vias* is high (see Figure 3.23). Also, TM_{10} becomes more sensitive to any added slot, since the path of its current is highly rerouted around all the slots along *BB*' axis. In this context, it is worth to mention that L_{d3} allows the controllability of center frequency without changing the FBW. Therefore, based on previous works on PCB technology as in [61], this filter could be tunable!.

In order to consider finite Q, the metallic layers are chosen to have aluminum conductivity for AP layer and copper for M6z layer. The achieved results for the proposed dual-mode filter is plotted in Figure 3.28. The recorded insertion loss is equal to 2.6 dB. The filter is well matched with return loss equal to 15 dB and FBW = 20%. In order to improve the performance and make the comparison between B55 8ML and 9ML versions, the same stack AP:M6z from B55 9ML is chosen. An optimization for some of the patch resonator elements is required to adjust the responses: L_p = 267 µm, D_t = 85 µm, $viad$ = 10.44 µm, L_d = 298 µm, L_{d1} = 70 µm, L_{d2} = 120 µm, L_{d3} = 55 µm and L_{d4} = 130 µm. The width W_s of all slots is fixed to 7 µm. The achieved results are plotted in Figure 3.28. The recorded S_{21} is -1.65 dB within the pass band, with return loss better than 20 dB and FBW of 20%. An improvement of 1 dB between B55 8ML and 9ML versions is achieved.

Based on this design analysis, single resonator was designed and implemented on B55-8ML:

1) A dual-mode bandpass filter operating at 120 GHz was developed on AP:M6z stack and denoted by F-11. It was synthesized to have return loss of 20 dB and FBW of 20 %.

In addition to those filters and to improve Q_u, 3 filters were designed and implemented on B55-9ML:

2) A dual-mode bandpass filter operating at 120 GHz on AP:M6z and M9v:M6z stacks denoted by F-12 and F-13, respectively. These filters were synthesized to have return loss of 20 dB and FBW of 20 %.
3) A dual-mode bandpass filter operating at 120 GHz on M9v:M6z stack denoted by F-14. It is synthesized to have return loss of 20 dB and FBW of 15 %.

3.2. 2nd Order Compact BandPass Filters at sub-wavelength (60 GHz)

3.2.1. Grounded Patch-Like Filter using CSRR

The usage of grounded vias in the middle of the patch (see Figure 2.7) has size reduction capability of approximately 75% (L_p = λ/4 at its center frequency). It is considered a significant reduce compared to the conventional patch, but it could be more. Taking a look to its *E* and *J* fields distribution in Figure 2.8, it shows that the surface current is radially flows starting from the *via* to the edges of the patch. So, in order to efficiently perturb it, the complementary split ring resonator (CSRR) is integrated within the patch geometry, as discussed further. To the best of our knowledge, (i) CSRR or patch resonators have never been implemented on CMOS/BiCMOS technology and (ii) it is the first filter study that combines grounded patch resonators with CSRR. The design of compact 2nd order grounded CSRR bandpass filter operating at 60 GHz and implemented on 55-nm BiCMOS technology is developed and explained in this subsection. It provides a design perspective with intensive size reduction.

Grounded CSRR Structure Analysis

Figure 3.29 shows different structures of proposed grounded patch resonators with different CSRR iterations. The conventional patch resonator is of size $\lambda/2$ and its

fundamental frequency f_c is determined by (3.2). Starting with the same length of patch resonator's (without via) as in section 3.1.2, L_p = 200 µm, its fundamental frequency appears at 375 GHz. After grounded *via* is inserted in the middle with size $viad$ = 4 µm, the lowest resonance frequency of different patch resonators' structures with same size is shown in Figure 3.30. When no CSRR is etched, the first resonance frequency appears at 185 GHz. It is drastically decreased to 80 GHz when first iteration of CSRR is introduced. This big shift in frequency shows the impressive impact of grounded vias and CSRR on miniaturization of patches. Then when two CSRR iterations is used, the resonance frequency is decreased down to 50 GHz. This shift is due to the elongation of the nominal electrical length of the signal from via to the output. It is worth mentioning that the physical

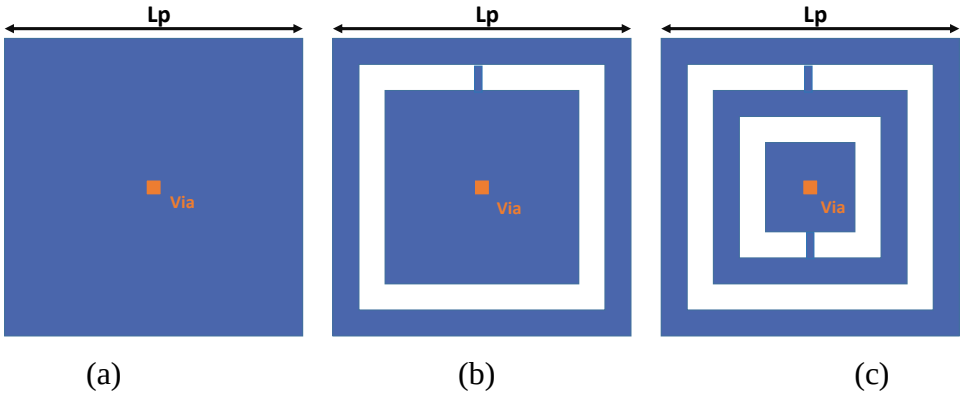

Figure 3.29: (a) Grounded patch resonator, (b) 1st iteration CSRR, (c) 2nd iteration CSRR.

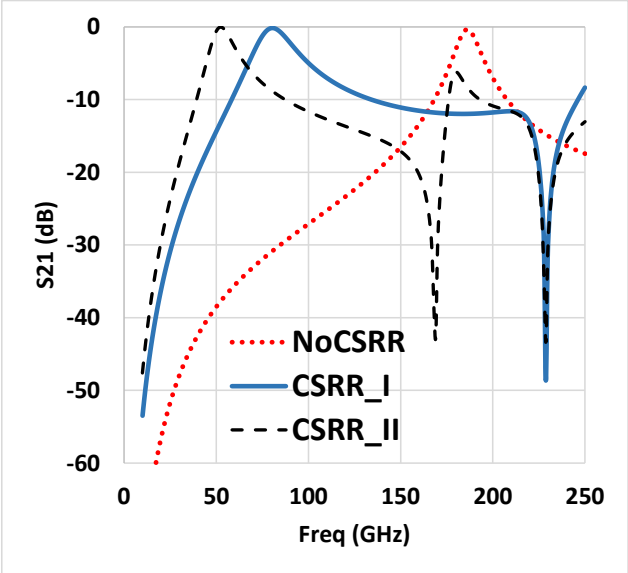

Figure 3.30: Resonance frequencies of grounded patch resonators of: NoCSRR, 1st iteration CSRR and 2nd iteration CSRR

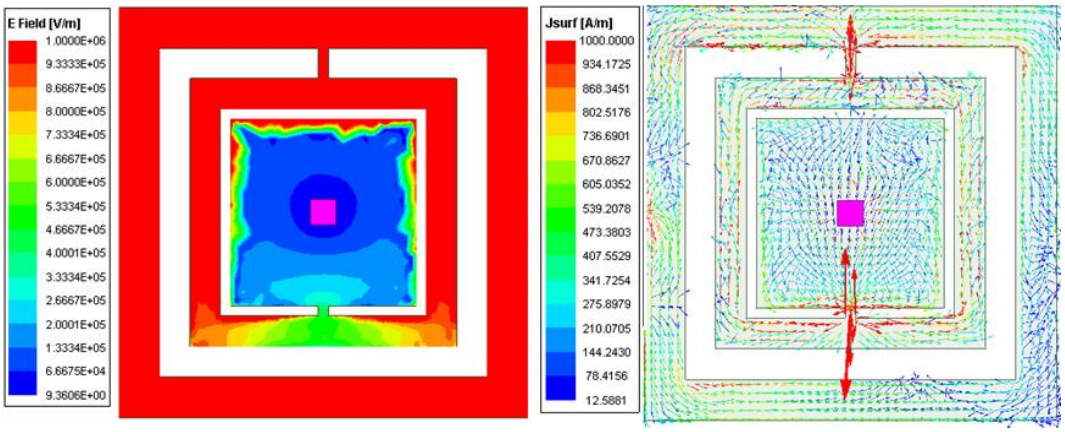

(a) (b)

Figure 3.31: (a) Electric field and (b) surface current distribution of 2nd iteration CSRR

outer length of the proposed patch resonator is extremely decreased from λ/4 with only via and no CSRR, to λ/14 with CSRR of 2nd iteration. Taking the advantage of the massive miniaturization of the patch resonator, the structure shown in Figure 3.29 (c) was selected.

It is very essential to observe the field distribution of the proposed structure in order to understand how to control the self-resonant frequency later in filter design. The grounded via resonance mode has a uniform electric field distribution across the CSRR surface except at its position, as shown in Figure 3.31 (a). While its surface current flow in Figure 3.31 (b) is directed radially outward/inward from/into via and follows the route through the small metal splits between the concentric etched rings. That means these small metal splits have a significant influence on fine tuning the resonance frequency of the resonator.

Filter Specifications and Synthesis Procedure

For designing the intended filter, a 2nd order Chebyshev filter response was chosen with fractional bandwidth (FBW) of 25 % and return loss of 20 dB. Its cascaded coupling scheme is shown in Figure 3.32. Each resonator has its single self-resonant frequency with resonator "1" only coupled to the source and resonator "2" only coupled to the load. There exists an indirect path between the source and the load created by the higher order modes. The lowpass prototype parameters were selected from [77] as follows: $g_0 = 1$, $g_1 = 0.6648$, $g_2 = 0.5445$ and $g_3 = 1.22$. In order to build up the normalized coupling matrix of the synthesized filter it is mandatory to determine a set of design parameters such as external quality factor and coupling coefficient that are calculated by (2.19) and (2.20), respectively.

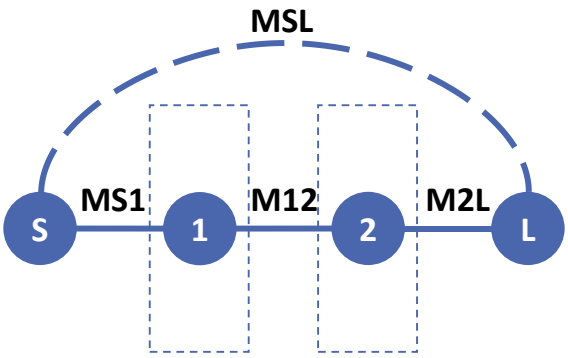

Figure 3.32: 2nd order bandpass filter equivalent cascaded coupling scheme (SL: source/load, 1: f_{01}, 2: f_{02}, solid line: main coupling, dotted line: S-L coupling cascaded coupling scheme.

The computed coupling parameters for the desired filter are: $Q_{e1} = Q_{e2} = 2.66$ and $M_{12} = M_{21} = 0.42$. It is worth mentioning that this kind of filter is of synchronous of tuning, i.e. the self-resonant frequency of each resonator is equal to the center frequency of the filter. In this context, the self-coupling parameters M_{11} and M_{22} are null. Also, both resonators are coupled to each other then $M_{12} = M_{21} \neq 0$. The chosen filter template, at first stage, is symmetrical, then there is no source-load coupling, i.e. $M_{SL} = 0$. The extracted normalized general coupling matrix is represented in (3.8).

$$m_{symmetrical \quad 2^{nd}-order} = \begin{bmatrix} 0 & 1.22 & 0 & 0 \\ 1.22 & 0 & 1.66 & 0 \\ 0 & 1.66 & 0 & 1.22 \\ 0 & 0 & 1.22 & 0 \end{bmatrix} \tag{3.8}$$

Filter design and Dimensions Extraction

The proposed 2nd order bandpass filter was designed and simulated using ANSYS HFSS software. Its design configuration is shown in Figure 3.33. The two resonators are implemented on the M8U:M1 stack from the B55-8ML version. They are electrically coupled by two small strips of length L_{12} on AP and M7 layers. In order to gain flexibility in controlling the external quality factor between the source/load and the resonator, a week coupling feeding aperture of length L_t at M7 layer was used. The orthogonal configuration of the feeding ports creates an indirect coupling between source and load, which leads to transmission zero at the upper band. In order to determine the physical length of feeding arm L_t, the method presented in CHAPTER II for Q_e extraction is used. The extracted Q_e is plotted in Figure 3.34 (a). It varies from 24 to 5 when L_t increases from 60 µm to 200 µm. Similarly, the direct coupling coefficient between the two resonators is determined from

(2.12), where f_{01} and f_{02} are the self-resonance frequencies of the two coupled resonators, respectively. The extracted M_{12} is plotted in Figure 3.34 (b). It varies from 0.11 to 0.33 when L_{12} increases from 5 µm to 50 µm. At first stage the simulation results exhibited larger FBW and noticeable passband ripple with bad out-of-band rejection. This is due to the initial values of the coupling matrix, which considers the filter as symmetrical with no

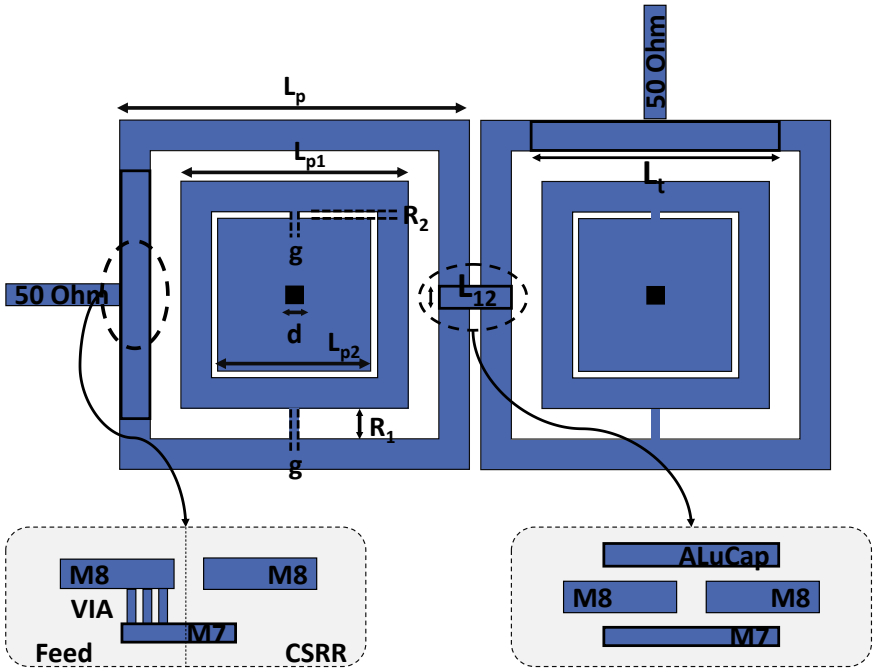

Figure 3.33: Layout configuration of proposed 2nd order filter.

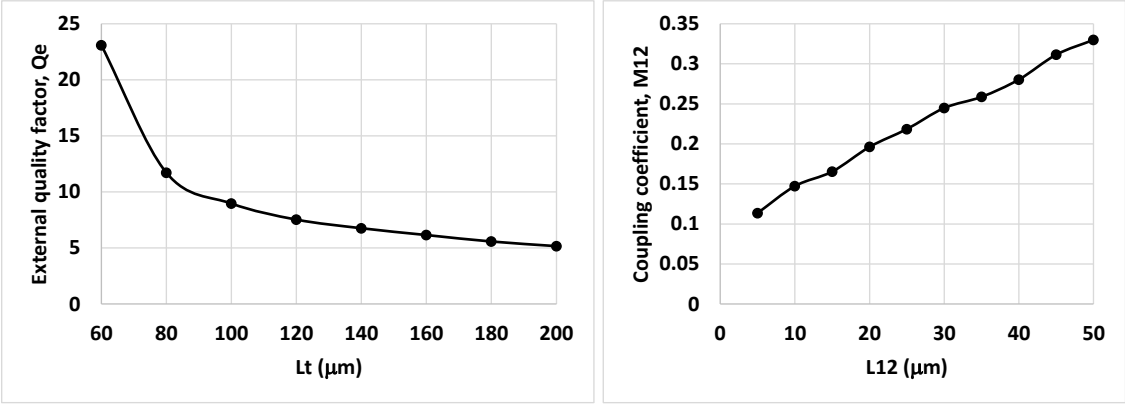

(a) (b)

Figure 3.34: (a) Extracted external quality factor for CSRR resonator at 50 GHz, (b) Extracted equivalent resonator-to-resonator coupling M_{12}.

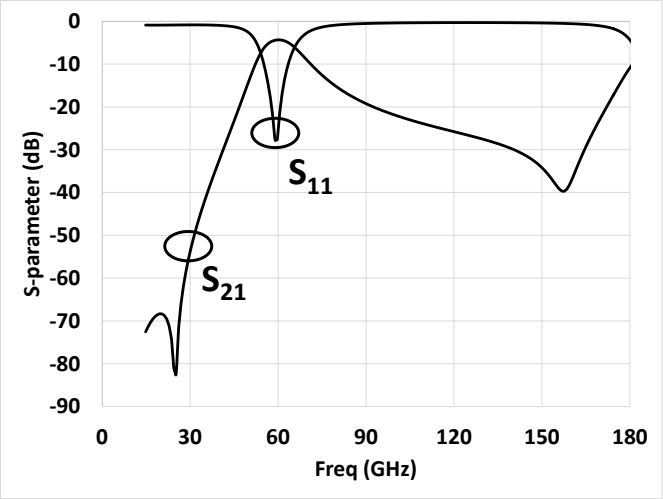

Figure 3.35: Simulated responses of the proposed 2nd order patch-like bandpass filter (L_p = 200 μm, L_{p1} = 160 μm, L_{p2} = 110 μm, g = 5 μm, R_1 = 20 μm, R_2 = 5 μm, $viad$ = 4 μm, L_{t1} = 200 μm, L_{t2} = 180 μm and L_{12} = 10 μm).

source/load coupling. In order to create coupling between source and load, reconfiguration of the feeding ports to have 90 degrees between them is required. Then filter synthesis using optimization technique is done. After coupling matrix optimization, M_{12}= M_{21} = 0.18, Q_{e1} = 5 and Q_{e2} = 5.5 mapping to final dimensions of L_{12} = 15 µm, L_{t1} = 200 µm and L_{t2} = 180 µm, respectively. The optimized normalized coupling matrix with infinite unloaded quality factor is represented in (3.9).

$$m_{asymmetrical \quad 2^{nd}-order} = \begin{bmatrix} 0 & 0.9 & 0 & -0.003 \\ 0.9 & 0 & 0.81 & 0 \\ 0 & 0.81 & 0 & 0.85 \\ -0.003 & 0 & 0.85 & 0 \end{bmatrix} \tag{3.9}$$

The achieved simulated results after taking into consideration the conductivity of all metallic layers are plotted in Figure 3.35. The recorded insertion loss is equal to 4.8 dB at the center frequency of 60 GHz. The filter is well matched with return equal to 28 dB, and fractional bandwidth FBW = 23 %. These results fit well with the defined filter template.

Based on this design analysis, a total of two filters were designed and implemented on B55-8ML version:

1) 1st and 2nd order patch filters at 60 GHz with same patch resonator topology were developed on M8U:M2M1 stack and denoted by F-15 and F-16, respectively. F-15

is used as a reference to extract its measured unloaded quality factor. The 2nd order filter F-16, was synthesized to have return loss of 20 dB and FBW of 20 %.

3.2.2. Ultra-Compact Patch Filter with Loaded "Mushroom"

Integrating shorting *vias* with patch resonators shows a great advantage to reduce the overall size of the filter. In this subsection an original ultra-compact patch resonator is introduced. Grounded *vias* are inserted with an extended stub at the corner of the conventional patch resonator. This allows a massive reduction of the patch size according to the analysis presented in CHAPTER II. In addition, the modified patch is loaded with shorted "mushrooms" to control its fractional bandwidth. Those mushrooms can be modeled as loaded capacitance to the patch. For proof of concept, a 2nd order patch filter is designed at 60 GHz for future 5G/6G applications with FBW of 20 %.

Modified Patch Resonator

The analysis presented previously in section 2.1.2, showed that the lowest resonant frequency of grounded patch resonator is achieved when the *via* is placed at the corner. In order to decrease it more, the corner is extended by a stub (length L_s and width W_s), which is shorted at its end by via of size $viad$, as shown in Figure 3.36 (a). Orthogonal feeding port structure is used with D_t deviation from center of origin.

For demonstration, a conventional patch resonator of initial size L_p = 360 µm is implemented on M8U:M1 stack from B55-8ML version, where its fundamental frequency operates at 200 GHz. ANSYS HFSS software is used for design and simulation. When via is inserted at the corner of the patch (without stub extension), the lowest resonance frequency for LC-mode appears at f_{LC} = 55 GHz, as shown in Figure 3.36 (b). As long as the extended stub is inserted, f_{LC} is impressively decreased. For example, when L_s = 100 µm, f_{LC} reached 28 GHz. Then it decreased to 18 GHz when L_s is extended to 400 µm. So, as the extended stub is elongated, the electrical length θ_{via} of LC-mode is increased and this decreases f_{LC} as well. Using the *eigenmode* solver from ANSYS HFSS software, the *E* field and surface current *J* distribution of f_{LC} are extracted and shown in Figure 3.37. As expected, the surface current flows from *vias* through the extended stub to reach the output port. Also, maximum E field occurs at the corners along *AA*' and *BB*' axes, where *J* is null. In this case, D_t has to be deviated forward/backward to excite the structure at its

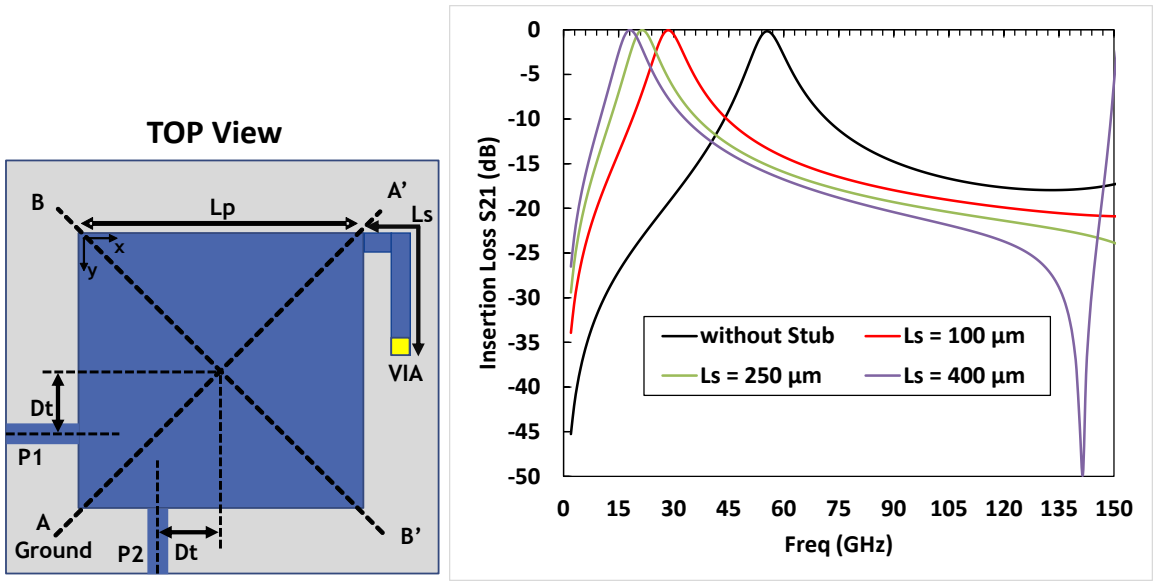

(a) (b)

Figure 3.36: (a) modified patch with extended stub, (b) variation of S_{21} with extended stub length L_s.

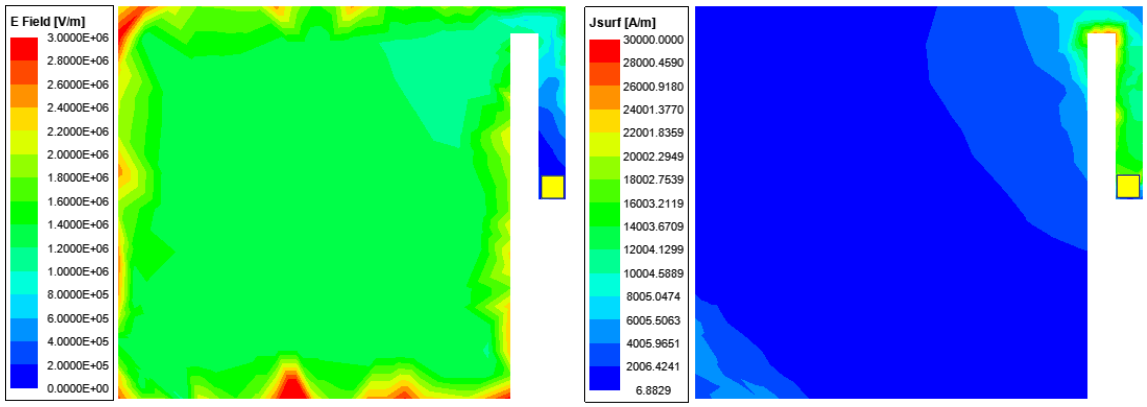

(a) (b)

Figure 3.37: modified patch with extended stub: (a) E field, (b) surface current J.

corner. Also this will help in improving the out-of-band rejection.

Our interest in this approach is to present a patch resonator that operates at 60 GHz, so the modified patch is resized to have f_{LC} = 60 GHz for L_p = 140 µm, L_s = 160 µm and W_s = 10 µm. Resizing the patch depends on how much miniaturization is needed. In our case, we took the maximum limit. In this context, if a conventional patch of size $\lambda/2$ is to be designed at 60 GHz, L_p should be set to 1250 µm ($\lambda/2$). However with our approach, L_p is drastically decreased to be of size $\lambda/18$. This impressive size reduction allows, approximately, 99 % of overall layout miniaturization according to the methodology used

in (2.5). In this case, the proposed modified patch resonator could be comparable to the structures presented in [12] using microstrip line topologies.

The advantage in size reduction came on the expense of bandwidth enlargement as shown in the simulated results in Figure 3.38. As explained in CHAPTER II, the resonance mode created by the *via* is modeled as LC circuit. In this case, when patch size is decreased, the overall capacitance C_p of the patch is decreased as well. For any LC circuit, bandwidth is inversely proportional to the capacitance. This is why the FBW is enlarged and reaches 85% at 60 GHz. In order to compensate the increase of bandwidth, the modified patch is loaded with "mushroom". The proposed patch resonator is shown in Figure 3.39. The loaded "mushroom" structure is a metallic floating plate of length L_m and width W_m connected with vias of size $viam$ to the ground. It is implemented at M7z layer to create a loading capacitance with the patch. Multiple of "mushrooms" are needed to compensate the lost capacitance and their distribution is controlled by the technology design rules that will be illustrated in the coming chapter. Moreover, 4 etched slots of length L_h and width W_h are inserted along the vertical and horizontal axes of the patch in order to control FTZ, that is appeared at 210 GHz. This FTZ is created by the upper modes, which is here the degenerated modes. Since both ports are deviated toward the same corner with $D_t < 0$ µm ($D_t > 0$ µm), then the upper excited mode is the *even*-mode (or the *odd*-mode).

In order to illustrate more on the reduction of FBW, Figure 3.40 (a) shows the variation

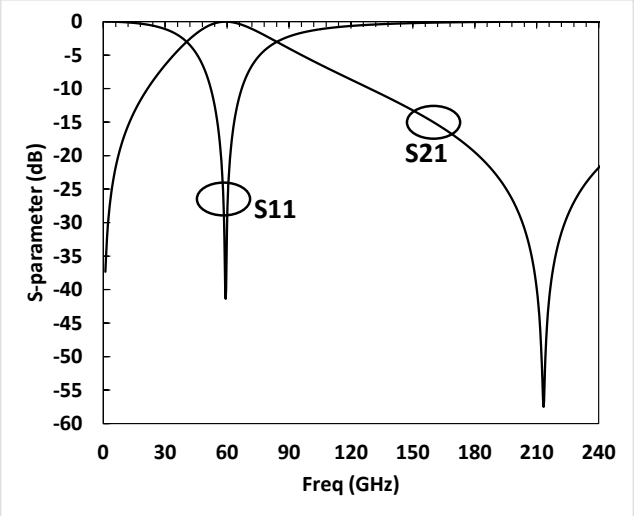

Figure 3.38: Simulated responses of the modified patch resonator with extended stub at 60 GHz.

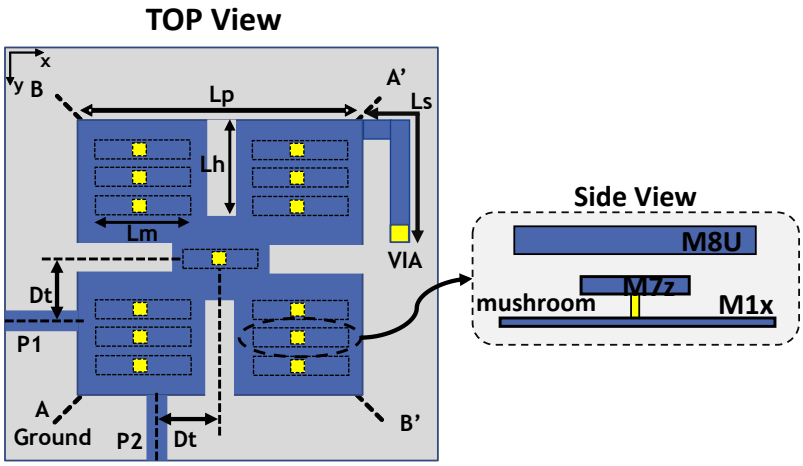

Figure 3.39: Proposed ultra-compact patch resonator with extended stub and loaded mushroom.

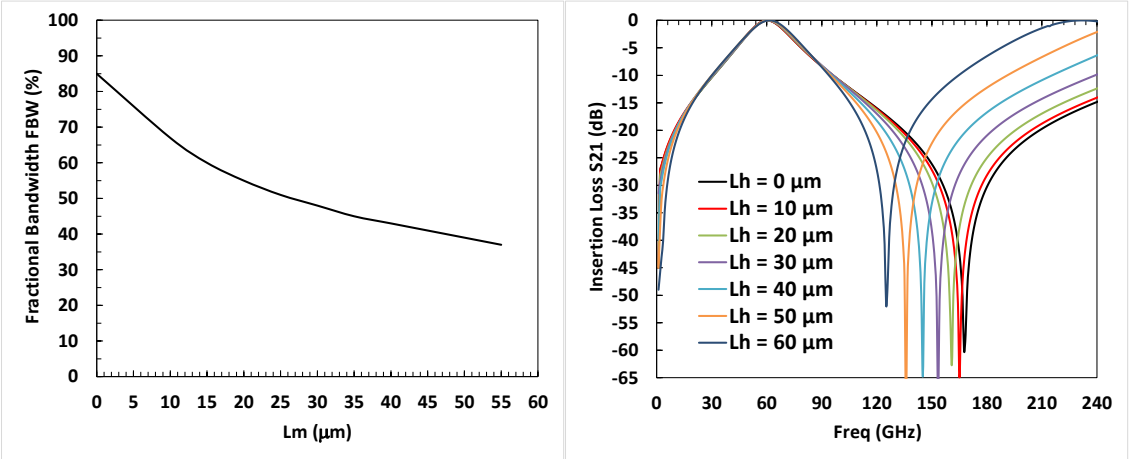

(a) (b)

Figure 3.40: (a) variation of FBW with the "mushroom" plate L_m, (b) variation of FTZ with etched slot L_h.

of FBW versus the variation of L_m. W_m and $viam$ are both set to 10 µm and L_h is set to 0 µm. When no "mushroom" loads are inserted, FBW is 85 %. It decreased to 38 % when L_m increased to 55 µm. Although, it is better to select the lowest possible FBW, this has a negative impact on the insertion loss when copper metal conductivity are set. So, for better compensation, the overall structure is re-optimized and the final dimensions are: L_p = 142 µm, L_s = 58 µm, W_s = 10 µm, L_m = 45 µm, W_m = 12 µm $viad$ = 14.4 µm, $viam$ = 6.8 µm and D_t = -50 µm. The simulated results are shown in Figure 3.40 (b). When L_h = 0 µm, FBW is dropped to 42 %, thanks to the usage of loaded mushrooms and the availability of multilayers of the technology. FTZ appeared at 175 GHz. In order to control the presented FTZ, L_h is varied. When L_h reaches 60 µm, FTZ is decreased to 125 GHz.

Also, the variation of L_h has no impact on the overall response of the patch resonator. Since both FBW and FTZ can be easily tuned, higher order bandpass filters can be designed.

Second Order ultra-compact bandpass filter

For the proof of concept, and following the same synthesis methodology presented in the previous subsection, a 2nd order bandpass filter operating at 60 GHz using the proposed "mushroom" loaded patch resonator is designed. The filter is designed to have Chebyshev response with FBW of 25 % and return loss of 20 dB. The overall structure of the proposed filter is shown in Figure 3.41. Two "mushroom" loaded patch resonators are cascaded and coupled to each other. In order to control the couplings between both resonators, two floating metals of length L_c and width W_c are inserted at AP and M7z layers. After design optimization using ANSYS HFSS software, the achieved results are shown in Figure 4.42. M8U and M1 layers are set to have copper conductivity. The recorded insertion loss is 3 dB with FBW of 28 %. The filter is well matched with return loss better than 15 dB. Since D_t is deviated to the corners, not only this allows to create FTZ in the upper band, but also, an indirect path between P_1 and P_2 is occurred and created FTZ in the lower band too. Also, with such kind of resonator it could be possible to design more sophisticated filter with cross-coupled synthesis approach and using the B55-9ML version for better selectivity and

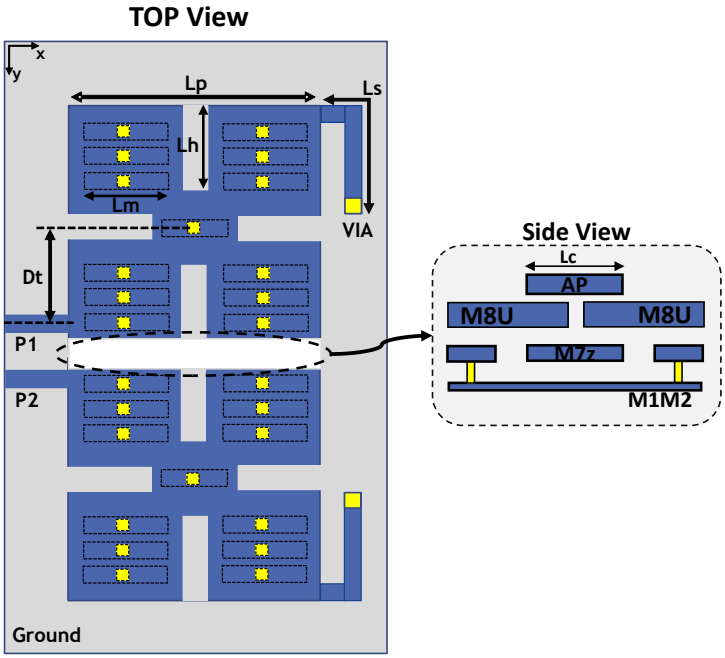

Figure 3.41: Configuration of 2nd order ultra-compact patch bandpass filter at 60 GHz with extended stub and loaded "mushroom".

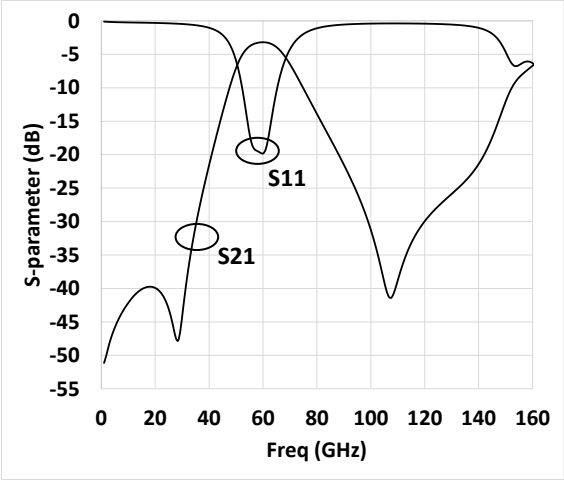

Figure 3.42: Simulated 2nd order ultra-compact patch bandpass filter with loaded "mushroom" (L_p = 142 μm, L_s = 50 μm, W_s = 10 μm, L_m = 45 μm, W_m = 10.8 μm $viad$ = 14.4 μm, $viam$ = 6.8 μm, L_c = 142 μm, W_c = 20 μm and D_t = -67 μm).

FBW. This will be developed in the future.

Based on this design analysis, a total of two filters were designed and implemented on B55-8ML version:

1) 1st and 2nd order patch filters at 60 GHz with same patch resonator topology were developed on M8U:M2M1 stack and denoted by F-17 and F-18, respectively. F-17 is used as a reference in order to extract the measured unloaded quality factor of the proposed resonator. The 2nd order filter F-18 is synthesized to have return loss of 20 dB and FBW of 25 % for the proof of concept.

3.3. Conclusion

This chapter presented different kinds of patch filters, which were implemented on different layers of B55 8ML and 9ML integrated technology.

Dual-mode single band and dual-band bandpass filters operating above 100 GHz were thoroughly synthesized and developed. Flexible responses were achieved, thanks to the combination between grounded *vias* and slots. Following the same synthesis methodology, more selective filter was developed at an operating frequency of 120 GHz. With this type of filters, upper out-of-band rejection was improved through creating multiple FTZs.

Another kind of filters based on conventional cascaded synthesis scheme were developed at 60 GHz. The focus was to present a new approach for patch resonators that

can be used for 5G applications at sub-wavelength band with very compact size. The first patch resonator topology combines both CSRR and grounded *vias*, while the other one is a grounded patch resonator loaded with “mushroom”. A massive miniaturization of 99 % was achieved as compared to a conventional patch resonator at the same frequency.

All the presented modified resonators are original and were not designed before on PCB or other technologies. The multi-layering availability within the used technology shows a great interest to develop more sophisticated filters without additional design complexity. The combination of both different versions of B55 with same filters topologies, showed a great interest of the 9ML technology in terms of Q_u improvement, which leads to better performance. This will be more focused in the coming chapter where measurement results are analyzed.

CHAPTER IV: LAYOUT DESIGN & MEASUREMENT RESULTS

Passive circuit layout is relatively complicated for advanced CMOS/BiCMOS technologies, due to the strict rules enacted by the manufacturer in the Design Rule Manual DRM. During the layout procedure, Design Rule Checker DRC has to be checked more often, mainly for different implementation rules like: metal density, precision dimensions …etc. In this chapter different layout steps, in order to successfully send all the layouts for fabrication, are explained. Also, it is shown the effect of different design rules on the performance of the filters and how it can be compensated. As a second step, measurement results are thoroughly analyzed and comparison with the state-of-art is conducted.

4.1. Layout Design and Technology Constraints

For mm-wave IC circuit design, more advanced CAD design tools are required. In order to sketch the layouts of the presented filters, Cadence Virtuoso® software was used and the Process Design Kit (PDK) was supported by STmicroelectronics for BiCMOS 55 nm technology. For confidentiality the design rules values cannot be specified. The layout methodology is driven by three main steps: i) implementation of the filter configuration on its intended layer stack, ii) fulfill the empty and unused metal layers to satisfy DRC and study the losses mechanism, iii) post layout simulation.

During the first step, each filter configuration is implemented on its intended layer, which for our patches are: AP, M8U and M9v layers. These layers share approximately the same precision dimensions rules with less complexity compared to lower layers. Since patch resonators use big strips in size, the first rule to be satisfied is the min/max allowed width for strips. There is no issue with the min limit, though with the max limit. In order to overcome it, small etched slots (with no significant impact) are inserted in specific places (Figure 4.1 (a)) as required by the DRC. Afterwards, the second rule to satisfy is the min/max allowed metal density for the used stack. This rule is only tested when the whole design of a given filter layout is implemented. Taking the example of the filter in Figure 3.39, where there is full metal patch parts that exceed the max allowed limit, it is solved by adding some etched slots as shown in Figure 4.1 (b). Those slots are inserted in parallel to the flow of current to minimize their impact. This issue doesn't exist with the filters shown in sections 3.1.1 and 3.1.2 where a lot of etched slots initially exist. The max allowed

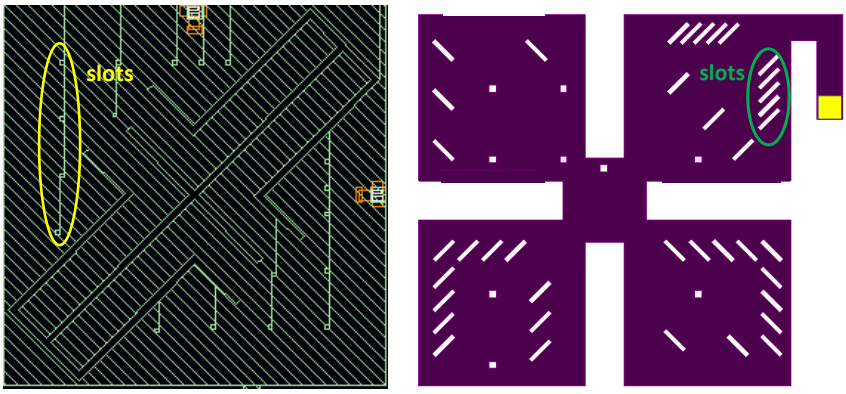

(a) (b)

Figure 4.1: Layout: (a) filter design in section 4.1.3, (b) filter design in section 4.2.2.

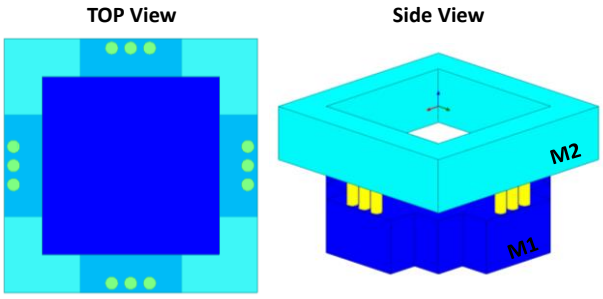

Figure 4.2: stacked ground unit cell.

metal density issue can be more highlighted with the implementation of the ground. In all of the presented filter designs, full metal ground is used. In order to satisfy the DRC with less impact on the performance, stacking multiple layers is the solution. Figure 4.2 shows the configuration of a unit cell of a given stack where both layers form an interconnected mesh. In case M1 is selected, M2M1 is stacked instead, and in case M6z is selected, M6zM5x is stacked.

At this layout step, the conductivity of the metals, especially for *vias*, has to be well extracted due to some technology fabrication constraints. According to the DRM, there exists a contact resistance with by very high resistivity between each metallic/dielectric layer, which drastically reduces the conductivity of the used *vias*. So, *vias* were modeled using maxwell-3D solver from ANSYS HFSS to extract its equivalent conductivity to be near to the real fabricated ones. In our case, the equivalent conductivity for *vias* that are used is $\sigma_v = 1.6 \cdot 10^6$ S/m.

The second step in the layout procedure is to fulfill the unused metal layers with the minimum floating metal possible, which are referred as “dummies”. The added dummies

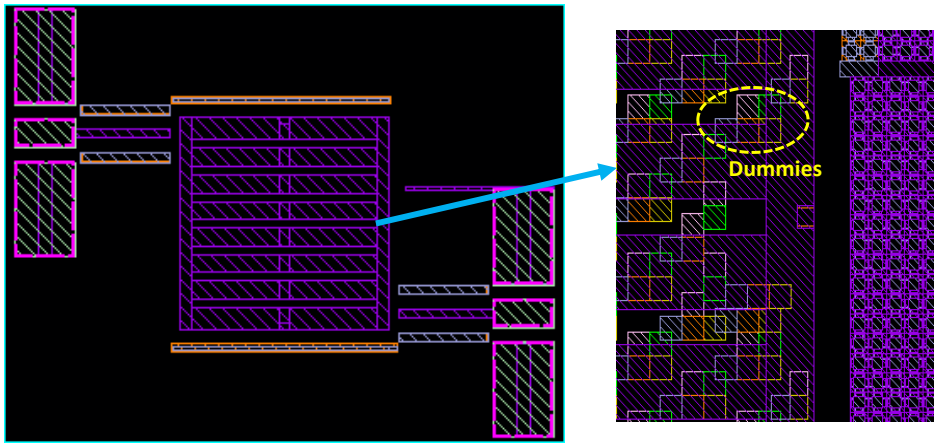

(a) (b)

Figure 3.3: (a) Layout design for filter in section 4.1.2, (b) zoom in to highlight dummies placement.

have double drawback, (i) they modify the electric field lines, with a capacitive effect under the patch and under the slots, and (ii) they generate losses by eddy current. For illustration, the layout of the dual-band filter designed in section 3.1.2 is given in Figure 3.3 (a). In Figure 3.3 (b), the dummies that were added in M3x to M7z layers are highlighted in a "zoom". The size of these dummies was fixed near to the minimum allowed by the technology, in order to reduce eddy current losses. Also, the placement of these dummies was carefully optimized. They have been placed in staggered rows with no overlapping between them in order to minimize the possibility for the electric field to jump from one metallization level to another, with the consequence of reducing the effective height between the patch and the ground plane, thus modifying the patch response. Moreover, the presence of dummies close to the *vias* leads to high losses, probably linked to the eddy currents induced due to the strong current flowing in the *vias* and therefore the strong magnetic field around the *vias*. Therefore, placing dummies in these areas should be avoided if possible. Also, the presence of dummies at the level of the slots leads to a slight modification of the resonant frequencies of the modes. This must therefore be considered when modifying the dimensions of the slots.

Expected Losses Study

Losses mechanism study based on EM simulation using ANSYS HFSS was carried out to recognize the occurrence and identify the dominant losses. For illustration, a dual-mode filter presented in section 3.1.1 is selected. Table 4.1 summarizes the expected losses for a

Table 4.1: Losses Study For Proposed Patch Filter in section 4.1.1.

Patch Conductivity	*Via Conductivity*	*Floating Dummies*	*IL @ oper. freq (dB)*
∞	∞	none	0.08
Nominal	Nominal	none	2.2
Nominal	Nominal	Near via	4.2
Nominal	Low	none	5.4
Nominal	Low	Near via	7.5

different configurations at the operating frequency. When perfect metal is used for the patch and *vias* with no insertion of dummies, the insertion loss is almost null (0.08 dB). This means the loss tangent of S_iO_2 dielectric of the BEOL reveals to be negligible, as expected. For nominal patch and via conductivity σ_p and σ_v, respectively, and without any floating dummies added, the filter's insertion loss is equal to 2.2 dB. Fixing the patch conductivity to its nominal value, different cases for via conductivity (according to the technology PDK) and presence of floating dummies were studied as follows:

1) For σ_v at its nominal value and floating dummies just near the *via*, 2 dB of losses is added, leading to overall insertion loss of 4.2 dB.
2) For σ_v at its low value and no floating dummies, the filter records an addition of 3.2 dB of loss. Then when dummies are added the overall insertion loss increases and reaches 7.5 dB.

Therefore, to avoid any additional losses to the designed filter, floating dummies were inserted with no overlapping between them and placed away from the *vias* as much as the DRC allows. Also *vias* were thoroughly modeled to reveal actual fabricated via. After that, a post-layout simulation was carried out to verify the desired performance. Since the designed filter's response is fully controllable, acceptable performance was reached, as presented in the next subsections.

The last step in the IC design is the post layout simulation. In case of performance deficiency, re-optimization of the filter design has to be performed. Afterwards all filters are sent to fabrication. Usually fabrication process takes around 6 months before the measurements. During this dissertation, we had the chance to participate in 4 tape outs: BUKA 2020, BADU 2021, BEAR 2021 and BEQUIA 2022. All tape outs are received except for BEQUIA 2022, which will be available for measurments in March 2023.

4.2. Measurement Setup

S-parameters measurement was performed in two different laboratories: CIME-NANOTECH at Grenoble and IEMN at Lille. At CIME-NANOTECH, two different VNAs were used: Anritsu VectorStar® ME7838A4 VNA to cover the band from 70 kHz to 145 GHz, and R&S ZVA VNA to cover the G-band from 140 GHz to 200 GHz. While at Lille R&S ZVA24 VNA was used to cover the band from 220 GHz to 325 GHz. Figure 3.4 shows a photo of the Anritsu VectorStar® measurement setup, with the ANRITSU probes and measurement heads above the wafer.

On-wafer measurements of the implemented filters were performed and each time with a first-tier on-wafer TRL calibration. For each stack and with each tape out run, different TRL calibration kits were used. Figure 4.5 shows the "Thru" for the two types of TRL calibrations that were used. Figure 4.5 (a) "classical" Thru is used with most of the filters with two ports GSG probes. Figure 4.5(b) "specialized" Thru is used with filters discussed in section 3.2.2 where a single GSGSG probe is used due to small gap between the two feeding ports in the design. GSG pads having a pitch equal to 50 µm were used for probes mounting.

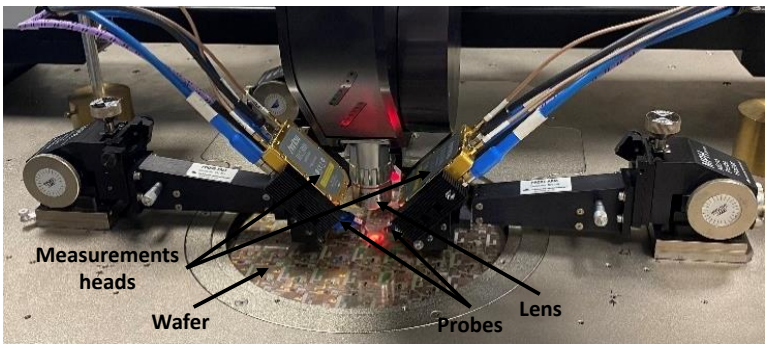

Figure 3.4: Anritsu VectorStar® ME7838A4 VNA measurement setup.

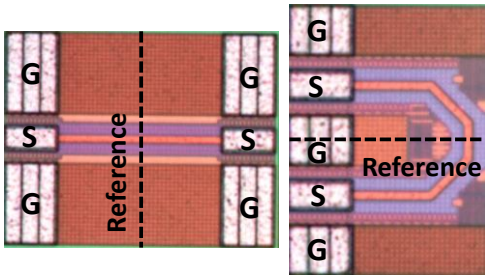

(a) (b)

Figure 3.5: (a) classical Thru, (b) specialized Thru.

4.3. On Chip Filters Measurement

4.3.1. Dual-Mode Filters above 100 GHz

Grounded Patch Filter with Collinear Feeding

On-wafer chip layout for single patch resonators operating at 200 GHz, F-Ref1 and F-Ref2, are shown in Figure 4.6. F-Ref1 and F-Ref2 are implemented on B55-8ML M8U:M2M1 and AP:M6zM5x stacks, respectively. The overall size for both resonators is 0.13 mm^2, particularly with a patch side length of 360 µm. Both patches are the reference designs for all the developed filters. Also, two different stacks were used in order to compare the extracted unloaded quality factor Q_{us} for a single patch resonator, which to our best knowledge will be measured for the first time. Q_{us} is calculated from (4.1) for loaded resonators with single response [77]:

$$S_{21} = 20 \cdot \log(1 + \frac{1}{FBW \cdot Q_{us}}) \tag{4.1}$$

where FBW is the fractional bandwidth.

The measurement results in comparison to the simulated ones are shown in Figure 4.7(a) and Figure 4.7(b), respectively. The agreement between measurement and *EM* simulation results is acceptable. Although, the measured insertion loss is higher (F-Ref1: 4 dB & 5dB ; F-Ref2: 3dB & 4 dB, in simulation and measurements, respectively), this can be partially explained by a bandwidth reduction between simulation and measurement results. Thus, their Q_{us} are very close, i.e. 22 and 25 in simulation for F-Ref1 and F-Ref2, respectively, against 18 and 20 in measurements. As expected, the highest Q_{us} is obtained for the stack

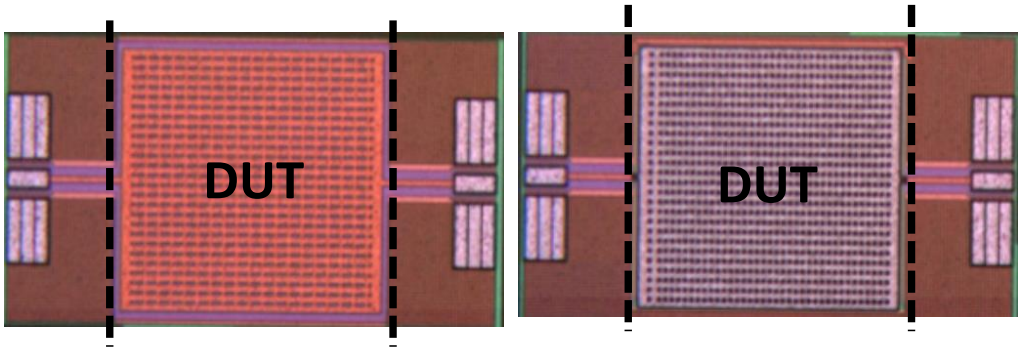

(a) (b)

Figure 4.6: On-wafer chip reference single patch resonators at 200 GHz: (a) F-Ref1 stack M8U:M2M1, (b) F-Ref2 stack AP:M6zM5x.

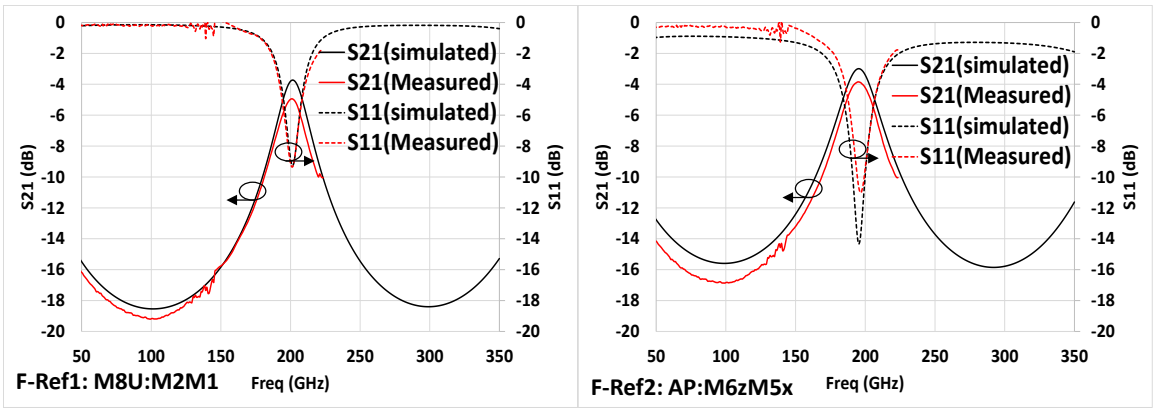

(a) (b)

Figure 4.7: Reference single patch resonators measurement results: (a) F-Ref1. (b) F-Ref2.

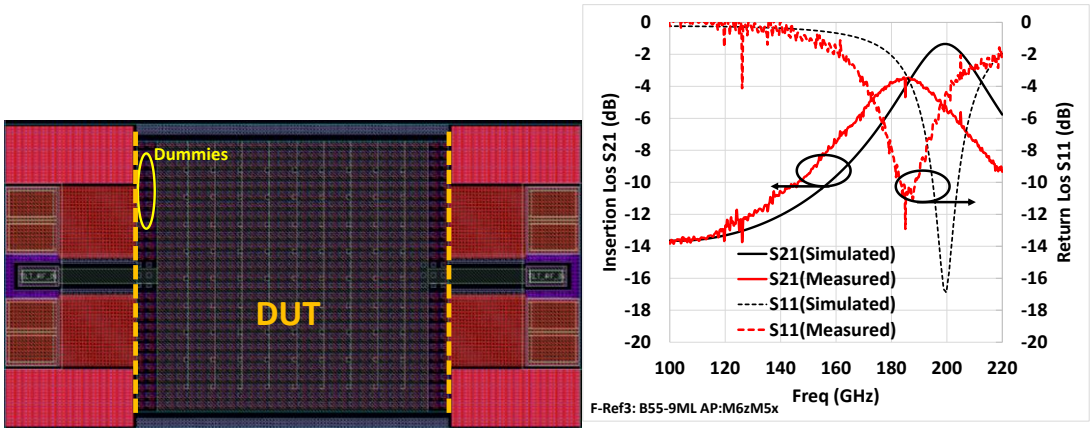

(a) (b)

Figure 4.8: Reference single patch resonator F-Ref3 on B55-9ML AP:M6zM5x stack: (a) Layout, (b) Measurement results.

AP:M6zM5x, due to the increase in dielectric height and ground thickness. Measurement results for reference single patch resonator F-Ref3 operating at 200 GHz, which is implemented on B55-9ML AP:M6zM5x stack, is shown in Figure 4.8 (a). The big shift of frequency in measurement results is due to the big amount of dummies inserted below the patch, as shown in Figure 4.8 (b). For that purpose, it was re-sent to BEQIUA2022 tape out (not received yet) with tolerated amount of dummies. Also, reference single patch resonators operating at 120 GHz couldn't be sent into fabrication due to their big size.

On-wafer chip layout for dual-mode patch filters, F-1 (symmetrical feeding structure) and F-2 (asymmetrical feeding structure), operating at 120 GHz and implemented on B55-8ML M8U:M2M1, are shown in Figure 4.9 (a) and Figure 4.9 (b), respectively. Also, dual-mode patch filters, F-3 (symmetrical feeding structure) and F-4 (asymmetrical feeding

structure), operating at 200 GHz and implemented on B55-8ML M8U:M2M1, are shown in Figure 4.9 (c) and Figure 4.9 (d), respectively. In addition to a dual-mode filter F-5 (asymmetrical feeding structure) operating at 200 GHz and implemented on B55-8ML AP:M6zM5x stack is shown in Figure 4.9 (e). The Device Under Test (DUT) is excited by 50 Ω feeding lines, which are of microstrip type and coming from the PDK. The overall size of filters at 120 GHz is 0.084 mm^2 (side length of 290 µm) and those at 200 GHz is 0.037 mm^2 (side length 194 µm). A remark to mention, filter F-6 (see Figure 3.11) that is implemented on B55-9ML M9v:M6z stack was sent to BEQIUA2022 tape out, which is not received yet.

The measurement results of F-1 and F-2 operating at 120 GHz are given in Figure 4.10 (a) and Figure 4.10 (b) respectively. The agreement between measurements and *EM* simulations is good, with only a slight increase in insertion loss. The simulated insertion loss is approximately 4.5 dB as compared to about 5 dB in measurements. Both filters are

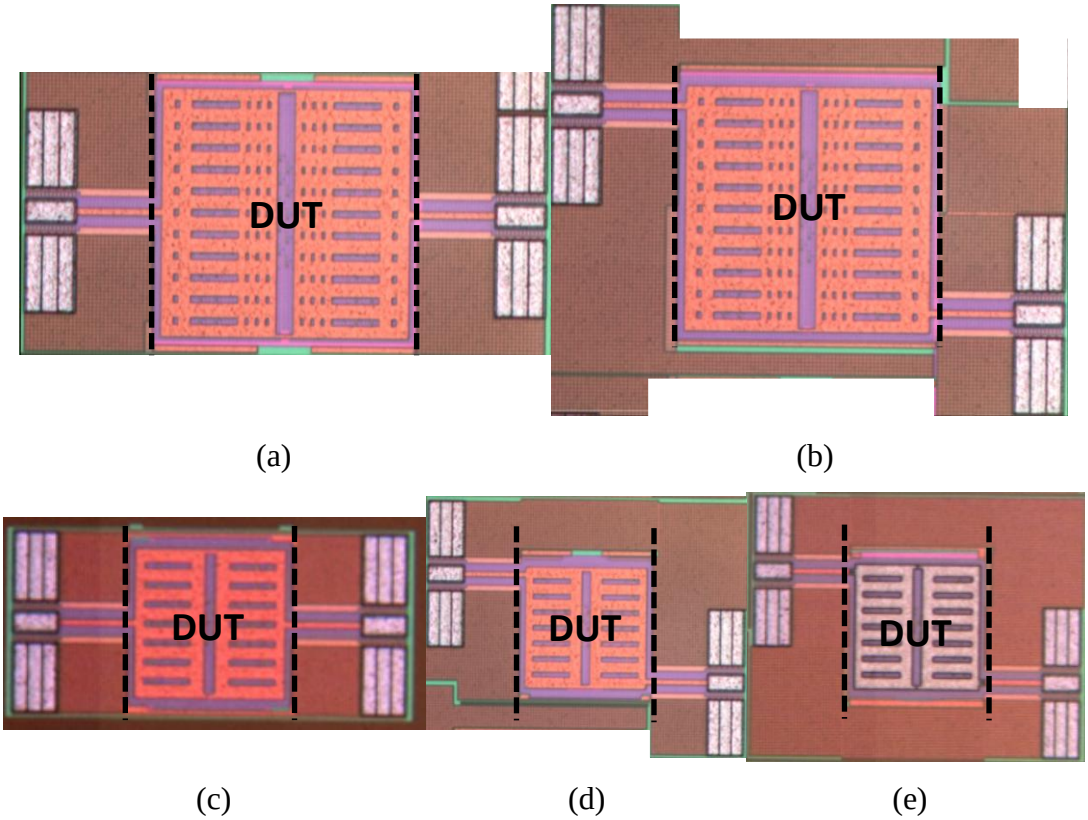

Figure 4.9: On-wafer chip dual-mode patches: 120-GHz stack M8U:M2M1: (a) F-1 Symmetrical feeding, (b) F-2 Asymmetrical feeding; 200-GHz stack M8U:M2M1, (c) F-2 Symmetrical feeding, (d) F-4 Asymmetrical feeding; 200-GHz stack AP:6zM5x, (e) F-5 Asymmetrical feeding.

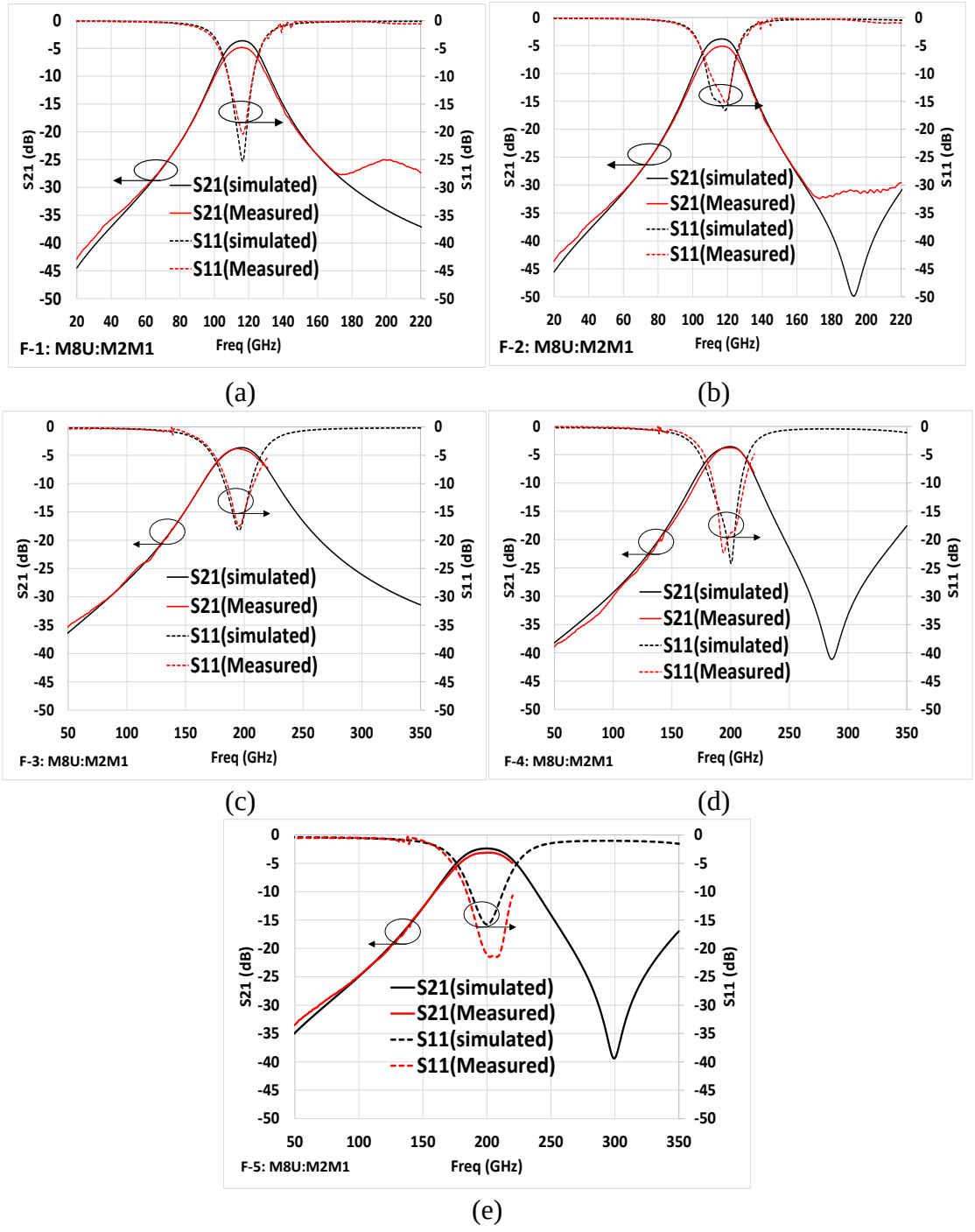

Figure 4.10: Dual-mode patch filters measurement results: (a) F-1, (b) F-2, (c) F-3, (d) F-4, (e) F-5.

well match with a return loss greater than 15 dB and FBW of 19%. A transmission zero was expected for asymmetrical feeding. If the transmission response for the filters operating around 200 GHz is observed, it is seen that the rejection is stronger for the asymmetric feeding, but the transmission zero does not appear in measurement. Probably this is related to the calibration that lacks to precision that does not allow measuring low

enough transmission levels in G-band. Measurement results of F-3 and F-4 operating at 200 GHz and designed on M8U:M2M1 stack, are given in Figure 4.10 (c) and Figure 4.10 (d), respectively. The agreement between measurements and *EM* simulations is very good, for both S_{21} and S_{11}. The measured insertion loss is about 3.8 dB for both filters, with matching greater than 15 dB. The measured FBW for F-3 is 22 % while for F-4 it is 18 %. As measurement capabilities were limited to 220 GHz, the transmission zero could not be observed. Finally, the measurement results of F-5 operating at 200 GHz and designed on AP:M6zM5x stack, are given in Figure 4.10 (e). Here again, the agreement between measurements and EM simulations is good. The measured insertion loss is about 3 dB, i.e. the lowest of all the designed filters.

In terms of general conclusion, several remarks can be deduced from all these results. Firstly, and as expected, the quality factor of the resonators increases with the frequency, thus the insertion loss, for the same bandwidth, decreases. Secondly, the AP:M6zM5x stack makes it possible to obtain slightly higher performance for conventional patches. Moreover, the advantage of using an AP:M6zM5x stack can be the non-use of the lower layers, which can then be used for routing operations. Active components (diodes, transistors) could also be made under the patch using an AP:M6zM5x stack, because the ground plane completely isolates the patch from the lower layers, neither the magnetic field nor the electric field penetrating through the ground plane.

Dual-Band Grounded Patch Filter with Collinear Feeding

On-wafer chip layout for single-band dual-mode patch filter F-7 operating at 175 GHz and dual-band dual-mode F-8 operating at 175 GHz / 267 GHz, which are implemented on B55-8ML M8U:M2M1, are shown in Figure 4.11 (a) and Figure 4.11 (b), respectively. Both filters are of overall size 0.037 mm^2 (side length 194 µm). A remark to mention, that filters F-9 and F10 (see Figure 3.21) were sent to BEQIUA2022 tape out, which is not received yet.

The measured and simulated results for F-7 are shown in Figure 4.12(a). The agreement between simulation and measurement results is very good, thanks to the fact that the simulation could be carried out considering the full presence of dummies, which are a lot with this filter. The operating frequency is 175 GHz. The measured insertion loss is equal to 4.1 dB, with FBW equal to 17%. The measured and simulated results for F-8 are shown

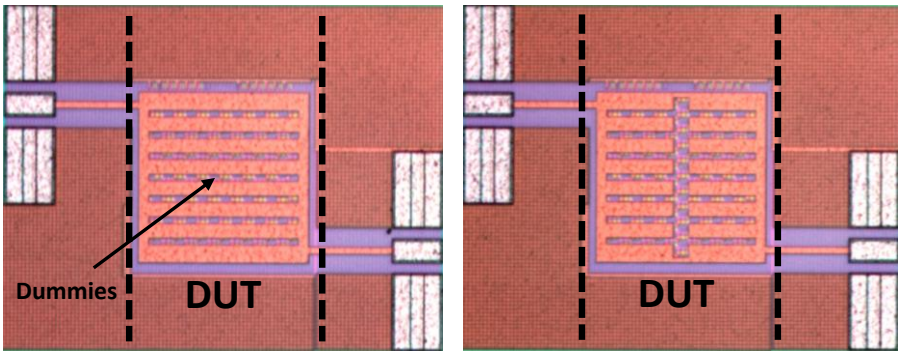

(a) (b)

Figure 4.11: On-wafer chip patches on M8U:M2M1 stack: (a) F-7 single-band dual-mode at 175 GHz, (b) F-8 single-band dual-mode at 175 GHz.

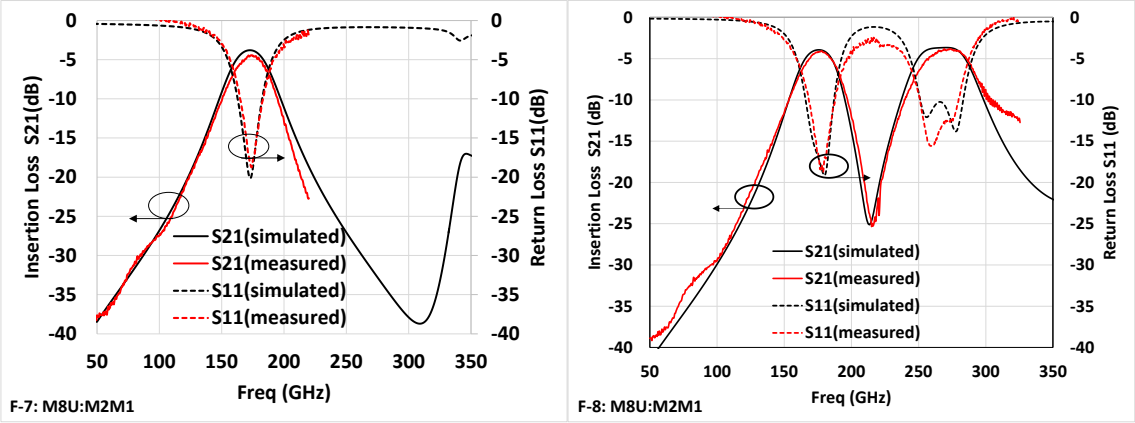

(a) (b)

Figure 4.12: Dual-mode patch filters measurement results: (a) F-7 single-band, (b) F-8 dual-band.

in Figure 4.12(b). Here again, the agreement between simulation and measurement results is very good, because dummies could be fully considered this time in simulation because of less occupied area. The operating frequency is 175 GHz for the first band, same as F-7 for the single-band dual-mode filter, and 267 GHz for the second band. The measured insertion loss is equal to 4 dB, with FBW equal to 17%, for both bands.

Selective Grounded Patch Filter with Orthogonal Feeding

On-wafer chip layout for the dual-mode patch filter F-11 with orthogonal feeding structure operating at 120 GHz is shown in Figure 4.13. It is implemented on B55-8ML AP:M6zM5x stack. In addition, F-12, implemented on B55-9ML AP:M6zM5x, and F-13 and F-14, implemented on B55-8ML M9v:M6zM5x with same topology, are realized but their images are not available. Filters with same topology, were realized in order to show

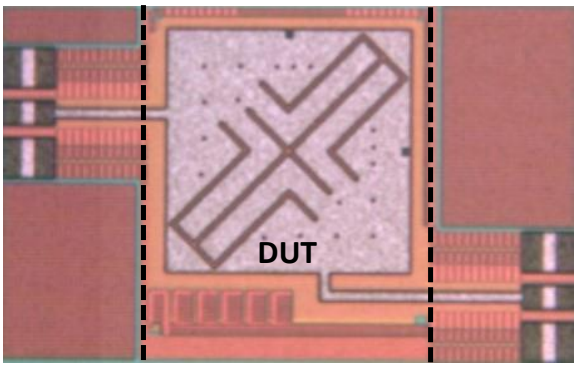

Figure 4.13: On-wafer chip dual-mode patch filter F-11 on B55-8ML AP:M6zM5x stack.

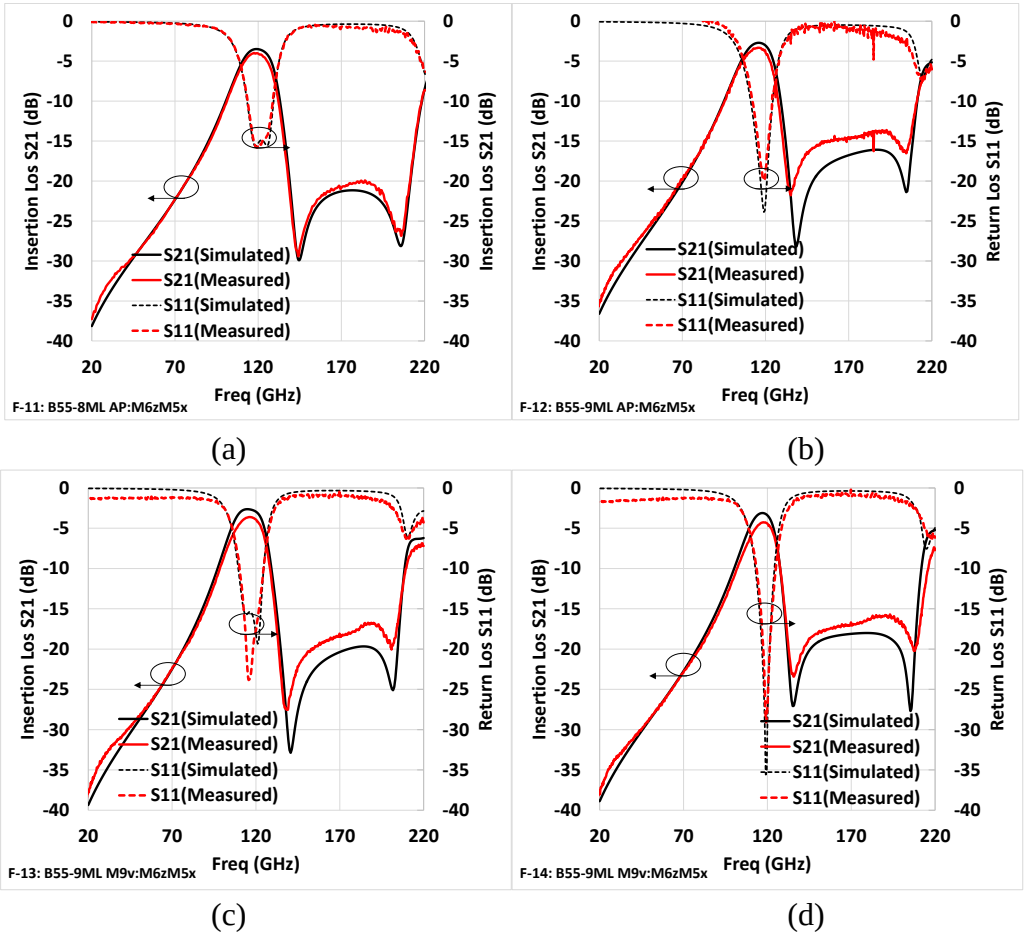

Figure 4.14: Dual-mode patch filters measurement results: (a) F-11, (b) F-12, (c) F-13, (d) F-14.

the advantage of increasing the BEOL for passive circuit, especially with the improvement of Q_u.The overall size for all the filters is 0.07 mm^2 (side length 267 µm).

The on-wafer measurement results for F-11, F-12, F-13 and F-14 filters are shown in Figure 4.14. As a first remark, all the measurement and simulated results are with great agreement. A difference in insertion loss, around 1 dB in case of F-13 and F-14, is due to

the conductivity of *vias*, which in reality is tolerated between different limits. The measured insertion loss for F-11 is 4.2 dB with FBW equal to 18 %. The insertion loss was improved with F-12, which recorded 3.3 dB for the same FBW of 18%. Same stack AP:M6zM5x was used but with different B55 versions (8ML and 9ML). The recorded insertion loss for F-13 is 3.6 dB with FBW of 18 %. Hence, F-12 is slightly better than F-13 because AP:M6zM5x is thicker than M9v:M6zM5x. The advantage of B55-9ML version appears with the measured results of F-14, which was implemented on M9v:M6zM5x. The recorded insertion loss is 4.3 dB, but for FBW of 15 %. This could not be possible with same FBW on B55-8ML version. All the filters are well matched with return loss better than 15 dB.

4.3.2. Compact Filters at 60 GHz

Grounded Patch-Like Filter using CSRR

On-wafer chip layout for patch-like filters using CSRR, for 1st order filter F-15 and 2nd order filter F-16, are shown in Figure 4.15 (a) and Figure 4.15 (b), respectively. Both filters operate at 60 GHz and were implemented on B55-8ML M8U:M2M1stack. F-15 has an overall size of 0.04 mm^2 (side length 200 µm) and F-16 has a size of 0.08 mm^2.

The achieved measurement results for F-15 and F-16 are shown in Figure 4.16. A very good agreement between measurement and simulation results is obtained. F-15 has a low insertion loss of 1 dB with big FBW of 88 %. It was realized to verify the concept and to extract the measured Q_{us} of the proposed topology, which recorded 10 at 60 GHz. The insertion loss of F-16 is equal to 5 dB at the operating frequency, while the return loss is better than 11 dB.

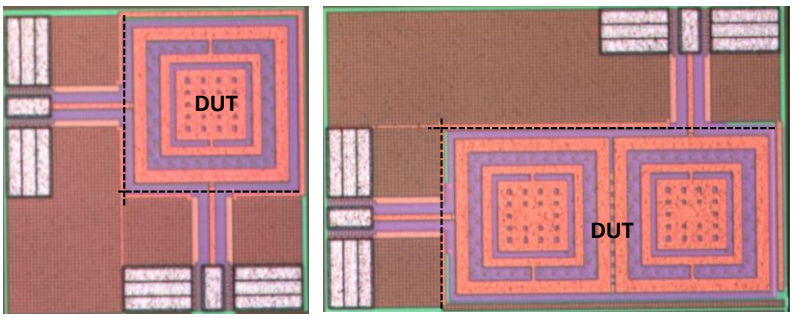

(a) (b)

Figure 4.15: On-wafer chip patch-like filter with CSRR on M8U:M2M1 stack: (a) F-15 Single resonator (b) F-16 2nd order filter.

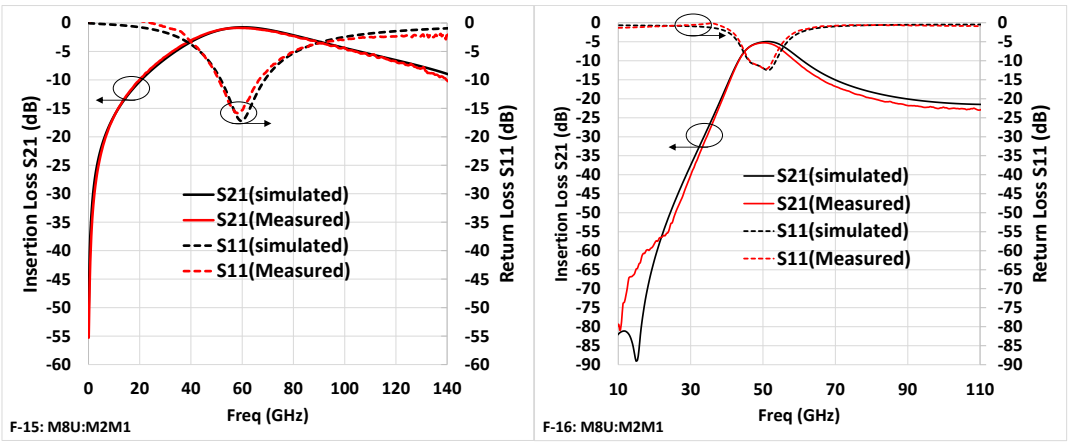

(a) (b)

Figure 4.16: Patch-like with CSRR filters measurement results: (a) F-15, (b) F-16.

The recorded FBW is equal to 23 %. It meets well with the initial conditions set in the filter synthesis. Also, a very good lower out-of-band rejection is achieved, which is interesting given the spectral occupancy of plethora of applications. Generally it is more important to get strong low frequency selectivity for mm-wave filters. A mistake was made with the dimensions when layout was configured, leading to operating frequency of 50 GHz.

Ultra-Compact Patch Filter with Loaded "Mushroom"

On-wafer chip layout for ultra-compact patch filters with loaded "mushroom", for 1st order filter F-17 and 2nd order filter F-18, are shown in Figure 4.17 (a) and Figure 4.17 (b), respectively. Both filters operate at 60 GHz and were implemented on B55-8ML M8U:M2M1stack. F-15 has an overall size of 0.04 mm^2 (side length 200 µm) and F-16 is of size 0.08 mm^2. Those filters are smaller than F-15 and F-16 by 50 %.

The achieved measurement results for F-15 and F-16 are shown in Figure 4.18. A very good agreement between measurement and simulation results is obtained. F-15 has a low insertion of 1 dB with big FBW of 88 %. It was realized to verify the concept and to extract the measured Q_{us} of the proposed topology, which recorded 12 at 60 GHz. The insertion loss of F-16 is equal to 4 dB at the operating frequency, while the return loss is better than 18 dB. The recorded FBW is equal to 27 %. An improvement of 1 dB was achieved for the insertion loss with this filter topology compared with F-16, which is due to the slight adjustment of the Q_u and to the slight increase of FBW. A very good lower out-of-band rejection is achieved, especially < 40 GHz. This is interesting given the spectral occupancy

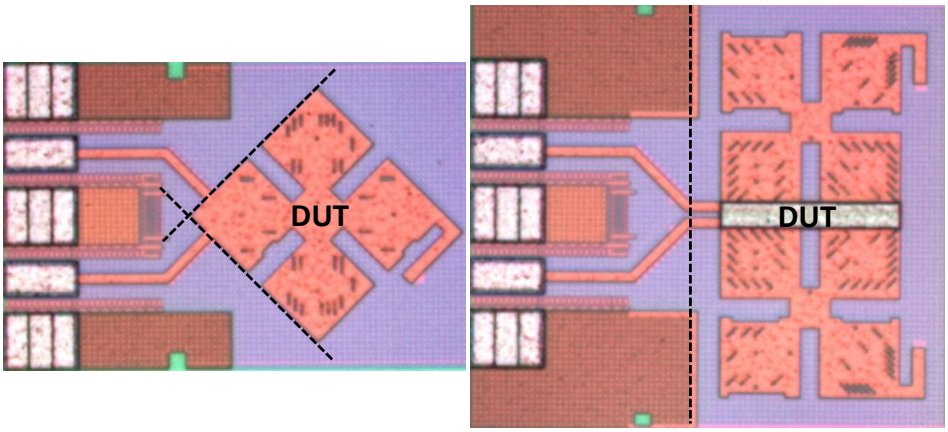

(a) (b)

Figure 4.17: On-wafer chip ultra-compact filter with loaded "mushroom" on M8U:M2M1 stack: (a) F-17 Single resonator (b) F-18 2nd order filter.

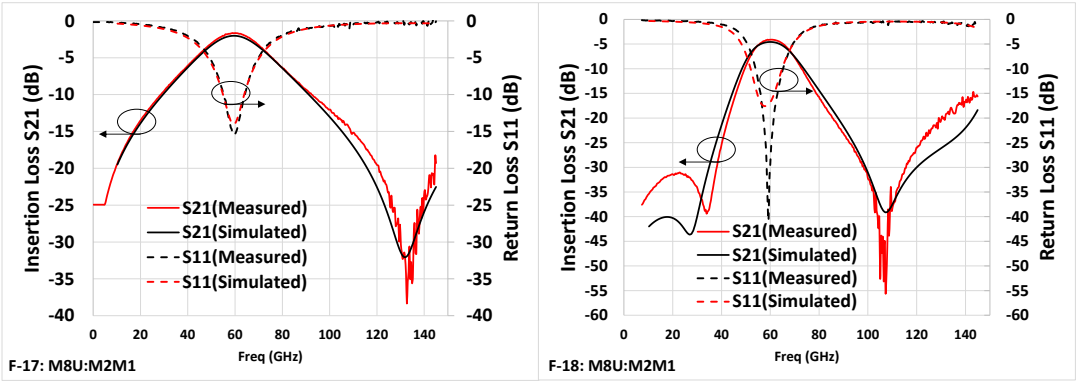

(a) (b)

Figure 4.18: ultra-compact patch filters with loaded "mushroom" measurement results: (a) F-17, (b) F-18.

of plethora of applications. Also the upper out-of-band rejection is improved by the addition of FTZ with rejection level of 20 dB for the band above 85 GHz, up to 128 GHz. Generally it is more important to get strong low frequency selectivity for mm-wave filters. However, the results show that the upper out-of-band rejection can be improved by using cross-coupled filters.

4.4. State-Of-Art Comparison

In order to contextualize the results presented, a comparison with the state-of-art is necessary, as for any scientific work. However, this exercise is complicated in the case of the filters presented in this dissertation, for at least two reasons detailed below.

First, very few articles deal with filters designed above 100 GHz. This comes from the fact that the applications are still few over this frequency, but also from a context where researchers working on the synthesis of filters are still relatively far from microelectronics technologies, and its many constraints. However, since applications begin to emerge beyond 100 GHz, with automotive radars but also the back-haul of the future 6G telecommunication standard, and as already mentioned in the introduction, it becomes necessary for our research community to be proactive in demonstrating that it is possible to create filters with acceptable performance that can be integrated into mm-wave front-ends. The frequency band beyond 100 GHz is certainly little used today, and one might think that the filtering behavior of amplifiers is sufficient, but this will probably no longer be true when the operating frequency of many systems gradually increases.

Secondly, it always proves dangerous to compare the performance of passive circuits (and even active ones) realized using different technologies from microelectronics. As it was shown earlier, the quality factor of a patch or a transmission line depends enormously on the thickness of the BEOL of the technology, so the performance sometimes turns out to be much more linked to the specificities of the technology rather than to the quality and to the originality of the design.

Nevertheless, and despite the two critical mentioned points, the developed filters in this report are compared to the state-of-art that discussed in CHAPTER I as summarized in Table 4.2. Although the works in [11] and [12] are considered among the best published works in 20-30 GHz band, it is still very hard with the extensive use of meandered transmission line topologies to be reproduced to work at higher frequencies. This is especially true when considering technologies like BiCMOS, since the width of the strips increases with the BEOL height, hence limiting the meandering efficiency. So, the focus is on the filters that operate above 60 GHz.

The Q_u obtained for the developed patch resonator filters are relatively comparable to the most of the one obtained for Transmission line-based "comparable" filters. For example, the filters presented in [5], carried-out by our research group, have higher Q_u, due to a realization based on slow-wave transmission lines (S-CPW). Their size is however larger, and they do not allow low frequency rejection, due to the use of a conventional DBR type topology. In addition, as explained in [89], the losses of S-CPW increase sharply with

Table 4.2: Comparison of the Designed mm-wave BPF to works in the State-Of-Art.

Ref	f_c *(GHz)*	*FBW (%)*	*IL (dB)*	*RL (dB)*	*Technology*	Q_u	SF_{30dB}	SF_{20dB}	*Size (mm²)*
[5]-1	60	18	2.6	11	0.13 µBiCMOS	28	0.31	0.34	0.14
[5]-2	60	18	4.1	11	0.13 µm CMOS	23	0.32	0.37	0.29
[11]-a	23	78	2.3	15	0.13 µm BiCMOS	9	-	0.55	0.15
[11]-b	27	70	2.6	13	0.35 µm CMOS	9	0.61	0.63	
[12]-a	23	17	3.8	20		19	0.13	0.17	0.02
[12]-b	31	11	3.2	15	0.13 µm SiGe	34	0.11	0.14	0.02
[12]-c	31	18	2.7	23		26	0.16	0.20	0.04
[15]-b	60	27	2.8	10	0.18 µm CMOS	22	0.38	0.47	0.61
[34]	57	35	3.5	10.2	0.18 µm CMOS	14	-	0.51	0.07
[35]	60	21	2.5	25	0.18 µm CMOS	18	-	-	0.16
[36]	60	23	2.8	20	0.18 µm CMOS	26	0.18	0.47	0.59
[37]	60	13	3.13	11	0.18 µm CMOS	40	-	-	0.03
[38]	60	12	5	38	0.25 µm CMOS	22	-	0.18	0.32
[39]	60	17	4.7	9	90 nm CMOS	17	0.13	0.18	0.04
[40]	60	16	4	20	0.18 µm BiCMOS	27	-	0.17	0.18
[41]	64	19	4.9	10	0.18 µm CMOS	18	0.4	0.43	1.71
[42]	60	22	3.3	30	0.18 µm CMOS	23	-	-	0.05
[43]	60	14	5.9	10	0.13 µm CMOS	20	0.34	0.61	0.35
[44]	60	24	4.2	12	90 nm CMOS	16	-	-	0.12
[45]-a	60	10	9.3	10	0.18 µm CMOS	18	0.23	0.40	0.14
[45]-b	77	10	9.3	10		18	0.26	0.48	0.11
[46]	65	51	2.7	15	0.18 µm CMOS	12	0.02	0.38	0.17
[47]	62	34	3.1	10	0.18 µm CMOS	16	-	-	0.13
[48]	70	26	3.6	12	0.18 µm CMOS	18	0.44	0.55	0.44
[49]	77	18	3.5	10	0.18 µm CMOS	26	0.35	0.42	0.39
[50]	77	27	2.9	20	0.18 µm CMOS	21	0.34	0.42	0.02
[51]	77	23	3.9	20	0.13 µm CMOS	18	-	0.44	0.08
[52]-a	115	18	7.1	20	55 nm BiCMOS (8ML)	17	0.32	0.48	0.05
[52]-b	115	24	5.2	25		17	0.36	0.51	0.07
[52]-c	125	28	4.9	10		16	0.41	0.58	0.07
F-1	**115**	**19**	**4.8**	**20**		**18**	**0.2**	**0.34**	**0.08**
F-2	**116**	**19**	**5.1**	**>15**		**18**	**0.22**	**0.36**	
F-3	**196**	**23**	**3.9**	**18**		**19**	**0.18**	**0.33**	
F-4	**200**	**18**	**3.8**	**18**	**55 nm BiCMOS (8ML)**	**24**	**0.21**	**0.34**	
F-5	**200**	**23**	**3**	**20**		**24.2**	**0.22**	**0.35**	**0.037**
F-8	**180**	**17**	**4.1**	**18**		**25**	**0.19**	**0.33**	
F-9	**176/270**	**17**	**4**	**>14**		**25**	**-**	**0.4/-**	
F-11	**120**	**18**	**4.2**	**>15**		**22**	**0.21**	**0.4**	
F-12	**116**	**18**	**3.3**	**20**	**55 nm BiCMOS (9ML)**	**28**	**-**	**0.35**	**0.07**
F-13	**116**	**18**	**3.6**	**20**		**26**	**-**	**0.36**	
F-14	**119**	**15**	**4.3**	**20**		**26**	**-**	**0.36**	
F-16	**60**	**23**	**5**	**>10**	**55 nm BiCMOS (8ML**	**14.4**	**-**	**0.27**	**0.08**
F-18	**60**	**27**	**4**	**30**		**15.5**	**0.27**	**0.39**	**0.04**

frequency beyond 100 GHz, due to the presence of eddy current losses. The advantage provided by S-CPW would therefore be much more mitigated at 120 GHz, and especially 200 GHz. The filter presented in [36] presents a very high Q_u, equal to 26, with good insertion loss of 2.8 dB, in the other hand its size is higher by 100 times as compared to the work presented in F-18. Also, the filters in [5,15-b-38,40,42,43] present a Q_u above 20, but

their size is much higher than what is achieved with F-17 and F-18 for the same operating frequency of 60 GHz. Moreover, the work in F-18 has overall results comparable to those in [44], but with nevertheless the achieved selectivity (SF_{20dB} = 0.39 and SF_{30dB} = 0.27) that is much better, where [44] is not selective below 15 dB.

For the proposed filters that operate at 120 GHz and above, it is much fair to compare them with the work published in [52], made within our research group using the same 55-nm BiCMOS (8ML) technology. For more illustration, Figure 4.19 (a) and Figure 4.19 (b) show the trend-line variation of insertion loss and Q_u with respect of FBW. They include all the state-of-art in addition to the proposed filters. The majority of the filters are better than the trend-lines, which makes their contribution higher. Also, the performance of the patch filters are much better than of the transmission line filters in [52]. For example, the insertion loss of F-11 (4.2 dB) is less than [52]-a (7.1 dB), for the same FBW. Also, taking the same insertion loss of 4.8 dB like with F-1 and [52]-c, the achieved FBW is 18 % while the other is 28 %. Although the overall selectivity of [52] is better, it is worth to mention that measured filter F-11 has sharp right selectivity of 0.7. It should be noted, however, that the filters presented in [52] call for a more complex design based on the use of coupled lines, with the need to properly control parasitic couplings. This last aspect, namely the simplicity of design, argues in favor of patch filters, which are based on simple structures (apart from the problem of taking dummies into account, depending on each technology), and whose design could be described through simple steps usable by mm-wave.

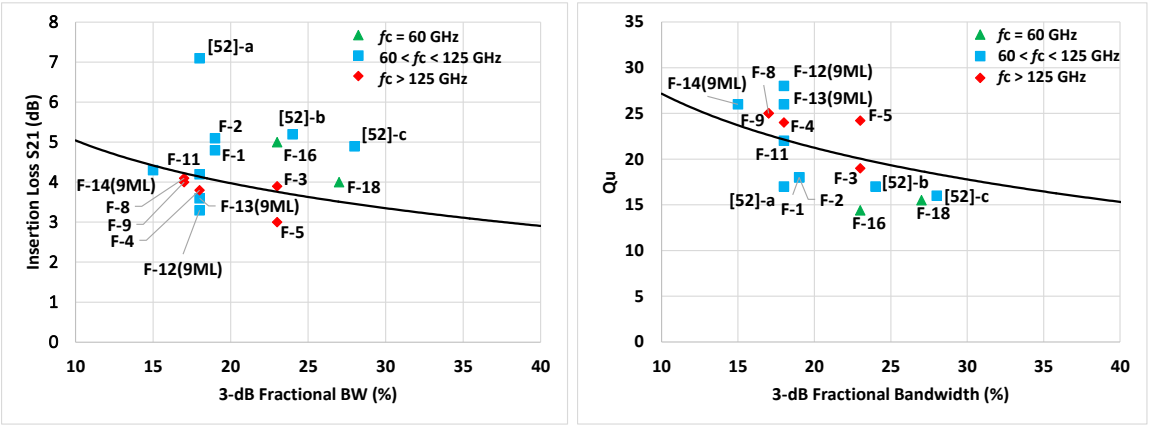

(a) (b)

Figure 4.19: state-of-art comparison: (a) variation of insertion loss with FBW, (b) variation of Q_u with FBW.

Nevertheless, the results achieved in F-12, F-13 and F-14, which are designed on 55- nm BiCMOS 9ML version, are the best among all the presented results. In comparison to the same filter topology used in F-11 and F-12 for the same FBW, but with different BiCMOS versions, 8ML and 9ML, respectively, the recorded insertion loss is 3.6 dB for F-11 and 4.2 dB for F-12. This has a direct impact on Q_u, that records 22 for F-12 and 28 for F-11. The only reason behind this is due to the significant increase of the BEOL thickness with the 9ML version, which impressively improves Q_u. So, the achieved unloaded quality factor is the highest among all the referenced filters, thus naturally leading to relatively low insertion loss for a similar FBW to several other articles in the literature. Therefore, the performance of the integrated filters are not only related to the sophistication of the filter design, but also it is linked to the selected technology.

4.5. Conclusion

In this chapter, the main layout challenges for integrated passive filters on the 55-nm BiCMOS technology were described. It highlighted on the main and critical DRC rules like metal densities for unused metal layers below the patch resonator, which drastically influence the fields and leads to power dissipation. As a solution for that, dummy metals were well organized away from high magnetic field areas created by *vias*. In addition, an empirical analysis for the expected losses was conducted in order to avoid surprises in the measurements.

A full measurement results analysis was carefully carried out. The achieved results meet well with the filters' definitions and can be considered as a promising vision for what can be developed in the future. The comparison with the state-of-art shows that the usage of the 55-nm BiCMOS technology, especially with thicker BEOL as in 9ML version, has a great potential for the development of patch filters. For one of the filters, the recorded Q_u is 28 which is the highest among all the previously published works.

CHAPTER V: FUTURE PERSPECTIVES-DIPLEXER

Diplexers are fundamental circuits within communication systems, as they allow full-duplex communications to be made possible in a simple way. When considering potential applications in the mm-wave bands, it is very complicated to make high-performance diplexers. SAW or BAW filters, which are available for sub-GHz bands are no longer available, and the realization of waveguide filters becomes critical due to mechanical tolerances. In addition, their connection to the planar parts of the circuits, produced in CMOS technologies, poses a problem.

In this context, we have made a first step toward a diplexer operating at 90 GHz using 55-nm BiCMOS technology with 9ML BEOL version. The difference between channels is set to be 10%. The lower channel Filter1 operates at 95 GHz and the upper channel Filter2 operates at 85 GHz. Both Filters are synthesized to have FBW of 10 % and return loss of 20 dB.

Since patch filters show a high flexibility in responses, a conventional dual-mode patch filter with crossed-slots is selected for the study. Its response allows to have FTZs at the lower and upper out-of-band rejection, which will improve the isolation between the channels. The modified configuration for the dual-mode patch filter is shown in Figure 5.1. The proposed filter is loaded by mushrooms at the four edges of the patch, where the *E* field for *even*- and *odd*-modes is maximum. The mushrooms play the role of loading capacitance. The diplexer was implemented on B55-9ML AP:M6zM5x stack with square mushroom plates of length L_c on M9v layer.

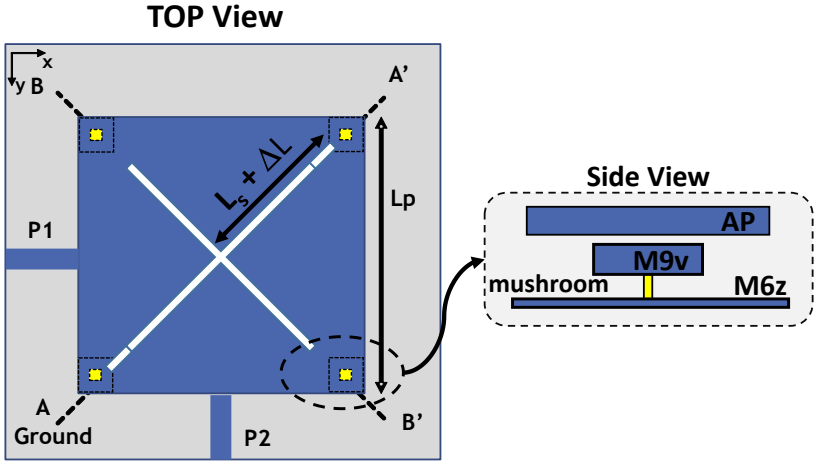

Figure 5.1: Proposed conventional dual-mode patch filter with loading mushrooms.

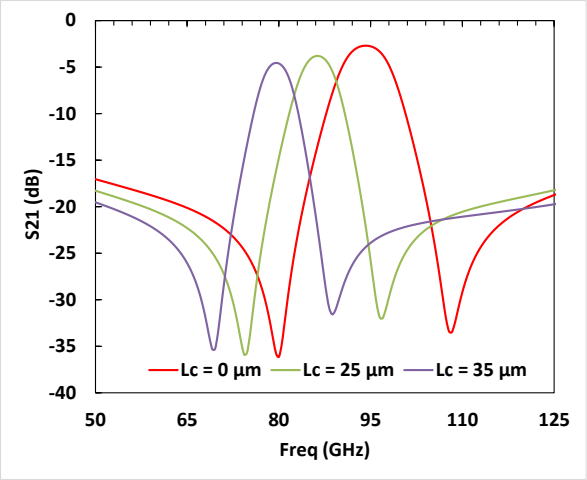

Figure 5.2: simulated S_{21} variation with L_C.

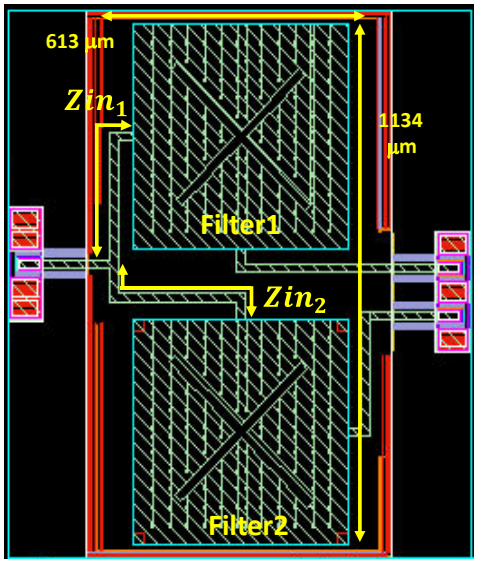

Figure 5.3: Layout configuration for the proposed diplexer at 90 GHz.

The variation of the transmission coefficient response with the square mushroom plate L_C is shown in Figure 5.2. When L_C varies from 0 to 35 µm, the whole response is shifted from f_c = 95 GHz to f_c = 80 GHz. This allows to have same patch size of 0.2 mm^2 (side length 400 µm) for both channels, which reserves area on the wafer.

The final layout of the designed diplexer is shown in Figure 5.3. T-junction of length λ/4 at f_1 and f_2, respectively, was added to connect lower and upper channel branches. For better impedance matching, the input impedance Zin_x at the T-junction needs to satisfy the following conditions:

$$Zin_1 = \begin{cases} \infty & at\ f_2 = 86\ \text{GHz} \\ 50\ \Omega & at\ f_1 = 96\ \text{GHz} \end{cases} \quad (5.1)$$

$$Zin_2 = \begin{cases} 50\ \Omega & at\ f_2 = 86\ \text{GHz} \\ \infty & at\ f_1 = 96\ \text{GHz} \end{cases} \quad (5.2)$$

where Zin_1 and Zin_2 are the input impedance of the diplexer at the junction looking into the lower and upper bands filters, respectively. These conditions are easily satisfied by connecting the junction to each filter with a microstrip line, which ensures an open circuit for the other channel. The overall size of the diplexer, with the T-junction, is 0.69 mm² without pads. It was sent to BEQUIA 2022 tape out. The EM simulation of the whole design is shown in Figure 5.4. The insertion loss is around 4 dB with a FBW equal to 9%. Both filters are well matched with return loss better that 15 dB. Also, the isolation is better than 35 dB at both f_1 and f_2 frequencies.

As a further step after the measurements, a combination of different filter responses based on the results achieved in Chapter VI, especially for F-11 filter, which exhibits better selectivity especially at the upper bands, could be studied.

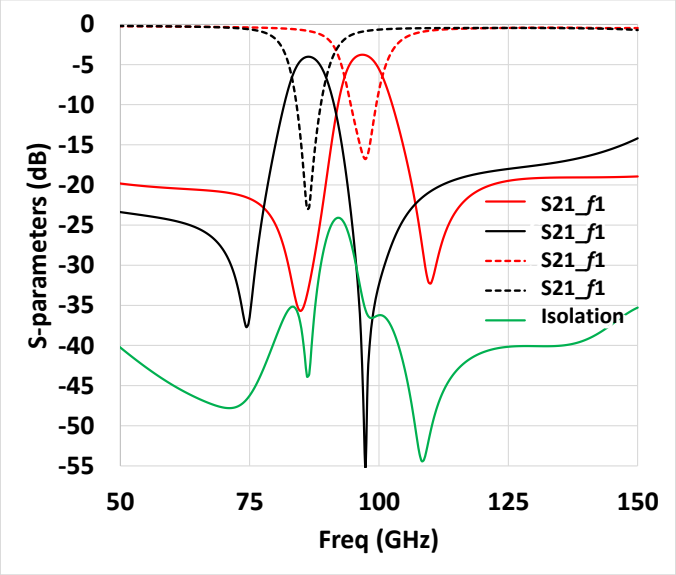

Figure 5.4: EM simulation results for the proposed diplexer.

GENARAL CONCLUSION

As the mm-wave applications for 5G and future 6G have just emerged, RF filters like any other radio blocks have to be re-designed to operate at mm-wave bands. In this dissertation, a full research study was carried out on building integrated dual-mode bandpass patch filters implemented on the 55-nm BiCMOS technology with its two supported versions of BEOL, 8ML and 9ML. The selection of the technology was made on the interest of combining active and passive circuits on the same chip. The choice of working on the development of integrated mm-wave filters was done since beyond 60 GHz, parasitics from interconnections become significant and the need for using single chip for radio becomes high.

Based on the presented literature, patch filters topology haven't been used in integrated circuits or even at mm-wave bands. In most of the published works, TLines was the dominance due to their small size and good performance. Moreover, it was hard for most of mm-wave filters to have FBW below 20% with acceptable losses. In our study, the challenge with patch filters was first to proof its potentiality to work at very high frequencies and second to present compact versions for its resonator. The performance of conventional patch resonators analyzed in CHAPTER I, shows that Q_u increases with frequency, which records at 200 GHz with 8ML version a value of 22. Also, it shows that Q_u increases with the BEOL height, to record with M9v:M6z stack a value of 40. In comparison to TLines, patch filters performance is better. In order to have compact patch resonator, grounded *vias* were used to reduce the edge of the patch resonator from $\lambda/2$ to $\lambda/8$. The work of grounded *vias* is to introduce a new resonance mode that appears below the fundamental modes of the patch, allowing the reduction of overall size.

A full filter theory and synthesis discussion was conducted in CHAPTER II. We used the already published synthesis approaches for dual-mode filters but with some assumptions based on the used resonance modes. In the designed approaches, LC-mode, which is created by via, is one of the main working modes. It can be considered as the new *even*-mode of a conventional patch, since it has a uniform *E* field distribution across the patch area. This is a very important feature to understand in order to define the couplings between the Source/Load with *LC*-mode and between the working modes itself, according

to the designed coupling scheme. All the analytical equations to build up the coupling matrices were explained along with the design methodology work flow.

CHAPTER III is the core of this dissertation where different patch filters were thoroughly designed. Following the drawn design methodology, narrowband dual-mode and dual-band filters, operating at 120 GHz and 270/280 GHz, were developed based on a doublet-coupling scheme. After extracting the coupling matrices, theoretical and simulation results were compared to validate the filter definition. In addition to that, cascaded compact 2nd order patch filters operating at 60 GHz were developed. An original ultra-compact patch resonator using CSRR and loading "mushrooms" structures were designed for that purpose. The combination of these structures with grounded *vias* allows overall area miniaturization of 99 %. All the developed filters were sent into fabrication through different tape out runs.

The layout circuit design along with measurments results analysis compared with the state-of-art were described in CHAPTER IV. It was a challenge to implement the intended filters on BiCMOS due to some technology constraints. Some design rules asked to remove metals from patch area, which impacted the surface current and others asked to add dummy metals in the unused layers below the patch, which impacted the electric field. Based on the expected losses analysis that were made, one of the recommended solutions was to avoid dummies near to the grounded *vias* where high magnetic field exists. After the fabricated filters were received, on-wafer measurements were performed. The measurement results came with great agreement with the simulated results. Dual-mode filters operating at 120 GHz achieved an insertion loss of 3.3 dB and 18 % of FBW. In addition to that, great results for dual-band filter at 176/270 GHz with 4 dB of losses and 17 % of FBW were achieved. The comparison with the literature shows that filters implemented on B55-9ML version with AP:M6z stack record the best performance among all the published works with measured Q_u of 28. This makes the 55-nm BiCMOS 9ML version a promising technology for mm-wave passive circuits design.

Last but not least, diplexer with lower channel at 85 GHz and upper channel at 95 GHz was designed and sent into fabrication based on mushroom loading conventional dual-mode filters. The potentiality of this structure makes it possible to design more sophisticated mm-wave diplexers in the future where the demand is notable.

REFERENCES

[1] www.nokia.com

[2] www.ericsson.com

[3] M. Shafi *et al.*, "5G: A Tutorial Overview of Standards, Trials, Challenges, Deployment, and Practice," *in IEEE Journal on Selected Areas in Communications*, vol. 35, no. 6, pp. 1201-1221, June 2017, doi: 10.1109/JSAC.2017.2692307.

[4] T. Zimmer *et al.*, "SiGe HBTs and BiCMOS Technology for Present and Future Millimeter-Wave Systems," *in IEEE Journal of Microwaves*, vol. 1, no. 1, pp. 288-298, Jan. 2021, doi: 10.1109/JMW.2020.3031831.

[5] A. -L. Franc, E. Pistono, D. Gloria and P. Ferrari, "High-Performance Shielded Coplanar Waveguides for the Design of CMOS 60-GHz Bandpass Filters," *in IEEE Transactions on Electron Devices*, vol. 59, no. 5, pp. 1219-1226, May 2012, doi: 10.1109/TED.2012.2186301.

[6] M. Margalef-Rovira *et al.*, "Design of mm-Wave Slow-Wave-Coupled Coplanar Waveguides," *in IEEE Transactions on Microwave Theory and Techniques*, vol. 68, no. 12, pp. 5014-5028, Dec. 2020, doi: 10.1109/TMTT.2020.3015974.

[7] H. Zhu, X. Zhu, Y. Yang and Y. Sun, "Design of Miniaturized On-Chip Bandpass Filters Using Inverting-Coupled Inductors in (Bi)-CMOS Technology," *in IEEE Transactions on Circuits and Systems I: Regular Papers*, vol. 67, no. 2, pp. 647-657, Feb. 2020, doi: 10.1109/TCSI.2019.2948754.

[8] K. Men, L. Hang and K. S. Yeo, "Design of a Ka-Band U-Shaped Bandpass Filter with 20-GHz Bandwidth in 0.13-µm BiCMOS Technology," *in Electronics*, vol. 9, no. 10, pp. 1608, Oct. 2020, doi: 10.3390/electronics9101608.

[9] Y. Tang, X. Fei, C. Yao, B. Dai and F. Sun, "Design of Compact Millimeter-Wave Bandpass Filter With Multiple Transmission Zeros Using Edge-Coupled Resonators in Silicon Technology," *2020 IEEE Asia-Pacific Microwave Conference (APMC)*, 2020, pp. 890-892, doi: 10.1109/APMC47863.2020.9331667.

[10] F. Sun, H. Zhu, X. Zhu, Y. Yang, Y. Sun and Q. Xue, "Design of Ultra-Wideband On-Chip Millimter-Wave Bandpass Filter in 0.13-µm (Bi)-CMOS Technology," *2019 IEEE International Symposium on Circuits and Systems (ISCAS)*, 2019, pp. 1-4, doi: 10.1109/ISCAS.2019.8702630.

[11] F. Sun, H. Zhu, X. Zhu, Y. Yang, Y. Sun and X. Zhang, "Design of Millimeter-Wave Bandpass Filters With Broad Bandwidth in Si-Based Technology," *in IEEE Transactions on Electron Devices*, vol. 66, no. 3, pp. 1174-1181, March 2019, doi: 10.1109/TED.2019.2895161.

[12] F. Sun, H. Zhu, X. Zhu, Y. Yang and R. Gómez-García, "Design of On-Chip Millimeter-Wave Bandpass Filters Using Multilayer Patterned-Ground Element in 0.13-µm (Bi)-CMOS Technology," *in IEEE Transactions on Microwave Theory and Techniques*, vol. 67, no. 12, pp. 5159-5170, Dec. 2019, doi: 10.1109/TMTT.2019.2949293.

[13] F. Sun, X. Zhu, H. Zhu, Y. Yang and R. Gomez-Garcia, "On-Chip Millimeter-Wave Bandpass Filter Design Using Multi-Layer Modified-Ground-Ring Structure," *2019 IEEE MTT-S International Microwave Symposium (IMS)*, 2019, pp. 853-856, doi: 10.1109/MWSYM.2019.8700897.

[14] Y. Yang, X. Zhu, E. Dutkiewicz and Q. Xue, "Design of a Miniaturized On-Chip Bandpass Filter Using Edge-Coupled Resonators for Millimeter-Wave Applications," *in IEEE Transactions on Electron Devices*, vol. 64, no. 9, pp. 3822-3828, Sept. 2017, doi: 10.1109/TED.2017.2720185.

[15] L. -K. Yeh, C. -Y. Hsu, C. -Y. Chen and H. -R. Chuang, "A 24-/60-GHz CMOS On-Chip Dual-Band Bandpass Filter Using Trisection Dual-Behavior Resonators," *in IEEE Electron Device Letters*, vol. 29, no. 12, pp. 1373-1375, Dec. 2008, doi: 10.1109/LED.2008.2006696.

[16] C. -L. Yang, S. -Y. Shu and Y. -C. Chiang, "Design of a K-Band Chip Filter With Three Tunable Transmission Zeros Using a Standard 0.13- μm CMOS Technology," *in IEEE Transactions on Circuits and Systems II: Express Briefs*, vol. 57, no. 7, pp. 522-526, July 2010, doi: 10.1109/TCSII.2010.2048395.

[17] M. G. Bautista et al., "Millimeter-Wave BPFs Design using Quasi-Lumped Elements in 0.13-μm (Bi)-CMOS Technology," *2019 IEEE International Symposium on Circuits and Systems (ISCAS)*, 2019, pp. 1-5, doi: 10.1109/ISCAS.2019.8702376.

[18] M. G. Bautista, H. Zhu, X. Zhu, Y. Yang, Y. Sun and E. Dutkiewicz, "Compact Millimeter-Wave Bandpass Filters Using Quasi-Lumped Elements in 0.13- μ m (Bi)-CMOS Technology for 5G Wireless Systems," *in IEEE Transactions on Microwave Theory and Techniques*, vol. 67, no. 7, pp. 3064-3073, July 2019, doi: 10.1109/TMTT.2019.2895581.

[19] M. Miao and C. Nguyen, "A Novel Multilayer Aperture-Coupled Cavity Resonator for Millimeter-Wave CMOS RFICs," *in IEEE Transactions on Microwave Theory and Techniques*, vol. 55, no. 4, pp. 783-787, April 2007, doi: 10.1109/TMTT.2007.892817.

[20] Z. J. Hou, Y. Yang, X. Zhu, Y. C. Li, E. Dutkiewicz and Q. Xue, "A Compact and Low-Loss Bandpass Filter Using Self-Coupled Folded-Line Resonator With Capacitive Feeding Technique," *in IEEE Electron Device Letters*, vol. 39, no. 10, pp. 1584-1587, Oct. 2018, doi: 10.1109/LED.2018.2864597.

[21] Y. Yang, X. Zhu, W. Che and Q. Xue, "A Millimeter-Wave On-Chip Bandpass Filter with All-Pole Characteristics," *2019 IEEE MTT-S International Wireless Symposium (IWS)*, 2019, pp. 1-3, doi: 10.1109/IEEE-IWS.2019.8804144.

[22] S. Chakraborty et al., "A Broadside-Coupled Meander-Line Resonator in 0.13-μm SiGe Technology for Millimeter-Wave Application," *in IEEE Electron Device Letters*, vol. 37, no. 3, pp. 329-332, March 2016, doi: 10.1109/LED.2016.2520960.

[23] H. Zhu, X. Zhu, Y. Yang and Q. Xue, "Design of Wideband Third-Order Bandpass Filters Using Broadside-Coupled Resonators in 0.13-μm (Bi)-CMOS Technology," *in IEEE Transactions on Microwave Theory and Techniques*, vol. 66, no. 12, pp. 5593-5604, Dec. 2018, doi: 10.1109/TMTT.2018.2873342.

[24] Y. Zhong, Y. Yang, X. Zhu, E. Dutkiewicz, K. M. Shum and Q. Xue, "An On-Chip Bandpass Filter Using a Broadside-Coupled Meander Line Resonator With a Defected-Ground Structure," *in IEEE Electron Device Letters*, vol. 38, no. 5, pp. 626-629, May 2017, doi: 10.1109/LED.2017.2690283.

[25] Y. Yang, X. Zhu and Q. Xue, "Design of an Ultracompact On-Chip Bandpass Filter Using Mutual Coupling Technique," *in IEEE Transactions on Electron Devices*, vol. 65, no. 3, pp. 1087-1093, March 2018, doi: 10.1109/TED.2018.2797304.

[26] L. Gao and G. M. Rebeiz, "Wideband Bandpass Filter for 5G Millimeter- Wave Application in 45-nm CMOS Silicon-on-Insulator," *in IEEE Electron Device Letters*, vol. 42, no. 8, pp. 1244-1247, Aug. 2021, doi: 10.1109/LED.2021.3089656.

[27] Y. Yang, H. Zhu, X. Zhu and Q. Xue, "A Low-Loss Bandpass Filter using Edge-Coupled Resonator With Capacitive Feeding in (Bi)-CMOS Technology," *in IEEE Electron Device Letters*, vol. 39, no. 6, pp. 787-790, June 2018, doi: 10.1109/LED.2018.2826782.

[28] L. . -K. Yeh, C. . -Y. Chen and H. . -R. Chuang, "A Millimeter-Wave CPW CMOS On-Chip Bandpass Filter Using Conductor-Backed Resonators," *in IEEE Electron Device Letters*, vol. 31, no. 5, pp. 399-401, May 2010, doi: 10.1109/LED.2010.2043333.

[29] Z. Ge, L. Chen, R. Gómez-García and X. Zhu, "Millimeter-Wave Wide-Band Bandpass Filter in CMOS Technology Using a Two-Layered Highpass-Type Approach With Embedded Upper Stopband," *in IEEE Transactions on Circuits and Systems II: Express Briefs*, vol. 68, no. 5, pp. 1586-1590, May 2021, doi: 10.1109/TCSII.2021.3064387.

[30] H. Zhu, Y. Yang, X. Zhu, Y. Sun and S. -W. Wong, "Miniaturized Resonator and Bandpass Filter for Silicon-Based Monolithic Microwave and Millimeter-Wave Integrated Circuits," *in IEEE Transactions on Circuits and Systems I: Regular Papers*, vol. 65, no. 12, pp. 4062-4071, Dec. 2018, doi: 10.1109/TCSI.2018.2839701.

[31] L. Wang, Y. Jiang, Z. Zhang and S. Yu, "Miniaturized Millimeter-Wave On-Chip Resonator Design in Silicon Technology," *2020 IEEE International Conference on Integrated Circuits, Technologies and Applications (ICTA)*, 2020, pp. 147-148, doi: 10.1109/ICTA50426.2020.9332098.

[32] V. N. R. Vanukuru, N. Godavarthi and A. Chakravorty, "Miniaturized millimeter-wave narrow bandpass filter in 0.18 μm CMOS technology using spiral inductors and inter digital capacitors," *2014 International Conference on Signal Processing and Communications (SPCOM), 2014, pp. 1-4*, doi: 10.1109/SPCOM.2014.6983960.

[33] Bo Yang, Efstratios Skafidas and R. Evans, "Design of integrated millimetre wave microstrip interdigital bandpass filters on CMOS technology," *2007 European Microwave Conference*, 2007, pp. 680-683, doi: 10.1109/EUMC.2007.4405283.

[34] S. -C. Chang et al., "Compact Millimeter-Wave CMOS Bandpass Filters Using Grounded Pedestal Stepped-Impedance Technique," *in IEEE Transactions on Microwave Theory and Techniques*, vol. 58, no. 12, pp. 3850-3858, Dec. 2010, doi: 10.1109/TMTT.2010.2086591.

[35] N. Mahmoud, A. Barakat, A. B. Abdel-Rahman, A. Allam and R. K. Pokharel, "Compact Size On-Chip 60 GHz H-Shaped Resonator BPF," *in IEEE Microwave and Wireless Components Letters*, vol. 26, no. 9, pp. 681-683, Sept. 2016, doi: 10.1109/LMWC.2016.2597219.

[36] R. K. Pokharel, X. Liu, R. Dong, A. B. A. Dayang, H. Kanaya and K. Yoshida, "60GHz-band low loss on-chip band pass filter with patterned ground shields for millimeter wave CMOS SoC," *2011 IEEE MTT-S International Microwave Symposium*, 2011, pp. 1-4, doi: 10.1109/MWSYM.2011.5972789.

[37] V. N. R. Vanukuru, "Millimeter-wave bandpass filter using high-Q conical inductors and MOM capacitors," *2016 IEEE Radio Frequency Integrated Circuits Symposium (RFIC)*, 2016, pp. 39-42, doi: 10.1109/RFIC.2016.7508245.

[38] P. Rynkiewicz, A. -L. Franc, F. Coccetti, M. Wietstruck, M. Kaynak and G. Prigent, "A compact millimeter-wave dual-mode ring filter using loaded capacitances in CMOS 0.25µm technology," *2016 IEEE MTT-S International Microwave Symposium (IMS)*, 2016, pp. 1-4, doi: 10.1109/MWSYM.2016.7540058.

[39] Y. -M. Chen, S. -C. Lin, S. -F. Chang and H. -Y. Yang, "A compact CMOS single-ended-to-balanced bandpass filter in millimeter-wave band," *2017 IEEE MTT-S International Microwave Symposium (IMS)*, 2017, pp. 1453-1455, doi: 10.1109/MWSYM.2017.8058893.

[40] K. Ma, S. Mou and K. S. Yeo, "Miniaturized 60-GHz On-Chip Multimode Quasi-Elliptical Bandpass Filter," *in IEEE Electron Device Letters*, vol. 34, no. 8, pp. 945-947, Aug. 2013, doi: 10.1109/LED.2013.2265165.

[41] C. -Y. Hsu, C. -Y. Chen and H. -R. Chuang, "A 60-GHz Millimeter-Wave Bandpass Filter Using 0.18- µm CMOS Technology," *in IEEE Electron Device Letters*, vol. 29, no. 3, pp. 246-248, March 2008, doi: 10.1109/LED.2007.915369.

[42] A. S. A. El-Hameed, A. Barakat, A. B. Abdel-Rahman, A. Allam and R. K. Pokharel, "Ultracompact 60-GHz CMOS BPF Employing Broadside-Coupled Open-Loop Resonators," *in IEEE Microwave and Wireless Components Letters*, vol. 27, no. 9, pp. 818-820, Sept. 2017, doi: 10.1109/LMWC.2017.2734771.

[43] B. Yang, E. Skafidas, and R. J. Evans. "60 GHz compact integrated cross-coupled SIR-MH bandpass filter on bulk CMOS," *in Electronics Letters*, vol. 44, no. 12, pp. 738-740, June 2008, doi: 10.1049/el:20080599.

[44] H-C. Lu, C-S. Yeh, and S-A. Wei. "Miniaturised 60 GHz rectangular ring bandpass filter in 90 nm CMOS technology, " *in Electronics Letters*, vol. 47, no. 7, pp. 448-450, March 2011, doi: 10.1049/el.2010.3636.

[45] L. Nan, K. Mouthaan, Y. -Z. Xiong, J. Shi, S. C. Rustagi and B. -L. Ooi, "Design of 60- and 77-GHz Narrow-Bandpass Filters in CMOS Technology," *in IEEE Transactions on Circuits and Systems II: Express Briefs*, vol. 55, no. 8, pp. 738-742, Aug. 2008, doi: 10.1109/TCSII.2008.922427.

[46] S. Sun, J. Shi, L. Zhu, S. C. Rustagi and K. Mouthaan, "Millimeter-Wave Bandpass Filters by Standard 0.18- μm CMOS Technology," *in IEEE Electron Device Letters*, vol. 28, no. 3, pp. 220-222, March 2007, doi: 10.1109/LED.2007.891305.

[47] C. -C. Lin, C. -Z. Huang and C. -Y. Chen, "Compact and highly selective millimeter-wave meandered bandpass filter using 0.18-μm CMOS technology," *Asia-Pacific Microwave Conference 2011*, 2011, pp. 49-52.

[48] C. -Y. Hsu, C. -Y. Chen and H. -R. Chuang, "70 GHz Folded Loop Dual-Mode Bandpass Filter Fabricated Using 0.18 μm Standard CMOS Technology," *in IEEE Microwave and Wireless Components Letters*, vol. 18, no. 9, pp. 587-589, Sept. 2008, doi: 10.1109/LMWC.2008.2002450.

[49] C. -Y. Hsu, C. -Y. Chen and H. -R. Chuang, "A 77-GHz CMOS On-Chip Bandpass Filter With Balanced and Unbalanced Outputs," *in IEEE Electron Device Letters*, vol. 31, no. 11, pp. 1205-1207, Nov. 2010, doi: 10.1109/LED.2010.2068536.

[50] L. -K. Yeh, Y. -C. Chen and H. -R. Chuang, "A novel ultra-compact and low-insertion-loss 77.GHz CMOS on-chip bandpass filter with adjustable transmission zeros," *2014 44th European Microwave Conference*, 2014, pp. 1056-1059, doi: 10.1109/EuMC.2014.6986620.

[51] Y. -M. Chen and S. -F. Chang, "A ultra-compact 77-GHz CMOS bandpass filter using grounded pedestal stepped-impedance stubs," *2011 41st European Microwave Conference*, 2011, pp. 194-197, doi: 10.23919/EuMC.2011.6101925.

[52] A. A. Saadi *et al.*, "Design of Coupled Slow-Wave CPW Millimeter-Wave Bandpass Filter Beyond 100 GHz in 55-nm BiCMOS Technology," *in IEEE Transactions on Electron Devices*, vol. 68, no. 9, pp. 4259-4266, Sept. 2021, doi: 10.1109/TED.2021.3094780.

[53] W. G. Lin, "Microwave Filters Employing a Single Cavity Excited in More than one Mode," *in Journal of Applied Physics*, vol. 22, no. 8, pp. 989, Oct. 1951, doi: 10.1063/1.1700114.

[54] I. Wolff, "Microstrip bandpass filter using degenerate modes of a microstrip ring resonator," *in Electronics letters*, vol. 8, no. 12, pp. 302-303, June 1972, doi: 10.1049/el:19720223.

[55] J. A. Curtis and S. J. Fiedziuszko, "Miniature dual mode microstrip filters," *1991 IEEE MTT-S International Microwave Symposium Digest*, 1991, pp. 443-446 vol.2, doi: 10.1109/MWSYM.1991.147031.

[56] J.S. Hong and M.J. Lancaster, " Bandpass characteristics of new dual-mode microstrip square loop resonators," *in Electronics letters*, vol. 31, no. 11, pp. 891-892, May 1995, doi: 10.1049/el:19950591.

[57] J. S. Hong and M. J. Lancaster, "Microstrip bandpass filter using degenerate modes of a novel meander loop resonator," *in IEEE Microwave and Guided Wave Letters*, vol. 5, no. 11, pp. 371-372, Nov. 1995, doi: 10.1109/75.473539.

[58] L. Zhu, P. . -M. Wecowski and K. Wu, "New planar dual-mode filter using cross-slotted patch resonator for simultaneous size and loss reduction," *in IEEE Transactions on Microwave Theory and Techniques*, vol. 47, no. 5, pp. 650-654, May 1999, doi: 10.1109/22.763171.

[59] A. L. C. Serrano, and F. S. Correra. "Dual-mode bandpass filter using triangular patch resonator with inverted T-shaped slot," *Microwave and Optical Technology Letters*, vol. 49, no. 12, pp. 2897-2902, Sep. 1999, doi: 10.1002/mop.22927.

[60] A. L. C. Serrano, F. S. Correra, T. -P. Vuong and P. Ferrari, "Synthesis Methodology Applied to a Tunable Patch Filter With Independent Frequency and Bandwidth Control," *in IEEE Transactions on Microwave Theory and Techniques*, vol. 60, no. 3, pp. 484-493, March 2012, doi: 10.1109/TMTT.2011.2181533.

[61] Q. Liu, D. Zhou, D. Zhang, X. Wang, " High-selective triple-mode bandpass filter using a new capacitive-loaded patch resonator," *in Electronics Letters*, vol. 55, no. 24, pp. 1294-1295, Nov. 2019, doi: 10.1049/el.2019.2653.

[62] Q. Liu, D. -F. Zhou, D. -W. Zhang, D. -L. Lü and Y. Zhang, "Dual-Mode Microstrip Patch Bandpass Filters With Generalized Frequency Responses," *in IEEE Access*, vol. 7, pp. 163537-163546, 2019, doi: 10.1109/ACCESS.2019.2952403.

[63] Q. Liu, D. Zhou, X. Wang, M. Tang, D. Zhang and Y. Zhang, "High-Selective Bandpass Filters Based on New Dual-Mode Rectangular Strip Patch Resonators," *in IEEE Microwave and Wireless Components Letters*, vol. 31, no. 10, pp. 1123-1126, Oct. 2021, doi: 10.1109/LMWC.2021.3106128.

[64] D. R. Hendry and A. M. Abbosh, "Parallel Multimode Cavity Filters With Generalized Frequency Response," *in IEEE Transactions on Microwave Theory and Techniques*, vol. 67, no. 5, pp. 1844-1853, May 2019, doi: 10.1109/TMTT.2019.2903470.

[65] Q. Liu, D. Zhang, J. Zhang, D. Zhou, N. An, " Compact single- and dual-band bandpass filters with controllable transmission zeros using dual-layer dual-mode loop resonators," *in Electronics Letters*, vol. 14, no. 6, pp. 522-531, Nov. 2019, doi: 10.1049/el.2019.2653.

[66] Y. C. Li, H. Wong and Q. Xue, "Dual-Mode Dual-Band Bandpass Filter Based on a Stub-Loaded Patch Resonator," *in IEEE Microwave and Wireless Components Letters*, vol. 21, no. 10, pp. 525-527, Oct. 2011, doi: 10.1109/LMWC.2011.2164394.

[67] R. Zhang, L. Zhu and S. Luo, "Dual-Mode Dual-Band Bandpass Filter Using a Single Slotted Circular Patch Resonator," *in IEEE Microwave and Wireless Components Letters*, vol. 22, no. 5, pp. 233-235, May 2012, doi: 10.1109/LMWC.2012.2192419.

[68] G. -Q. Zhang, J. -X. Chen, J. Shi, H. Tang, H. Chu and Z. -H. Bao, "Design of Multilayer Balun Filter With Independently Controllable Dual Passbands," *in IEEE Microwave and Wireless Components Letters*, vol. 25, no. 1, pp. 10-12, Jan. 2015, doi: 10.1109/LMWC.2014.2363018.

[69] S. Sun and W. Menzel, "Novel Dual-Mode Balun Bandpass Filters Using Single Cross-Slotted Patch Resonator," *in IEEE Microwave and Wireless Components Letters*, vol. 21, no. 8, pp. 415-417, Aug. 2011, doi: 10.1109/LMWC.2011.2158535.

[70] Q. Zhang, C. Chen, W. Chen, J. Ding, H. Zhang, "Novel balanced single/dual-band bandpass filters based on a circular patch resonator," *in IET Microwaves, Antennas & Propagation*, vol. 15, no. 2, pp. 206-220, Oct. 2020, doi: 10.1049/mia2.12037.

[71] X.-B. Ji and M. Yang, "Compact Balanced Bandpass Filter with High Selectivity Based on Two Coupled Dual-Mode Microstrip Loop Resonators," *in Progress In Electromagnetics Research Letters*, vol. 90, no. 1, pp. 143-149, Oct. 2020, doi: 10.2528/PIERL20011704.

[72] R. Porath, "Theory of miniaturized shorting-post microstrip antennas," *in IEEE Transactions on Antennas and Propagation*, vol. 48, no. 1, pp. 41-47, Jan. 2000, doi: 10.1109/8.827384.

[73] N. Janković, G. Niarchos, and V. Crnojević-Bengin, "Compact UWB bandpass filter based on grounded square patch resonator," *in Electronics Letters*, vol. 52, no. 5, pp. 372-374, March 2016, doi: 10.1049/el.2015.4087.

[74] V. Radonic and V. Crnojevic-Bengin, "Cross-coupled microstrip filter using grounded patch resonators," *2011 41st European Microwave Conference*, 2011, pp. 763-766, doi: 10.23919/EuMC.2011.6101811.

[75] W. Tang, B. Xiang, S. Zheng, and Y. Long, "Design of wideband/dual-band bandpass filter using a vias and slots loaded sector circular patch resonator," *in INTERNATIONAL JOURNAL OF RF AND MICROWAVE COMPUTER-AIDED ENGINEERING*, vol. 31, no. 7, Jan. 2021, doi: 10.1002/mmce.226.

[76] Q. Yang, H. Li, J. Li, C. Guo, and A. Zhang, "Design of wideband bandpass filter using short-circuited circular patch resonator loaded with slots," *in INTERNATIONAL JOURNAL OF RF AND MICROWAVE COMPUTER-AIDED ENGINEERING*, vol. 31, no. 1, Oct. 2021, doi: 10.1002/mmce.22473.

[77] J.-S. Hong and M. J. Lancaster, "Microstrip Filters for RF/MicrowaveApplications," New York, NY, USA: Wiley, 2001.

[78] H. Zhu, Y. Yang, X. Zhu, Y. Sun and S. -W. Wong, "Miniaturized Resonator and Bandpass Filter for Silicon-Based Monolithic Microwave and Millimeter-Wave Integrated Circuits," *in IEEE Transactions on Circuits and Systems I: Regular Papers*, vol. 65, no. 12, pp. 4062-4071, Dec. 2018, doi: 10.1109/TCSI.2018.2839701.

[79] Y. Yang, X. Zhu, E. Dutkiewicz and Q. Xue, "Design of a Miniaturized On-Chip Bandpass Filter Using Edge-Coupled Resonators for Millimeter-Wave Applications," *in IEEE Transactions on Electron Devices*, vol. 64, no. 9, pp. 3822-3828, Sept. 2017, doi: 10.1109/TED.2017.2720185.

[80] Y. Yang, X. Zhu and Q. Xue, "Design of an Ultracompact On-Chip Bandpass Filter Using Mutual Coupling Technique," *in IEEE Transactions on Electron Devices*, vol. 65, no. 3, pp. 1087-1093, March 2018, doi: 10.1109/TED.2018.2797304.

[81] W. Feng et al., "28-GHz High-Selectivity Bandpass Filters With Dual-Behavior Resonators Using GaAs Technology," *in IEEE Transactions on Plasma Science*, vol. 47, no. 12, pp. 5277-5282, Dec. 2019, doi: 10.1109/TPS.2019.2950708.

[82] G. Shen, W. Feng, W. Che, Y. Shi and Y. Shen, "Millimeter-Wave Dual-Band Bandpass Filter With Large Bandwidth Ratio Using GaAs-Based Integrated Passive Device Technology," *in IEEE Electron Device Letters*, vol. 42, no. 4, pp. 493-496, April 2021, doi: 10.1109/LED.2021.3062862.

[83] K. -D. Xu et al., "Compact Millimeter-Wave On-Chip Dual-Band Bandpass Filter in 0.15-μm GaAs Technology," *in IEEE Journal of the Electron Devices Society*, vol. 10, pp. 152-156, 2022, doi: 10.1109/JEDS.2022.3143999.

[84] K. -D. Xu, Y. -J. Guo, Y. Liu, X. Deng, Q. Chen and Z. Ma, "60-GHz Compact Dual-Mode On-Chip Bandpass Filter Using GaAs Technology," *in IEEE Electron Device Letters*, vol. 42, no. 8, pp. 1120-1123, Aug. 2021, doi: 10.1109/LED.2021.3091277.

[85] Y. -J. Guo, K. -D. Xu, X. Deng, X. Cheng and Q. Chen, "Millimeter-Wave On-Chip Bandpass Filter Based on Spoof Surface Plasmon Polaritons," *in IEEE Electron Device Letters*, vol. 41, no. 8, pp. 1165-1168, Aug. 2020, doi: 10.1109/LED.2020.3003804.

[86] R. J. Cameron, "General coupling matrix synthesis methods for Chebyshev filtering functions," *in IEEE Transactions on Microwave Theory and Techniques*, vol. 47, no. 4, pp. 433-442, April 1999, doi: 10.1109/22.754877.

[87] S. Amari, U. Rosenberg and J. Bornemann, "Adaptive synthesis and design of resonator filters with source/load-multiresonator coupling," *in IEEE Transactions on Microwave Theory and Techniques*, vol. 50, no. 8, pp. 1969-1978, Aug. 2002, doi: 10.110 9/TMTT.2002.801348.

[88] C. -K. Liao, P. -L. Chi and C. -Y. Chang, "Microstrip Realization of Generalized Chebyshev Filters With Box-Like Coupling Schemes," in *IEEE Transactions on Microwave Theory and Techniques*, vol. 55, no. 1, pp. 147-153, Jan. 2007, doi: 10.1109/TMTT.2006.888580.

[89] A. Franc, E. Pistono, G. Meunier, D. Gloria and P. Ferrari, "A Lossy Circuit Model Based on Physical Interpretation for Integrated Shielded Slow-Wave CMOS Coplanar Waveguide Structures," in *IEEE Transactions on Microwave Theory and Techniques*, vol. 61, no. 2, pp. 754-763, Feb. 2013, doi: 10.1109/TMTT.2012.2231430.

APPENDIX

The Matlab code that is used to plot the theoretical scaterring parameters for the optimized coupling matrix is:

```
clear
%------------------------------------------------------------%
% To be completed with the filter specifications:
n=; % n is the order of the filter
fc=; % Central frequency fc in Hz
BW=; % Absolute Bandwidth in Hz
%------------------------------------------------------------%
%-------------------------------------------------------------------------------------------%
%Matrices
R=zeros(n+2);
R(1,1)=1;
R(n+2,n+2)=1;
W=eye(n+2);
W(1,1)=0;
W(n+2,n+2)=0;
M=zeros(n+2);
% To be complete with the necessary couplings of the coupling scheme
% where 1 is related to the source;
% 2 to N-1 are related to the modes;
% N+2 is related to the load.
M(1,2)=;
M(1,3)=;
M(2,2)=;
M(2,3)=;
M(3,3)=;
% For a symmetrical matrix M:
for b=1:n+2
for a=1:n+2
M(a,b)=M(b,a);
end
end
disp(M)
%-------------------------------------------------------------------------------------------%
%------------------------------------------------------%
% To be completed with the graphic definition:
points=; % Definition of the curves
fi=; % Initial frequency of the graphic
ffinal=; % Final frequency of the graphic
f=fi:(ffinal-fi)/(points-1):ffinal;

    %------------------------------------------------------%

%------------------------------------------------------%
% S-parameters calculus
for a=1:points
f1=fc*(f(a)/fc-fc/f(a))/BW;
A=M-1j*R+f1*W;
```

```
B=inv(A);
S21(a)=20*log10(abs(-2*1j*B(n+2,1)));
S11(a)=20*log10(abs(1+2*1j*B(1,1)));
end
%-----------------------------------------------------------%

      plot(f,S21,'b',f,S11,'k','LineWidth',2)
```